Annual Report

of

The Institute of Physics
Academia Sinica

Volume 18

May 1989

The Institute of Physics, Academia Sinica
Taipei, Taiwan, Republic of China

Annual Report

of

The Institute of Physics

Academia Sinica

Volume 18

May 1989

The Institute of Physics, Academia Sinica

Taipei, Taiwan, Republic of China

中央究研院物理研究所集刊

發 行 人 (Publisher)
林 爾 康 (E.K. Lin)

編 輯 (Editor)
余 海 禮 (H.L. Yu)
蕭 先 雄 (S.S. Hsiao)

The Annual Report is published annually by the Institute of Physics, Acadmia Sinica, Taipei Taiwan, 115, Republic of China.

中央研究院物理研究所集刊

第十八卷

中央研究院物理研究所印行

CONTENTS 目 錄

COMMENTS ON THE SPIN CONTENT OF THE PROTON

Hai-Yang Cheng

Institute of Physics, Academia Sinica, Taipei, Taiwan 11529
Republic of China

Abstract

It is shown that while the elastic neutrino-proton scattering data are consistent with the recent EMC measurements on the proton's polarized structure function, they are just marginally compatible with the quark model expectation of the proton's spin content. This suggests that the fraction of the proton spin carried by the quarks is tended to be small as implied by the EMC data, and that the polarization of the ss sea is unlikely negligible. A comment is made on recent $1/N_c$ and chiral-symmetry arguments on the spin content of the proton.

1. Recently, the European Muon Collaboration (EMC) [1] have reported the measurements of deep inelastic polarized μ scattering off polarized protons. While the data are overlapped with the previous SLAC experiments [2], they are substantially lower than had been expected at the smaller values of x. The zero moment of the spin-dependent tructure function $g_1^p(x, Q^2)$ is preliminarily estimated to be [1]

$$\int_0^1 dx\, g_1^p(x, Q^2) = 0.114 \pm 0.012 \pm 0.026 \tag{1}$$

at $Q^2 = 10.7\ GeV^2$, which is significantly lower than the SU(6) model prediction [see Eq. (15) below]. When combined with the data of neutron and hyperon deacys, the EMC result implies that [3, 4]

$$\Delta u = 0.74 \pm 0.08, \quad \Delta d = -0.51 \pm 0.08, \quad \Delta s = -0.23 \pm 0.08 \tag{2}$$

and

$$\Delta u + \Delta d + \Delta s = 0.00 \pm 0.24 \tag{3}$$

where

$$\Delta q = \int_0^1 dx[q^{\uparrow}(x) + \bar{q}^{\uparrow}(x) - q^{\downarrow}(x) - \bar{q}^{\downarrow}(x)] \tag{4}$$

is the helicity of the quark flavor q in the infinite momentum frame of the proton with positive helicity. There are two surprising features inferred from Eqs. (2) and (3): (i) the ss sea is significantly polarized, contrary to the conventional wisdom that $\Delta s \approx 0$, and (ii) the net fraction of the proton spin carried by the quarks is consistent with zero. This has the profound implication that the spin of the proton is due mainly to the gluon polarization and/or to the orbital angular momentum of the quarks [4].

We point out in this Letter that elastic neutrino-proton scatterings provide an independent information on the spin content of the proton. We conclude that the quark model is just marignally accommodated by the νp data and the EMC results seem to be in the right direction.

2. Let's consider the following axial vector currents

$$A_\mu^3 = \bar{u}\gamma_\mu\gamma_5 u - \bar{d}\gamma_\mu\gamma_5 d$$

$$A_\mu^8 = \frac{1}{\sqrt{3}}(\bar{u}\gamma_\mu\gamma_5 u + \bar{d}\gamma_\mu\gamma_5 d - 2\bar{s}\gamma_\mu\gamma_5 s) \tag{5}$$

$$A_\mu^0 = \sqrt{\frac{2}{3}}(\bar{u}\gamma_\mu\gamma_5 u + \bar{d}\gamma_\mu\gamma_5 d + \bar{s}\gamma_\mu\gamma_5 s)$$

and the nucleon axial vector coupling constants at $q^2 = 0$

$$< p \mid A_\mu^i \mid p > = g_A^i s_\mu \tag{6}$$

where s_μ is the proton spin 4-vector. The nonsinglet couplings g_A^3 and g_A^8 under SU(3) flavor symmetry are determined by the usual F and D parameters. In terms of the quark helicity Δq [Eq. (4)] the axial coupling constants read [5]

$$g_A^3 = \Delta u - \Delta d = F + D$$

$$g_A^8 = \frac{1}{\sqrt{3}}(\Delta u + \Delta d - 2\Delta s) = \frac{1}{\sqrt{3}}(3F - D) \tag{7}$$

$$g_A^0 = \sqrt{\frac{2}{3}}(\Delta u + \Delta d + \Delta s) \equiv \sqrt{\frac{2}{3}}S$$

Hence $S \equiv \sqrt{\frac{3}{2}}\, g_A^0$, which cannot be determined from hyperon or neutron β decay, measures the fraction of the proton spin carried by the quarks.

The Bjorken sum rule for the polarized structure function of the proton and neutron is given by

$$\int_0^1 dx\, g_1^p(x) = \frac{1}{2}\int_0^1 dx\,[\frac{4}{9}\Delta u(x) + \frac{1}{9}\Delta d(x) + \frac{1}{9}\Delta s(x)]$$
$$= \frac{1}{12}(g_A^3 + \frac{1}{\sqrt{3}}g_A^8 + 2\sqrt{\frac{2}{3}}g_A^0) \tag{8}$$

and

$$\int_0^1 dx\, g_1^n(x) = \frac{1}{2}\int_0^1 dx\,[\frac{4}{9}\Delta d(x) + \frac{1}{9}\Delta u(x) + \frac{1}{9}\Delta s(x)]$$
$$= \frac{1}{12}(-g_A^3 + \frac{1}{\sqrt{3}}g_A^8 + 2\sqrt{\frac{2}{3}}g_A^0), \tag{9}$$

respectively. Evidently, the unknown axial isoscalar current A_μ^0 contributes to the Bjorken sum rule for g_1^p and g_1^n. Perturbative QCD corrections are different for non-singlet and singlet components of the integral of $g_1^{p,n}(x)$ and amount to multiplying g_A in Eqs. (8) and (9) by [6]

$$(1 - \frac{\alpha_s(Q^2)}{\pi})\, g_A^{3,8} \quad , \quad (1 - \frac{\alpha_s(Q^2)}{3\pi})\, g_A^0 \tag{10}$$

for u, d, s three flavors.

In the naive nonrelativistic SU(6) quark model in which the proton is made of u and d quarks, the constants, F, D and S are predicted to be [7]

$$F + D = \frac{5}{3}\,,\ \frac{D}{F+D} = \frac{3}{5}\,,\ S = \frac{3}{5}(F+D) \tag{11}$$

Substituting this into Eq. (7) leads to

$$g_A^3 = \frac{5}{3}, \quad g_A^8 = \frac{1}{\sqrt{2}} g_A^0 = \frac{1}{\sqrt{3}} \tag{12}$$

Physically, the relation $D/(F + D) = \frac{3}{5}$, which stems from the spin part of the proton wavefunction, ensures no plarization arising from the ss sea, while the prediction $F + D = \frac{5}{3}$ is translated into the fact that the proton spin is entirely responsible by the constituent quarks (i.e. $S = \Delta u + \Delta d + \Delta s = 1$ here).

Experimentally, $F + D = 1.258 \pm 0.004$ and $D/(F + D) = 0.61 - 0.64$.* The former is noticeably different from the naive SU(6)-model prediction $\frac{5}{3}$. The discrepancy is mainly attributed to the lower component of the relativistic proton wavefunction and to the transverse momentum of the quarks [11]. It is evident from the above discussion that within the SU(6) quark model, the deviation of $D/(F + D)$ from $\frac{3}{5}$ characterizes the degree of the sea-quark polarization.† Using the experimental values of F and D we obtain

$$g_A^3 = 1.258, \quad g_A^0 = 0.616, \quad 0.41 \geqslant g_A^8 \geqslant 0.31 \text{ for } 0.61 \leqslant \frac{D}{F + D} \leqslant 0.64 \tag{13}$$

It is easily checked that the polarization of the ss sea is $0.02 \leqslant \Delta s \leqslant 0.07$.

A popular alternative of estimating g_A^0 or S is to make the use of SU(3) symmetry and the Zweig rule that $<p|s\gamma_\mu\gamma_5 s|p> = 0$ [12]. From Eq. (7) we find $S = 3F - D$ (recall that $S = \frac{3}{5}(F + D)$ in the SU(6) quark model) and hence

$$g_A^3 = 1.258, \quad 0.41 \geqslant g_A^8 = \frac{1}{\sqrt{2}} g_A^0 \geqslant 0.31 \text{ for } 0.61 \leqslant \frac{D}{F + D} \leqslant 0.64 \tag{14}$$

Therefore, the net helicity carried by the quarks (i.e. $S = \sqrt{\frac{3}{2}} g_A^0$) accounts for at least half of the proton spin in either the SU(6) quark model or the SU(3) model supplemented with the Zweig rule, in sharp contrast to the EMC result Eq. (3).

We are ready to see what is the zero the moment of $g_1^p(x,Q^2)$. Substituting

* The best value of F + D is taken from ref. [8]. While the best fit of ref. [9] gives $D/(F + D) = 0.61$, all other analyses [10] yield a little bit large value. For our purpose we take $0.61 \leqslant D/(F + D) \leqslant 0.64$.

† When $D/(F + D) \neq \frac{3}{5}$, the SU(6) prediction $S = \frac{3}{5}(F + D)$ still holds, but it is no longer equal to $3F - D$.

Eqs. (12)-(14) into Eq. (8) and taking into account QCD corrections, we find at $Q^2 = 10\ \text{GeV}^2$

$$\int_0^1 dx\, g_1^p(x, Q^2) = \begin{cases} 0.26 & \text{naive nonrelativistic SU (6) quark model} \\ 0.20 & \text{SU(6) quark model with experimental values of F and D} \\ 0.19 & \text{SU(3) symmetry + Zweig rule with } D/(F + D) = 0.61 \\ 0.17 & \text{SU(3) symmetry + Zweig rule with } D/(F + D) = 0.64 \end{cases} \tag{15}$$

where use of $\Lambda_{QCD} = 150$ MeV has been made. Evidently, the EMC result Eq. (1) is much lower than the quark model expectation.

How reliable is the quark model prediction? Since the isoscalar axial-vector current A_μ^0 has an anomaly, there is no reason to believe that the SU(6) quark model works well for matrix elements of anomalous currents. The large deviation of the EMC measurement Eq. (1) from the quark model expectation thus could be attributed to the axial anomalies.

3. Since the EMC estimate of $\int_0^1 dx g_1^p(x, Q^2)$ and its implication are drastically different from the conventional quark picture, it is thus quite important to have an independent check. Fortunately, the elastic neutrino-proton scattering experiment, which can be used to put bounds on the axial isoscalar coupling, serves this purpose.

The neutral axial-vector hadronic current relevant to the νp elastic scattering has the form

$$A_\mu^Z = \frac{1}{2}(\bar{u}\gamma_\mu\gamma_5 u - \bar{d}\gamma_\mu\gamma_5 d - \bar{s}\gamma_\mu\gamma_5 s) \tag{16}$$

$$= \frac{1}{2} A_\mu^3 + \frac{\sqrt{3}}{6} A_\mu^8 - \frac{1}{6}\sqrt{\frac{3}{2}} A_\mu^0$$

From Eq. (7) it is easily seen that the axial-vector form factor in

$$<p|A_\mu^Z|p> = \bar{u}(p')G_A(Q^2)\gamma_\mu\gamma_5 u(p) \tag{17}$$

at $Q^2 = 0$ is related to the constants F, D and S by*

$$G_A(0) = \frac{1}{2}(F + D) + \frac{1}{6}(3F - D) - \frac{1}{6}S \tag{18}$$

Therefore, g_A^3 and hence S can be extracted from the experimental measurement of $G_A(0)$.

Up to date, the most accurate measurement of $G_A(0)$ comes from the high-statistics experiment on the reactions $\nu_\mu p \to \nu_\mu p$ and $\bar{\nu}_\mu p \to \bar{\nu}_\mu p$ performed at Brookhaven [13].† Since the limit $Q^2 = 0$ is experimentally unattainable, the form factor $G_A(Q^2)$ is usually assumed to have the dipole form

$$G_A(Q^2) = \frac{1}{2}\frac{g_A^3}{(1 + Q^2/M_A^2)^2}(1 + \eta) \tag{19}$$

which is then extrapolated to $Q^2 = 0$. In the experimental analysis of ref. [13] $\sin^2\theta_w$ (θ_w being the Weinberg angle) and M_A are first extracted from fitting the cross sections $d\sigma(\nu_\mu p)/dQ^2$ and $d\sigma(\bar{\nu}_\mu p)/dQ^2$ by taking $\eta = 0$. Then assuming that the axial-vector neutral- and charged-current form factors have the same Q^2 dependence and fixing M_A to the world-average value obtained from charged-current reactions, one finds [13]

$$\eta = 0.12 \pm 0.07, \text{ or } 0.00 < \eta < 0.25 \text{ at 90\% C.L.} \tag{20}$$

---

* The naive relation $G_A(0) = \frac{1}{2}g_A^3$ often employed in the literature is valid only under the assumption of a vanishing $\bar{s}s$ polarization in the proton sea.

† The $\nu_\mu p$ and $\bar{\nu}_\mu p$ elastic scatterings had been measured by the Harvard-Pennsylvania-Wisconsin (HPW) collaboration. Two different separate data samples were taken at different times [14]. The results reported in 1979 and 1982 are

[1979] $G_A(0) = 0.5^{+0.2}_{-0.15}$,

[1982] $G_A(0) = 0.56 \pm 0.03$ or 0.57 ± 0.03

respectively. The 1979's result was used by ref. [15] to estimate S: $2.2 \geqslant S \geqslant 0.0$. A new high-statistics experiment of 1986 gathers an antineutrino (neutrino) sample more than seven (four) times the size of that in earlier HPW experiment.

From Eqs. (19), (20), (7), (8) and (10) we obtain

$$0.71 > S > -0.26,\ 0 > \Delta_s > -0.32,\ 0.19 > \int_0^1 dx g_1^p(x, Q^2) > 0.09 \tag{21}$$

for $D/(F + D) = 0.61$ and

$$0.53 > S > -0.44,\ 0 > \Delta s > -0.32,\ 0.17 > \int_0^1 dx g_1^p(x, Q^2) > 0.06 \tag{22}$$

for $D/(F + D) = 0.64$ at 90% C.L. Since the integral of $g_1^p(x, Q^2)$ was found to be 0.095 ± 0.008 from the SLAC ep data at $Q^2 = 4$ GeV^2 over the range $0.1 < x < 0.64$ [16], it is pertinent to regard Eq. (21) as bounds on various parameters inferred from νp data. Comparing Eq. (21) with Eqs. (12)-(15), it is clear that the quark-model predictions are just marginally compatible with the elastic neutrino-proton scattering measurements. The central values $S \approx 0.23$, $\Delta s \approx -0.16$, $\int_0^1 dx g_1^p(x) \approx 0.14$ suggest that the EMC implications Eqs. (2) and (3) are in the right direction: the net fraction of the proton spin carried by the helicities of the quarks is much smaller than the quark model expectation, and the ss sea is considerably polarized opposite to the proton spin.

Clearly the confirmation of EMC measurements by reducing the errors associated with the $x \to 0$ extrapolation is urgently needed, as stressed by ref. [8]. It also would be quite helpful to measure the zero the moment of $g_1^n(x)$, which is presumably enhanced by almost an order of magnitude relative to the quark model expectation if the nucleon's spin content is that implied by the EMC data.

4. Theoretically, there is still no reliable method to evaluate the matrix element of the isoscalar axial-vector current $\langle p|A_\mu^0|p\rangle$, a crucial term for determining the spin content of the proton. Recently, Brodsky, Ellis and Karliner (BEK) [4] have argued that to the leading order in $1/N_c$ expansion (N_c being the number of colors), $S = 0$ in the chiral limit where $m_u = m_d = m_s = 0$. Moreover, they claimed that in the presence of chiral symmetry breaking the non-orthogonal kinetic mixing of η and η' results in $S = -0.18$. We wish to point out in this section that a nonvanishing $\langle p|A_\mu^0|p\rangle$ actually first appears in the subleading order in $1/N_c$.

To recaptulate the argument of BEK, we consider the pole approximation of the matrix element $\langle p|\partial^\mu A_\mu^0|p\rangle$ evaluated at zero momentum transfer

$$<p|\partial^\mu A^0_\mu|p> \cong \sum_i <0|\partial^\mu A^0_\mu|i> \frac{1}{m_i^2} g_{ipp}\bar{p}\gamma_5 p \tag{23}$$

where i runs over all particles that can be created from the vacuum by $\partial^\mu A^0_\mu$. Hence,

$$\sum_i <0|\partial^\mu A^0_\mu|i> \frac{1}{m_i^2} g_{ipp} \cong 2g^0_A m_N \tag{24}$$

is a generalized Goldberger-Treiman (GT) relation, where m_N is a nucleon mass. For the isovector axial-vector current A^3_μ, one has the familiar GT relation

$$g^3_A m_N = f_\pi g_{\pi NN} \tag{25}$$

with f_π = 94 MeV, where use of the PCAC relation $\partial^\mu A^3_\mu$ has been made. Since in the large N_c limit, $m_N \sim O(N_c)$, $f_\pi \sim O(N_c^{1/2})$ and $g_{\pi NN} \sim O(N_c^{1/2})$, it follows that $g^3_A \propto <p|A^3_\mu|p> \sim O(N_c^0)$.* However, η' decouples from other mesons in thelarge N_c limit. Consequently, in the chiral limit $g_{\eta_0 BB} = 0$ inferred from the Skyrme model [4]. This indicates that a nonvanishing $g_{\eta_0 BB}$ first occurs at order $N_c^{-1/2}$. From Eq. (24) it turns out that

$$g^0_A \sim 0(1/N_c) \text{ in the chiral limit} \tag{26}$$

In the presence of chiral symmetry breaking (i.e. $m_q \neq 0$, q = u, d, s), $g_{\eta' pp} \neq 0$ (though $g_{\eta_0 pp} = 0$ in the leading $1/N_c$ expansion) due to $\eta - \eta'$ mixing effects. There are two such effects: mass mixing and kinetic mixing. The $\eta - \eta'$ mass matrix takes the form (neglecting isospin violation) [17]

$$(\eta_8\ \eta_0)\begin{pmatrix} \frac{4}{3}m_K^2 - \frac{1}{3}m_\pi^2 & -\frac{2}{3}\sqrt{2}(m_K^2 - m_\pi^2) \\ -\frac{2}{3}\sqrt{2}(m_K^2 - m_\pi^2) & \frac{2}{3}m_K^2 + \frac{1}{3}m_\pi^2 + \frac{a}{N_c} \end{pmatrix}\begin{pmatrix}\eta_8 \\ \eta_0\end{pmatrix} \tag{27}$$

The parameter a/N_c related to gluonic anomalies is not fixed to the leading order in

* We disagree with ref. [4] on the N_c dependence of g^3_A.

$1/N_c$ since it depends on which physical mass $m_\eta + m_{\eta'}$, m_η, or $m_{\eta'}$ is used as an input [18]. In the large N_c limit of chiral perturbation theory, the Lagrangian term responsible for $f_K/f_\pi \neq 1$ and for $\eta - \eta'$ kinetic mixing is given by [19] †

$$g\,\mathrm{Tr}[\partial^\mu U^\dagger \partial_\mu U(M^\dagger U + U^\dagger M)] \tag{28}$$

where $U = \exp(2i\phi^a\lambda^a/f_\phi)$ and M is the meson mass matrix

$$M_{ij} = 0\ (i \neq j),\ m_\pi^2 = M_{11} = M_{22},\ m_K^2 = \frac{1}{2}(M_{11} + M_{33}) \tag{29}$$

From Eq. (28) we obtain‡

$$\frac{1}{2}(\partial^\mu\eta_8\ \partial\partial^\mu\eta_0)\begin{pmatrix} 1 + \frac{4m_K^2 - m_\pi^2}{3f_\pi^2}g & -\frac{2}{3}\sqrt{2}\frac{m_K^2 - m_\pi^2}{f_\pi^2}g \\ -\frac{2}{3}\sqrt{2}\frac{m_K^2 - m_\pi^2}{f_\pi^2}g & 1 + \frac{2m_K^2 + m_\pi^2}{3f_\pi^2}g \end{pmatrix}\begin{pmatrix}\partial_\mu\eta_8 \\ \partial_\mu\eta_0\end{pmatrix} \tag{30}$$

and [20]

$$\frac{f_K}{f_\pi} - 1 = 4g\frac{m_K^2 - m_\pi^2}{f_\pi^2} \tag{31}$$

† The other term contributing to $f_K/f_\pi \neq 1$ is

$$g'\mathrm{Tr}(\partial^\mu U^\dagger\partial_\mu U)\,\mathrm{Tr}(M^\dagger U + U^\dagger M)$$

But this Lagrangian vanishes in the large N_c limit [19]. Chiral-loop effects are suppressed by factors of $1/N_c$ and thus can be neglected in the leading $1/N_c$ expansion.

‡ Since BEK applied an ansatz different from Eq.(28), their coefficient of $\frac{1}{2}\partial^\mu\eta_0\partial_\mu\eta_0$ is equal to one.

BEK performed a non-orthogonal transformation to diagonalize the $(\partial_\mu \eta_8, \partial_\mu \eta_0)$ kinetic mixing terms. As a result, their η and η' are not orthogonal physical states. A sensible way for solving this problem is first to diagonalize the kinetic mixing and recast the mass matrix of Eq. (27) in terms of the orthogonal basis $(\underline{\eta}, \underline{\eta}')$. Now, the orthogonal transformation needed for diagonalizing the $\underline{\eta} - \underline{\eta}'$ mass matrix will not affect the $\underline{\eta} - \underline{\eta}'$ kinetic terms. Using the relations, e.g. $<0|\partial^\mu A^0_\mu|\eta'> = m^2_{\eta'} f_\phi \cos\theta$, $g_{\eta' pp} = g_{\eta_s pp} \sin\theta$ (θ being the $\eta - \eta'$ mixing angle) . . . etc.,* it is easily seen that to the $1/N_c$ limit $< p|\partial^\mu A^0_\mu| p>$ and hence g^0_A vanishes, as in the case of chiral limit. To achieve a nonzero $<p|A^0_\mu|p>$ requires a subleading $1/N_c$ expansion to give rise to $g_{\eta_0 pp} \neq 0$. Neglecting chiral-loop effects, it is straightforward to show that

$$\frac{<p|A^0_\mu|p>}{<p|A^8_\mu|p>} = \frac{<p|\partial^\mu A^0_\mu|p>}{<p|\partial^\mu A^8_\mu|p>} = \frac{g_{\eta_0 pp}}{g_{\eta_0 pp}} \tag{32}$$

and hence‡

$$S = \frac{1}{\sqrt{2}} \frac{g_{\eta_0 pp}}{g_{\eta_s pp}} (3F - D) \tag{33}$$

where the magnitude and sign of $g_{\eta_0 pp}/g_{\eta_s pp}$ is in principle calculable from the Skyrme model in which the nonleading $1/N_c$ terms are added to the higher order chiral Lagrangians [22].

5. To summarize, we have surveyed the proton's spin content in the conventional quark modesl. The integral of $g^p_1(x)$ at $Q^2 = 10$ GeV^2 ranges from 0.17 to 0.26. We then showed that while the elastic $\nu_\mu p$ and $\bar{\nu}_\mu p$ data are just marginally compatible with the quark model predictions, they do support the EMC measurements. This implies that the ss sea is considerably polarized in the direction opposite to the proton spin and the net helicities of the quarks are much smaller than the

* Unlike the octet pseudoscalar mesons, it is the axial anomaly term TrGG rather than the current divergence $\partial^\mu A^0_\mu$ to be interpreted as the η' field interpolator [21].

‡ The BEK's result $S = -0.18$ corresponds to $\int_0^1 dx g^p_1(x, Q^2 = 4\ \text{GeV}^2) \approx 0.94$, which is already saturated by the integral of $g^p_1(x, Q^2 = 4\ \text{GeV}^2)$ over the range $0.1 < x < 0.64$ measured by the SLAC polarized ep experiment [16]. This leads us to believe that it is not the $\eta - \eta'$ kinetic mixing that contributes to $<p|A^0_\mu|p>$.

quark model expectation. Finally, we commented that to the leading order in $1/N_c$, $<p|A^0_\mu|p>$ vanishes even in the presence of chiral symmetry breaking.

Note added: After this paper was typed, we learnt that a similar conclusion about the elastic $\nu_\mu p$ data was independently reached by D.B. Kaplan and A. Manohar, HUTP-88/A024 and by J. Ellis and M. Karliner, CERN-TH-5095/88, SLAC-PUB-4592 (1988).

REFERENCES

1. J. Ashman et al., Phys. Lett. **B206** (1988) 364.
2. M. J. Alguard et al., Phys. Rev. Lett. **37** (1976) 1261; **41** (1978) 70; G. Baum et al., Phys. Rev. Lett. **51** (1983) 1135.
3. J. Ellis and R. A. Flores, CERN-TH-4911/87 (1987).
4. S. J. Brodsky, J. Ellis, and M. Karliner, Phys. Lett. **B206** (1988) 309.
5. L. M. Sehgal, Phys. Rev. **D10** (1974) 1663.
6. J. Kodaria, S. Matsuda, T. Muta, K. Sasaki, and T. Uematsu, Phys. Rev. **D20** (1979) 627; J. Kodaira, Nucl. Phys. **B165** (1980) 129.
7. S. L. Adler et al., Phys. Rev. **D11** (1975) 3309.
8. F. E. Close and R. G. Roberts, Phys. Rev. Lett. **60** (1988) 1471.
9. M. Bourquin et al., Z. Phys. **C21** (1983) 27.
10. See, e.g. V. Hughes and J. Kuti, Ann. Rev. Nucl. Part. Sci. **33** (1983) 611.
11. See, e.g. F. E. Close, *"Introduction to Quarks and Partons"* (Academic, New York, 1979).
12. J. Ellis and R. L. Jaffe, Phys. Rev. **D9** (1974) 1444.
13. K. Abe et al., Phys. Rev. Lett. **56** (1986) 1107; L. A. Ahrens et al., Phys. Rev. **D35** (1987) 785.
14. A. Entenberg et al., Phys. Rev. Lett. **42** (1979) 1198; J. Horstkotte et al., Phys. Rev. **D25** (1982) 2743.
15. H. Georgi, D. B. Kaplan, and L. Randall, Phys. Lett. **169B** (1986) 73.
16. G. Baum et al. in ref. [2].
17. C. Rosenzweig, J. Schechter, and G. Trahern, Phys. Rev. **D21** (1980) 3388; P. Di Vecchia and G. Venziano, Nucl. Phys. **B171** (1980) 253.
18. G. A. Christos, Phys. Report **116** (1984) 251.
19. J. Gasser and H. Leutwyler, Nucl. Phys. **B250** (1985) 465.
20. See, e.g. H. Y. Cheng, Phys. Rev. **D34** (1986) 166.

21. E. Witten, Nucl. Phys. **B156** (1979) 269; G. Venziano, Nucl. Phys. **B159** (1979) 213.
22. P. Di Vecchia, F. Nicodemi, R. Pettorino, G. Venziano, Nucl. Phys. **B181**(1981) 318.

MONTE CARLO SIMULATION OF ISING MODEL IN MICROCANONICAL ENSEMBLE

C. H. Kao & Simon C. Lin

Institute of Physics, Academia Sinica
Taipei, Taiwan 11529

Abstract

Metropolis algorithm has been the most popular method to simulate physical systems undergo phase transitions and near criticality. A new alogrithm was proposed by M. Creutz in 1983 to simulate Physical systems in microcanonical ensumble. In this article, we shall introduce Creutz algorithm briefly and apply these ideas to Ising Model. Critical temperature and other typical quantities have been obtained in the microcanonical ensemble. In particular, we have found a relationship between average total energy and temperature dynamically across the critical point in this ensemble. This would enable us to gain physical insight into the controlling of the temperature indicrectly. Additionally, a program of 3-dimensional Ising Model is given here and some further works will be indicated at the end.

I. Introduction

For simulating physical problems, Monte Carlo method is used very widely, and there are many algorithms proposed to implement the Monte Carlo ideas. One of the most interesting subjects is related to the state of a system in thermodymanical equilibrium. In statistical Mechanics, canonical ensemble, microcanonical ensemble and grandcanonical ensemble, provide us with accepted postulates to illustrate microscopic configurations in order to satisfy the equilibrium conditions in different ensemble. The algorithm proposed by Metropolis et al. in 1953[1] is practically a description to obtain equilibrium configurations in canonical ensemble. Metropolis et al. gave a procedure which determines the acceptability of any configuration in the canonical ensemble by generating a random number to compare with Boltzmann factor associated with the temperature of the system. Their algorithm has been applied to various system for the past few decades. Since Ising Model is one of the

most important models in statistical physics, it has been studied very extensively by this algorithm.

However, M. Creutz[2] proposed a new algorithm in 1983, by which he simulated a physical system based on microcanonical ensemble. The algorithm generates the configurations of the microcanonical ensemble by introducing a small fascinating subsystem in contact with the original system, i.e. extra degrees of freedom, called demon. Demon traverses over and exchanges energy with the bulk system in order to generate configurations in equilibrium. There are more details about microcanonical ensemble and Creutz's Method in this paper. Many simulations have been done on Ising Model and a complete program about 3-dimensional Ising lattice is given. Most of the simulations are carried out in a SUN-4 computer. They are also compared with the works done by the Metropolis algorithm, and one can find the advantages and characteristics of Creutz's method.

II. Microcanonical Ensemble

For a conservative system as considered with a fixed number of particle N in a fixed volume V, the macrostate of the system is specified by the value of N, V, and E. At the microscopic level there are in general a large number of different ways or configurations in which the macrostate (N, V, E) can be realized. A particular configuration or microstate is accessible if its properties are consistent with the specified macrostate. Since we have no reason to prefer any microstate, it is reasonable to believe that the system is equally likely to be in any one of its accessible microstates. In order to make this postulate of equal a priori probabilities more precisely, we can imagine in phase space a set of points, Ω (Fig. 1), that every point represents a microstates consistent with the required macrovariables. The Ω is just like a surface which only contains those states of equal energy E. The probability of finding the system in the neighbourhood $d\underline{X}$ of some state $\underline{X}$ in phase space is $P(\underline{X})d\underline{X}$.

Microcanonical ensemble assumes that, for an isolated system, i.e. fixed E, V, and N, the $P(\underline{X})d\underline{X}$ is

$$p(\underline{X})d\underline{X} = \begin{cases} (1/Z)d\underline{X} & ; \text{ if } \underline{X} \text{ is belong to } \Omega \\ 0 & ; \text{ otherwise.} \end{cases} \tag{1}$$

where, Z is a normalization constant, in fact, it is the partition function. The partition function Z can be written as

$$Z = \int_{\Omega} \delta(H(\underline{X}) - E)\, d\underline{X} \tag{2}$$

Any observable A is associated with a function $A(\underline{X})$ which depends on the state of the system. Observable A is equal to the ensemble average over the constant-energy surface Ω,

$$\langle A \rangle = (1/Z)\int_{\Omega} A(\underline{X})\delta(H(\underline{X}) - E)\, d\underline{X}.$$

For ensemble consisted of discrete states, observable A is given by

$$\langle A \rangle = (1/Z)\, \Sigma_X A_X \delta(H(\underline{X}) - E)\ , \tag{3}$$

and partition function is written as

$$Z = \Sigma_X\, \delta(H(\underline{X}) - E)\ . \tag{4}$$

III. Monte Carlo Simulation by Creutz Algorithm

By previous formula of partition function etc., one can imagine that what a valid algorithm for simulation must be. It should be constructed in such a way that the system varies its state around the constant energy surface in a random walk in order to guarantee that sufficient configurations are generated for statistical estimate. Considering the systems in Fig. 2, an additional small system is in contact with the

bulk one which we wish to take its ensemble average. The energy of C_2 is $H(\underline{X})$, we introduce an extra degree of freedom, called demon, with energy E_d for C_1. C_1 and C_2 can be regarded as a whole system C. Since we are interested in microcanonical ensemble, the total energy for system C would have to be fixed. That is,

$$H(\underline{X}) + E_d = E \tag{5}$$

The probability that C in some state, given by the microcanonical ensemble, is

$$P(\underline{X}c)d\underline{X}c \propto \delta[H(\underline{X}c) - E]\, d\underline{X}c \tag{6}$$

The constraint, $C_1 + C_2 = C$, permits us to rewritten (6) as

$$P(\underline{X}c_1, \underline{X}c_2)d\underline{X}c_1\, d\underline{X}c_2 \propto \delta[H(\underline{X}) + E_d - E]\, d\underline{X}c_1\, d\underline{X}c_2 \tag{7}$$

Creutz algorithm allows C_1, i.e. the demon, to exchange energy with C_2.
If we are only interested in subsystem C_1, the probability of finding C_1 in $\underline{X}c_1$ is

$$P(\underline{X}c_1)d\underline{X}c_1 \propto \int \delta[H(\underline{X}) + E_d - E]\, d\underline{X}c_2 \quad d\underline{X}c_1 \ ,$$

or

$$P(\underline{X}c_1)d\underline{X}c_1 \propto \Gamma[E - H(\underline{X})]\, d\underline{X}c_1 \ . \tag{8}$$

If the system C_2 is large enough, C_1 should behave like in contact with an heat bath, that is C_2. Therefore, the smaller demon system C_1 would act as an equilibrium system in contact with a heat bath and the probability distribution will obey the Boltzmann factor, that is

$$P(E_d) \propto e^{(-E_d/k_BT)} \tag{9}$$

When interacting randomly with the system, by the condition of $E_d \ll H(\underline{X})$, the demon will promote a random walk of the system on the surface Ω with fluctuation $\delta H \approx E_d$. On the other hand, (4) is reformulated as

$$Z = \Sigma_x \Sigma_{E_d}\, \delta[H(\underline{X}) + E_d - E] \tag{10}$$

For the reason that we must avoid the system absorbing too much energy from demon, a restriction of positive E_d is necessary.

The outlined procedure looks as follow[3];

1. Construct a state such that $H(\underline{X}) = E$.
2. Set the demon energy E_d (for example $E_d = 0$).
3. Choose a part of the system.
4. Change the local state of the system so that $X \to X'$.
5. Calculate the energy change produced $\delta H = H(X') - H(X)$.
6. Accept the change, only if $\delta H < E_d$, then count X' as a new configuration and set $E_d \Leftarrow E_d - \delta H$, otherwise maintain X as a configuration.
7. Return to step 3.

Step 6 guarantees that the system relaxes to thermal equilibrium and ensures the positivity of the demon energy. Eventually, an ensemble average may be obtained over all configurations generated by the demon.

IV. Ising Model and Phase Transition

The Ising Model was proposed by Lenz and investigated by his graduate student, Ising, to study the phase transition from a paramagnet to a ferromagnet. Ising had found that, in one dimension, the model does not have a phase transition. However, for two and three dimensions, it does exhibit a phase transition. The Ising model is defined as follows: Consider a d-dimensional lattice, associate with each lattice site i a spin s_i which can take the values +1 or −1, the spins interact via a

homogeneous coupling constant J. Under an external magnetic field K, the Hamiltonian is

$$H = -J \sum_{i,j} s_i s_j + \mu K \sum_i s_i \tag{11}$$

where, μ denotes the magnetic moment of a spin. It the exchange constant J is positive, the Hamiltonian is a model for ferromagnetism. For J negative the system is anti-ferromagnetic. We can define the magnetization M as

$$M = m_+ - m_- \tag{12}$$

where m_+ is the number of "up" spins, m_- is the number of "down" spins.

In zero magnetic field, i.e. K = 0, the Ising model shall still exhibits a phase transition. It has a critical point Tc where a second-order transition occurs. For temperature T above Tc, M is equal to zero, when T is below Tc, there is a two-fold degenerate spontaneous magnetization, such as in Fig. 3. There are exact solutions for the magnetization of two-dimensional model. Unfortunately, there is no exact solution in three dimensional model. We can use the micro-canonical Monte Carlo method to simulate spin system in 3-D model. To carry out the work we choose a simple cubic lattice of N^3 where N is the linear length of this lattice. Initially, all spins are set to "up"-state, then we select spins at random and turn them over until the desired energy is reached. The demon energy is supported to zero by the time. There are two ways to choose a part of the system. We can allow demon to sequencially or randomly interact with spins in the lattice. Demon turns the spin of a site from "up" to "down" or from "down" to "up", if this change lowers the energy of the Ising system, and we accept it as a new configuration and store the extra energy to demon. Otherwise, i.e. the energy is raised, we accept the new configuration only if there is enough energy for demon to supply the amount of raising energy. After "touching" with N^3 spins in lattice, we call the time unit a Monte Carlo Step per spin (MCS). In our simulation, periodic boundary condition has been imposed on the system.

Before taking the ensemble average we have to get rid of the first few N_0 MCS to ensure that the system has been relaxed to thermal equilibrium. Let N be the

total number of MCS then the approximation for the magnetization is

$$< M > = (N - N_0)^{-1} \sum_{i>N_0}^{N} M(s_i) \ , \tag{13}$$

where s_i is the i-th generated spin configuration. Since the demon energy ultimately becomes Boltzmann distributed, the slope of $\ell n \left\{P(E_d)\right\} - E_d$ diagram is just the β value, i.e. the temperature. On the other hand, when demon interacts with one spin, the least energy change of system is 4J. It implies that $E_d = 4nJ$ where n is a positive integral. Based on

$$< E_d > = \frac{\sum_{E_d=0}^{\infty} E_d d^{-E_d\beta}}{\sum_{E_d=0}^{\infty} e^{-E_d\beta}}$$

and $E_d = 4nJ$, we can easily show that

$$J/k_B T = (1/4) \ln (1 + 4J/<E_d>) \ , \tag{14}$$

which is another way to compute the temperature.

V. Programming and Results

In order to carry out the algorithm, a C program has been implemented and the program is called ising.c (see Appendix). It is assumed that the lattice is simple cubic. All spins are stored as characters in a two dimensional array. For each character, zero is meant "down" and +2 is "up". Firstly, subprogram present( ) obtains the necessary data to set up the system. All input data are stored in a file "datain" with fixed format. Secondly, initial( ) presets the initial configuration for further simulation. Random numbers are generated by ram( ) which applies the

mode operator "%" on the random number supplied from the system. The demon() is the most important subprogram at all. We let demon interact with the system randomly and pick up the ensemble average by average( ). Finally, plot( ) records the distribution of demon energy. We now turn to the discussion of the results.

Since demon energy is supposed to behave according to the Boltzmann distribution, we show the first result in Fig. 4. Good fitting of dashed line to open points provides a sufficient confidence for our statistics. Spontaneous magnetization of various lattice sizes are shown in Fig. 5. We can obtain the critical point from Fig. 6, the susceptibility of Ising system. The relationship between system energy and β value has also been studied in Fig. 7. In canonical ensemble temperature is used as a controlling parameter, but in microcanonical ensemble we can control the total energy of spins only. Therefore, we carried out the dynamical simulation of the spin system near criticality and found in Fig. 8 that the relationships between energy and temperature are coincident with each other, i.e. there is no hysteresis when the system is moved from below T_c to above T_c in the forward and backward directions. This result permits us to control system temperature by energy in the microcanonical ensemble simulation and no need to worry about the hysteresis. The variation of the magnetization with respect to the actual iteractions in the dynamical process is also plotted in Fig. 9. This is done in the forward direction, i.e. from below T_c toward higher than T_c.

VI. Conclusion

Metropolis algorithm has provided us a good approach to simulate canonical ensemble which enable us to control the temperature of the physical system, while the Creutz algorithm provides a new way to simulate statistical problems based on microcanonical ensemble. The demon energy doesn't interact with the system by employing Boltzmann factor but generates the Boltzmann distribution instead. It may avoid many complicated works such as calling random number or computing exponential function inside a loop, this can save more CPU time. Comparing with the simulation in canonical ensemble[4], our simulation is rather accurate and efficient, and seems to be quite insensitive to the finite-size effect.

Apart from the convenience of the algorithm, the system with larger size could be simulated easily. It can also be vectorized if multi-spin coding is adopted[5][6].

Appendix

```
/*************************** FILE ising.c ********************************/
/*There are two output files generated after carrying out the program.     */
/*One is saved the essential data  of our simulation which are displayed on*/
/*screen ,and the other is saved the distribution of demon energy .        */
/*All input data must be presetted in a file  "datain" ,and the format in  */
/*"datain" is like :(line by line)                                         */
/*                          L(lattice length)                              */
/*                          nmcs                                           */
/*                          J(coupling const.)                             */
/*                          E(desired energy of system)                    */
/*                         Ns(start counting from which Monte Carlo step)*/
/*                          output datafile name                           */
/*                          output file name of demon energy distribution*/
/*************************************************************************/
/* Ising model - Demon ;three dimension; [siz]x[siz]x[siz]spins ;siz < 1000*/
/* using char variable for storing spins */
/* generating a randum number by getting mode("%") to rand() */
#define INDATA "datain"
#define SCREEN 0                    /* SCREEN = 1 : display data on screen   */
#include "math.h"
#include "stdio.h"
#define siz 100
#define enmx 250                    /*enmx: enmx*4 is the largest Ed we allow*/
#define mode 262144
float ram();
long N,E,M,H,Hi,Mi;                 /*N:total number of spins ;L:lattice size*/
int nmcs,J,Ed,L,Ns;                 /*E:preset system energy ;M:magnization  */
char s[siz][siz][siz];              /*H:system energy ;Hi,Mi:initial H & M   */
unsigned long Ned[enmx];            /*nmcs:number of M.C. steps ;J:coupling  */
FILE *fp,*fpp,*fx;                  /*Ns:step for starting count ;Ed:demon E */
char nam[100],dat[100];             /*Ned[xx]:number of demon configurations */
main()                              /*        in Ed = xx*4                   */
{                                   /*nam[]: file of Ed distribution         */
  void preset(),initial();          /*dat[]: file of output data             */
  int demon();
  void distrib(),average(),plot();
  int t,i,ac;
  long d;
  double hcum,magcum;
  double edcum,mag2cum,h2cum,accept;
  long now;
  srand(time(&now)%37);
  accept=0;
  edcum=0;
  hcum=0;
  magcum=0;
  mag2cum=0;
  h2cum=0;
  preset();
  N=(long)L*(long)L*(long)L;
  initial();
  for(i=0;i<enmx;i++)
    Ned[i]=1;
  for(t=0;t<nmcs;t++){
    if(t==Ns&&SCREEN==1) printf("starting....\n");
    for(d=0;d<N;d++){
      ac=demon();
      if(t>=Ns){
        accept=accept+(double)ac;
```

```
        distrib();
        edcum=edcum+(double)Ed;
        hcum=hcum+(double)H;
        magcum=magcum+(double)M;
        h2cum=h2cum+(double)H*H;
        mag2cum=mag2cum+(double)M*M;
      }
    }
  }
  average(edcum,hcum,magcum,h2cum,mag2cum,accept);
  plot();
}
void preset()
{
  if((fx=fopen(INDATA,"r"))==NULL){
    if(SCREEN==1) printf("cannot open input data file \n");
    exit(1);
  }
  fscanf(fx,"%d",&L);
  fscanf(fx,"%d",&nmcs);
  fscanf(fx,"%d",&J);
  fscanf(fx,"%ld",&E);
  fscanf(fx,"%d",&Ns);
  fscanf(fx,"%s",dat);
  fscanf(fx,"%s",nam);
}
/*generate a random number in [0,1] */
/*using the function of "mode"*/
float ram()
{
  float rrr;
  int ri;
  ri=rand()%mode;
  rrr=(float)ri/mode;
  return rrr;
}
/*set up the initial configuration*/
void initial()
{
  int i,j,k,l,r,u,d,f,b,sum,spin;
  for(i=0;i<L;i++){
    for(j=0;j<L;j++){
      for(k=0;k<L;k++){
        s[i][j][k]=2;
      }
    }
  }
  H=-J*N*3;
  M=N;
  while(fabs((double)(H-E))>6){
    i=(int)(ram()*L);
    j=(int)(ram()*L);
    k=(int)(ram()*L);
    s[i][j][k]=2-s[i][j][k];
    if(i==0) l=L-1;          /*periodic boundary condition*/
     else l=i-1;
    if(i==L-1) r=0;
     else r=i+1;
    if(j==0) d=L-1;
     else d=j-1;
    if(j==L-1) u=0;
     else u=j+1;
    if(k==0) b=L-1;
     else b=k-1;
```



```
    if(k==L-1) f=0;
     else f=k+1;
    spin=s[i][j][k];
    sum=s[r][j][k]+s[l][j][k]+s[i][u][k]+s[i][d][k]
        +s[i][j][f]+s[i][j][b];
    H=H-2*J*(6-sum)*(1-spin);
    M=M+2*(spin-1);
  }
  Ed=0;
  Hi=H;
  Mi=M;
  if(SCREEN==1) printf("initial Ed=%d, H=%ld, M=%ld\n",Ed,H,M);
}
/*Let demon go thouth spins*/
int demon()
{
  int i,j,k,l,r,u,d,f,b,ed,spin,sum,acpt=0;
  i=(int)(ram()*L);
  j=(int)(ram()*L);
  k=(int)(ram()*L);
  if(i==0) l=L-1;                    /*periodic B.C.*/
   else l=i-1;
  if(i==L-1) r=0;
   else r=i+1;
  if(j==0) d=L-1;
   else d=j-1;
  if(j==L-1) u=0;
   else u=j+1;
  if(k==0) b=L-1;
   else b=k-1;
  if(k==L-1) f=0;
   else f=k+1;
  spin=s[i][j][k];
  sum=s[r][j][k]+s[l][j][k]+s[i][u][k]+s[i][d][k]
      +s[i][j][f]+s[i][j][b];
  ed=2*J*(6-sum)*(1-spin);
  if(ed<=Ed){
    s[i][j][k]=2-s[i][j][k];
    spin=s[i][j][k];
    acpt=1;
    Ed=Ed-ed;
    H=H+ed;
    M=M+2*(spin-1);
  }
  return acpt;
}
/*count the numbers of configurations according to Ed*/
void distrib()
{
  int d;
  d=Ed/4;
  Ned[d]+=1;
}
/*average energy and M over whole configurations and per spin*/
void average(edcum,hcum,magcum,h2cum,mag2cum,accept)
double hcum,magcum;
double edcum,h2cum,mag2cum,accept;
{
  double edave,have,magave,h2ave,mag2ave,accept_rate,norm,Jf,temp,Nc;
  if(SCREEN==1) printf("final H=%ld , M=%ld\n",H,M);
  Nc=nmcs-Ns;
  norm=1/((double)N*(double)Nc);
  if(SCREEN==1) printf("norm=%e\n",norm);
  edave=edcum*norm;
```

```
  accept_rate=accept*norm;
  norm=norm/N;
  have=hcum*norm;
  magave=magcum*norm;
  h2ave=h2cum*norm;
  mag2ave=mag2cum*norm;
  Jf=(double)J;
  temp=4*Jf/log(1+(4*Jf/edave));
  if(SCREEN==1){
    printf("mean Ed =%lf\n",edave);
    printf("mean H per spin=%lf\n",have);
    printf("mean M per spin=%lf\n",magave);
    printf("mean squared M per spin=%lf\n",mag2ave);
    printf("mean squared H per spin=%lf\n",h2ave);
    printf("accept rate =%lf\n",accept_rate);
    printf("Temperature : %lf\n",temp);
  }
/*put the data to a data file*/
  if((fpp=fopen(dat,"a"))==NULL){
    if(SCREEN==1) printf("cannot open data file\n");
    exit(1);
  }
  fprintf(fpp,"\n######\n%d steps per spin on %dx%dx%d lattice\n",nmcs,L,L,L)
  fprintf(fpp,"count after %d steps\n",Ns);
  fprintf(fpp,"Hi=%ld , Mi=%ld\nHf=%ld , Mf=%ld\n",Hi,Mi,H,M);
  fprintf(fpp,"<Ed>=%lf , accept rate=%lf\n",edave,accept_rate);
  fprintf(fpp,"mean H per spin=%lf , mean M per spin=%lf\n",have,magave);
  fprintf(fpp,"mean squared M per spin =%lf\n",mag2ave);
  fprintf(fpp,"mean squared H per spin =%lf\n",h2ave);
  fprintf(fpp,"Temperature = %lf\noutput file name : %s\n",temp,nam);
  fclose(fpp);
}
/*print Ed distribution to GRAPHER */
void plot()
{
  int i;
  if((fp=fopen(nam,"a"))==NULL){
    if(SCREEN==1) printf("cannot open file\n");
    exit(1);
  }
  fprintf(fp,"\n$$$$$$\nE = %ld\n",E);
  for(i=0;i<enmx;i++){
    fprintf(fp,"%d %ld\n",i*4,Ned[i]);
  }
  fclose(fp);
}
```


References

1. N. Metropolis, A. W. Rosenbluth, M. N. Rosenbluth, A. H. Teller, E. Teller, J. Chem. Phys. 21, 1087 (1953).
2. M. Creutz, Physical Review Letters 50, 1411 (1983).
3. D. W. Heermann: Computer Simulation Method in Theoretical Phys. (New York: Springer-Verlag 1986), P. 82.
4. D. P. Landau, Physical Review B 14, 255 (1976).
   K. Binder: Monte Carlo Methods in Statistical Phys., 2nd Ed. (New York: Springer-Verlag 1986); Applications of the Monte Carlo Methods in Statistical Phys., 2nd Ed. (New York: Springer-Verlag 1987).
5. M. Creutz, and K. J. M. Moriarty, Computer Phys. Commun. 39, 173 (1986).
6. J.-M. Drouffe, and K. J. M. Moriarty, Computer Phys. Commun. 52, 249 (1989).

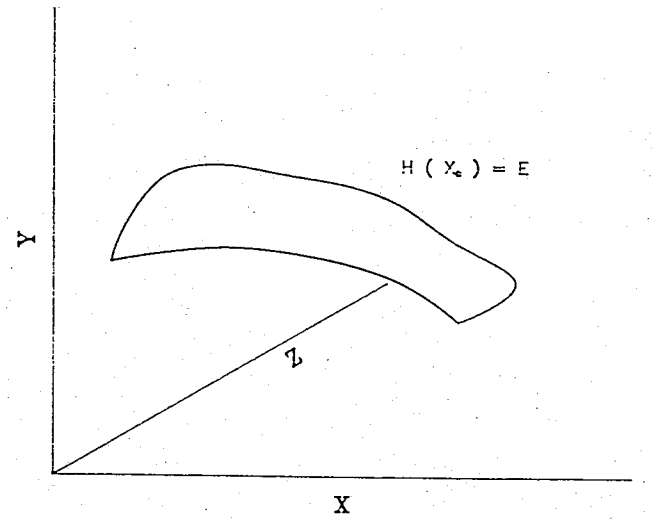

FIG. 1 The surface of constant energy Ω

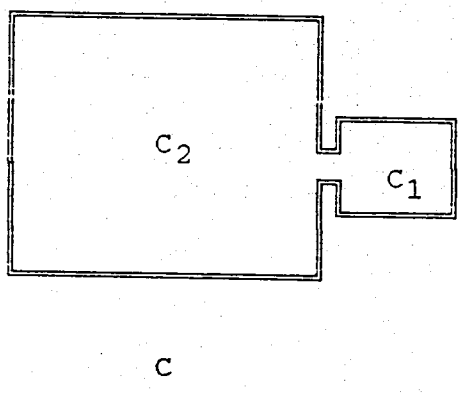

FIG. 2 The total system C wich is composed of C_1 and C_2

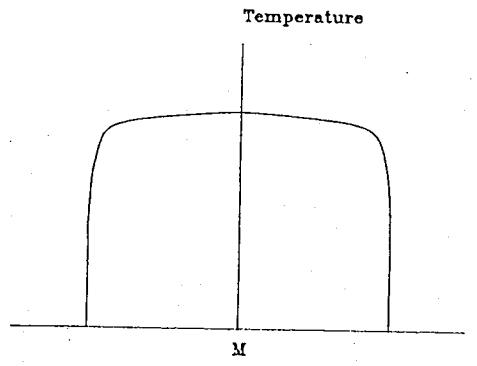

FIG. 3 Two-fold degenerate spontaneous magnetization

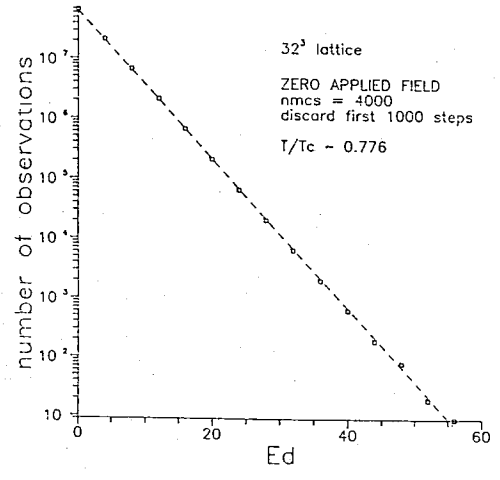

FIG. 4 Demon energy distribution

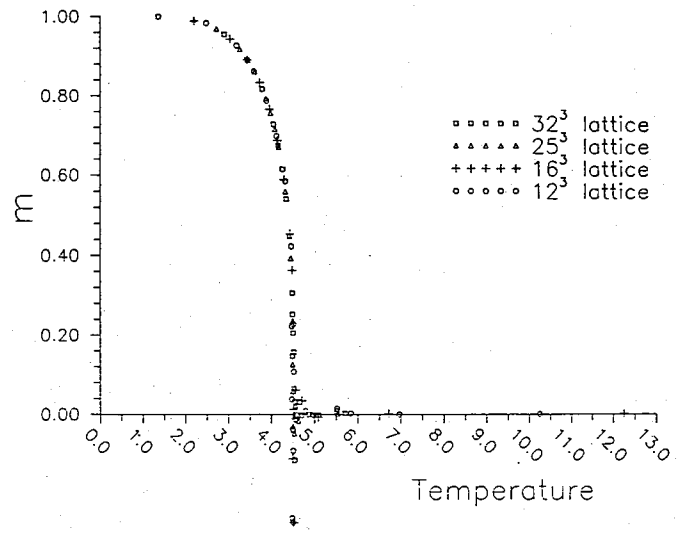

FIG. 5 The relationship between magnetization and temperature of 32^3, 25^3, 16^3, 12^3 lattice sizes

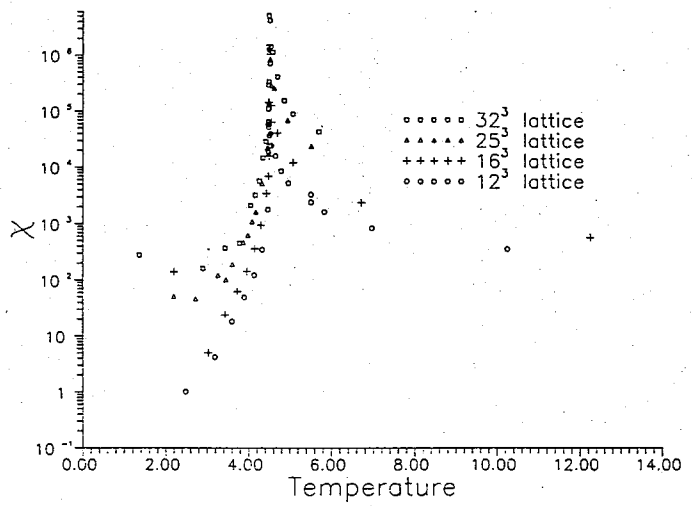

FIG. 6 The susceptibility of various lattice sizes near criticality

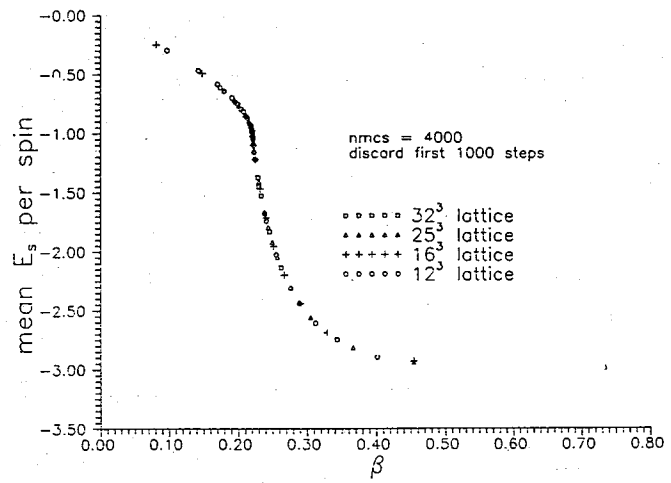

FIG. 7 The relationship between mean energy per spin and β value

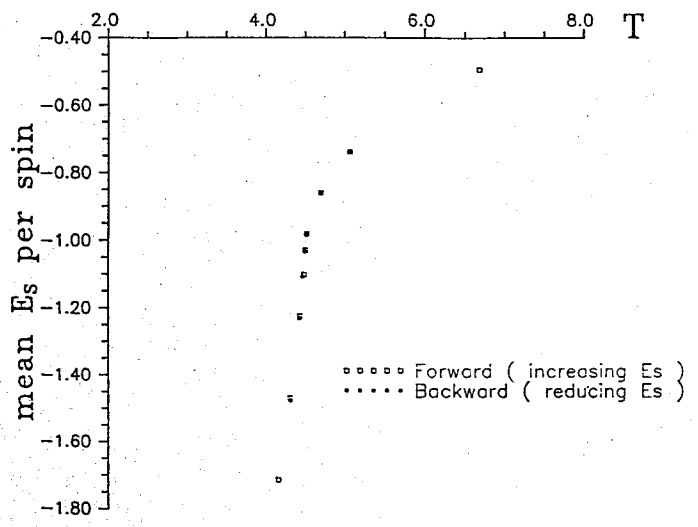

FIG. 8 The dynamical simulation of forward and backward directions on Ising lattice

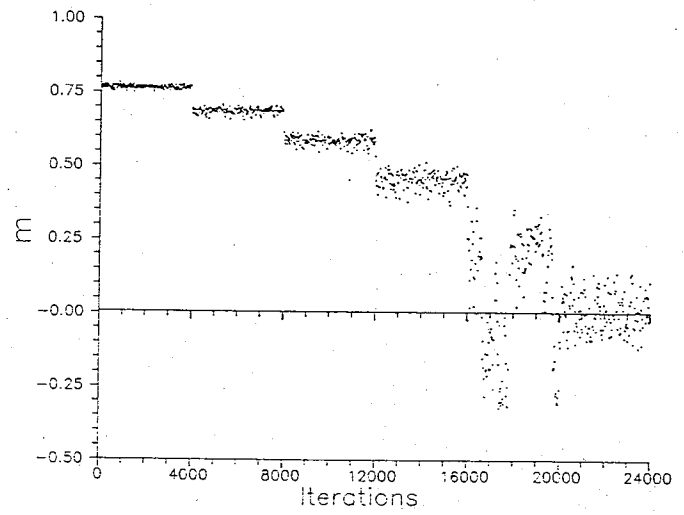

FIG. 9 The variation of magnetization w.r.t. the actual iterations

MONTE CARLO SIMULATION OF GAMMA-RAY DETECTORS IN LOW-ENERGY EXPERIMENTS

S.T. Li, G. C. Kiang, P. K. Teng, Simon C. Lin
Institute of Physics, Academia Sinica

&

L. L. Kiang
Department of Physics, Tsing Hua University

Introduction

Semiconductor detectors, such as lithium-drift germanium (Ge(Li)) and high purity germanium (HpGe) detectors have been used widely in the study of gamma-ray spectroscopy, primarily because of their large sensitive volume and thus outstanding energy resolution. Until recently, a number of results, both experimental and simulated, have been published for the efficiencies and energy spectra of Ge(Li) detectors. Wainio and Knoll [1] were the first who computed the full peak efficiency for planar Ge(Li) detectors by Monte Carlo Simulation. Several other groups have also developed Monte Carlo codes and have applied them to the coaxial detectors and energies up to 12 MeV [2-5]. However, the recently developed HpGe detector has seldom been simulated. We have developed a computer program (MONGE) to simulate the qualitative feature of HpGe detector as well as Ge(Li) detector. In this report, we shall discuss Monte Carlo simulations of some of the important characteristics of the response functions, full peak efficiency and double-escape peak efficiency of detectors. In MONGE, the gamma-ray source can be placed at arbitrary position relative to the detector, and the geometry of the source is changeable.

We assume that the detector and source are kept in vacuum, that is, the scattering by the atmosphere around the detector are not considered. If the energy of the secondary photons produced by Compton process is below 15 KeV, we assume that they are absorbed by the detector without any further interaction. The characteristic X-rays following the photoelectric effect and the bremsstrahlung radiation are neglected for simplicity, thus MONGE program is valid when the incident gamma-ray energy is below 4 MeV. The geometry considered is closed-end HpGe

coaxial detector (the same as that used in our laboratory). The simulation of the 25 cm^2 × 5.9 cm HpGe detector is compared with the experiments made in our laboratory, the agreement is very well. The planar Ge(Li) detector is also simulated and the results are compared with experiments done by Ewan and Tavendale [11] and Cline [12].

Interaction of Gamma Photon and Matter

It is well-known that the incident photon interact with matter through the following processes: photoelectric effect, compton scattering, and pair production. The three processes all produce moving electrons (or positrons), and these electrons (positrons) lose their energy by ionization and bremsstrahlung emission (Fig. 1). Ionization is the more important process for electrons up to a few MeV, but radiative energy losses increase with energy and comparable at about 6 MeV [6]. In our simulation, the gamma-ray energy is up to 4 MeV, so the bremsstrahlung losses are neglected.

In the photoelectric process, the energy of recoil electron is equal to the photon energy minus ionization energy. We assume that all photons interact with K-shell electrons. The energy of the photoelectron is

$$E_P = E_G - E_K \tag{1}$$

where E_G is the photon energy, E_K is the K-shell binding energy. For Ge crystal, E_K is 11.104 KeV. The angular distribution of the photoelectron is [6]

$$dn/d\Omega = A \sin^2\Theta \, [1 + 2\beta(1 + E_K/E_P) * \cos\Theta] \tag{2}$$

where A is a constant, β is the ratio of the velocity of photoelectron to the velocity of light.

In the Compton effect, the gamma-photon interacts with an electron, which gives the electron an amount of energy that depends upon the angle of scattering. Since the binding energy of an electron is small compared to the energy of a gamma photon, and the velocity of the atomic electrons is small compared to the velocity of light, therefore, the electron can be considered as free and at rest before its interaction with the photon. With this assumption, the relationship between the scattering angle and photon energy with the aid of conservation laws of energy and

momentum, is given as

$$\alpha' = \alpha/[1 + \alpha(1 - \cos\Theta)] \tag{3}$$

where $\alpha = E_G/m_eC^2$ is the incident photon energy and α' is the scattered photon energy in the unit of electron rest mass energy. The differential cross section of the Compton-scattered photon is determined by the Klein-Nishina formula [7],

$$\frac{dn}{d\Omega} = \left[\frac{r_0^2(1 + \cos^2\Theta)}{2(1 + \alpha(1 - \cos\Theta))^2}\right] \cdot \left[1 + \frac{\alpha^2(1 - \cos\Theta)^2}{(1 + \cos^2\Theta)(1 + 2(1 - \cos\Theta))}\right] \tag{4}$$

where $\alpha = E_G/m_eC^2$; r_0 is the classical radius of the electron. By eliminating cosΘ from (3), the Klein-Nishina formula can be written in the form,

$$\frac{dn}{d\Omega} = \frac{r_0^2}{2} \cdot \left(\frac{\alpha'}{\alpha}\right)^2 \cdot \left[\frac{\alpha'}{\alpha} + \frac{\alpha}{\alpha'} + 2\left(\frac{1}{\alpha} - \frac{1}{\alpha'}\right) + \left(\frac{1}{\alpha} - \frac{1}{\alpha'}\right)^2\right] \tag{5}$$

which can be used to sample the Klein-Nishina distribution.

Pair production occurs when the gamma-ray energy is greater than 1.022 MeV. The produced electrons and positrons slowed down and deposit their energy in the crystal. When the positron comes to rest, it annihilates with an electron and produces two 0.511 MeV gamma-rays. Both of these must be absorbed to obtain the full energy peak. If one of the gamma-ray escapes from the crystal, then the total energy absorbed is 0.511 MeV less than the original incident gamma-ray energy, and it will contribute to the single-escape peak. If both of the gamma-rays escape from the crystal without making any further interaction, the total energy absorbed is 1.02 MeV less than original gamma-ray energy, and it will contribute to the double-escape peak.

Semiconductor Detector Theory

Semiconductor detectors have a P-I-N diode structure in which the intrinsic (I) region is formed by the depletion of charge carriers with the application of reversed bias across the diode. When the incident photon interacts within the depletion

region, it produces electron (positron) through the photelectric process, Compton process, or pair production. In Ge crystal, the electron (positron) creates free electron- hole pairs at the rate of 1 pair per 2.98 eV, this rate is independent of the particle energy and ionization density over a wide range of energies. The charge carriers (electrons and holes) are swept to their respective collecting electrode by the electric field. The resultant charge is integrated by a charge sensitive preamplifier and converted to a voltage pulse with an amplitude proportional to the produced electron (positron).

Since the pulses relative to these electrons are produced simultaneously, the output pulse would be the sum of the pulses. If all the secondary electrons produced by the incident photon deposit their energies in the detective region and the electric field is sufficient to separate the charge carriers before they recombine, then the amplitude of the output pulses would be proportional to the photon energy. If the detective volume is not large enough, the photon or its recoil-electrons will escape from the detective region and the collected energy will be less than the photon energy. In order to obtain the large sensitive detector volume, extremely pure material is required. Prior to the mid-1970's the required purity on Si and Ge could be achieved only by doping the P-type crystals with Li, in a process known as Lithium-ion drifting. This process is still widely used in the production of Si(Li) X-ray detectors, but now Ge crystals of sufficient purity are grown fairly routinely and the Ge(Li) detector is no longer being produced in substantial quantities. The program we developed can simulate the HpGe detector as well as the Ge(Li) detector with the change of different volume sizes and geometry configurations.

Monte Carlo Simulation

The Monte Carlo method, in our simulation, uses random numbers with suitable probability distribution to determine the occurrence of physical events. In the simulation of the detector, it involves a great number of individual photons passing through the crystal. All interactions between gamma-ray & detector and measurable quantities of the crystal are then simulated according to the given probability distribution function. The geometry and coordinate axes used are shown in Fig. 2. In our program, MONGE, the position of radiation source can be determined freely. If it is inside the core of the surface area of the detective crystal, two random points on the surfaces of source (x_s, y_s, z_s) and crystal (x_c, y_c, z_c) are chosen, the direction cosines are computed according to,

$$\begin{aligned} \cos\alpha &= (y_c - y_s)/d \\ \cos\beta &= (z_c - z_s)/d \\ \cos\gamma &= (x_c - x_s)/d \end{aligned} \tag{6}$$

where d is the distance between (x_s, y_s, z_s) and (x_c, y_c, z_c), i.e. $[(x_c - x_s)^2 + (y_c - y_s)^2 + (z_c - z_s)^2]^{1/2}$. If the source is outside the core of crystal surface area, find out the range of polar angle Θ_{min}, Θ_{max} and the range of azimuthal angle ϕ_{max} $(-\phi_{min} \leqslant \phi \leqslant \phi_{max})$, then the angles are determined from [8]

$$\cos\Theta = \cos\Theta_{min} - R^*(\cos\Theta_{min} - \cos\Theta_{max}) \tag{7}$$

$$\phi = \phi_{max}^*(2R - 1) \tag{8}$$

where R is a random number between 0 and 1.

The intensity of gamma-rays in a medium of interaction cross section μ (cm^{-1}) is distributed as a function of medium thickness r according to $I = I_0 e^{-\mu r}$, where μ is the total cross section of photoelectric effect, Compton scattering and pair production.

$$\mu = \mu_p + \mu_c + \mu_{pp} \tag{9}$$

where I_0 is the intensity of gamma-ray at crystal surface, I is the intensity at depth r. In our simulation, the interaction depth is determined by

$$r = -(1/\mu) * \ln(1 - R) \tag{10}$$

Where R is a uniform random number between 0 and 1. The data of μ, μ_p, μ_c, and μ_{pp} are taken from the experiment of Storm and Israel [9], and we fit the data point to determine the μ values at energy from 15 keV to 10 MeV (Fig. 3). The coordinates of photon or electron varies with their proceeding directions, after each interaction with the media, the transferred directional cosines are given by [3],

for $|\cos\gamma| \neq 1$,

$$\cos\alpha' = \cos\Theta\cos\alpha + [(1 - \cos2\Theta)/(1 - \cos2\gamma)]^{1/2} \cdot [\cos\alpha^*\cos\gamma^*\cos\phi - \cos\beta\sin\phi]$$

$$\cos\beta' = \cos\Theta\cos\beta + [(1-\cos2\Theta)/(1-\cos2\gamma)]^{1/2} \cdot [\cos\beta^*\cos\gamma^*\cos\phi - \cos\alpha\sin\phi]$$

$$\cos\gamma' = \cos\Theta\cos\gamma - [(1-\cos2\Theta)/(1-\cos2\gamma)]^{1/2}[1-\cos2\gamma]\cos\phi$$

for $|\cos\gamma| = 1$,

$$\cos\alpha' = (1-\cos2\Theta)^{1/2}\cos\phi$$

$$\cos\beta' = (1-\cos2\Theta)^{1/2}\sin\phi$$

$$\cos\gamma' = \cos\gamma^*\cos\Theta$$

where Θ is the scattering polar angle, ϕ is the azimuthal angle, the traveling range r is determined from (10). If the position of interaction is outside the crystal, record the photon as running away without interaction and proceed with next incident photon, else use Monte carlo sampling with the distribution according to the ratio of μ_p, μ_c, and μ_{pp} to determine which interaction to occur. In our simulation, the distribution for the photoelectron is given by

$$dn/d\Omega = A\sin^2\Theta[1+2\beta(1+E_K/E_P)*\cos\Theta] \tag{11}$$

which can be obtained by the following random sampling process,

```
if (B <= 1)  do  {  r = -1 + R * 2;
                    p = (1 + B*r)(1 - r^2);
                 }  while (R <= p/1.18);

else  do  {  r = -1/B + R * (1 + 1/B);
             p = (1 + B*r)(1 - r^2);
          }  while (R <= p/1.52);
```

where $B = 2\beta(1 + E_K/E_P)$, R is a random number ($0 \leqslant R \leqslant 1$). The azimuthal angle ϕ is determined from the uniform distribution between 0 and 2Π. The average range of the electron in the direction of its motion is determined from the empirical formula [10],

$$r_R = 9.8434 \times 10^{-5} * E_p - .0176 * (1 - e^{-E/183.96}) \tag{12}$$

where E_P is the electron energy in Kev. The traveling range of electron r_e is sampled from

$$r_e = -(1/r_R)\ln(1-R) \tag{13}$$

where R is a random number between 0 and 1. The stopped position of the electron is computed accordingly. If it is inside the crystal, the energy of the electron is all dissipated in the detector volume, else we compute the traveling range of the electron in the crystal and find out the amount of energy dissipated by electron in the detector. The E_G, photon energy after Compton collision, is determined by sampling the Klein-Nishina distribution (5),

```
do {
     x = (1 + α)/α - sqrt((1 + e)^2 * R + 1/α^2));
     gx = 2 + (1 - x)*2α;
     px = x + 1/(α^2 * e) + α^2 - 2α - 2/α^2 x + 1/α^2 x^2;
   }
while (R > px/gx);
E_G' = α * x * m_e c^2;
```

where R is a uniform random number ($0 \leqslant R < 1$), $e = 1/(1+2\alpha)$ is the minimum possible energy (in unit of $m_e c^2$). The scattering angle corresponds to E_G, is

$$\cos\Theta = 1 + 1/\alpha - 1/(\alpha x) \tag{14}$$

The energy transferred to the Compton electron in the scattering process is

$$E_e = E_G - E_{G'} ,$$

whose polar angle is determined by the kinematic relation

$$\cos\Theta_e = (E_G - E_{G'}\cos\Theta)/E_e \tag{15}$$

The azimuthal angle ϕ of the Compton scattered photon is determined from the uniform distribution between 0 and 2Π, the azimuthal angle of the scattered electron is $\phi + \Pi$. We compute the path of the scattered electron and determined the energy it dissipated in the crystal, and then trace the scattered photon to find

whether it interacts within the crystal. If it does, we choose the process to be simulated again. The complete history is traced until the photon energy is reduced below 15 KeV or it escapes from the detector. It is assumed that the kinetic energy is uniformly shared by the electron and positron. The polar angles of electron and positron with respect to the direction of the gamma-ray are [6].

$$\Theta_{\pm} = m_e c^2 / (\sqrt{3} E_{\pm})$$

where $E_{\pm}$ is the total energy (sum of the rest mass and kinetic energy) of the electron or positron. The azimuthal angle of one of them is sampled from the uniform distribution between 0 and 2Π, azimuthal angle of the other particle is made to differ by Π. We use the same process for the photoelectron and Compton scattered electron to compute the energy dissipated by the electron and positron. If the positron stopped in the detector volume, the annihilation of the positron with electron in crystal takes place. The two annihilation photon with energy of 0.511 MeV are emitted isotropically from the point where the annihilation takes place. The energy, position, and direction of one of the photons is stored. We treat the other photon in the same manner as the Compton scattered photon. After its history is completed (that is, either the photon escapes from the crystal or the energy is reduced to below 15 KeV), we take the stored data of photon and trace the photon in the same way. Each incident photon is simulated until its history is completed and the total energy collected by the detector is the sum of dissipate energy of recoil electrons. We convert the energy into associated channel number, and the peak shape is simulated by the Gaussian distribution, so that the result of program is just like the spectrum appeared in the multi-channel analyzer in experiment. The FWHM (full width at half maximum) of the Gaussian distribution is determined from expertment.

Results

The program has been used to investigate the following results:

a. The response function of gamma-rays in detector;
b. Full energy peak efficiency (ϵ_{fe}), defined as the ratio of the number of photons interact and lose all its energy in the detector to the total number of photons incident on the detector;
c. Double escape peak efficiency (ϵ_{de}), defined as the probability that the incident photon interacts via the pair production reaction with all the electron and positron energy being absorbed in the detector, while both annihilation quanta escape without interaction.

The following types of detectors are discussed in this report: (1) 2.5 cm^2 × 0.35 cm planar Ge(Li) detector, the results of ϵ_{fe} and ϵ_{de} are compared with the experimental values of Ewan and Tavendale [11] and the simulated results of Lal and Iyenger [6]. (2) 2.5 cm^2 × 0.8 cm planar Ge(Li) detector, the results of ϵ_{fe} and ϵ_{de} are compared with the experimental values of Cline [12] and the simulated results of Lal and Iyenger [6] and Wainio and Knoll [1]. (3) 25 cm^2 × 5.9 cm coaxial HpGe detector, the response function of ^{60}Co gamma-ray source placed 25 cm away from detector face, and the results of ϵ_{fe} are compared with the experiments made in our laboratory. The simulated spectrum of ^{60}Co is normalized to compare with the experimental result.

In the simulation of planar Ge(Li), dead layer of the front edge is not accounted. The results agree quite well with the experimental results of Ewan and Tavendale [11] and the simulated results of Wainio and Knoll [1] and Lal and Iyengar [6], but the values of ϵ_{fe} and ϵ_{de} are higher than that in the experiments of Cline [12]. In the simulation of coaxial HpGe, we find out that if the influence of dead layer is not taken into account, the simulated efficiency will much higher than experimental values, especially in low energy part. The data supplied by detector producer (ORTEC) show that the absorbing Al in front surface is 0.127 cm and inactive Ge is 0.07 cm, dead layer in this range is not neglectible (Fig. 3). Because the data is often a rather uncertain approximation [5], we take into account an insensitive region in front surface of 0.14 cm, which makes the simulated efficiency in good agreement with the experimental results. The response function (Fig. 8) agree quite well with the experiment in the region of peak and Compton edge, the lower energy part was omitted because of the remarkable contribution of room scattering and backscattering. To conclude, the Monte Carlo code MONGE is valuable to obtain the response function, full energy peak efficiency and double escape peak efficiency of planar or coaxial detectors. It can also be used to investigate the influence of varying geometries and positions of the source. With minor changes, we will use MONGE to investigate HpGe-NaI (Tl) Compton suppression spectrometer. As for the computing time, it depends on the detector size and incident photon energy. For the HpGe of diameter 5.67 cm and length 5.9 cm, it takes about 150 histories per second at the energy of 1 MeV by use of the PC-386 computer.

References

1. K. M. Wainio & G. F. Knoll, Nucl. Instr. and Meth., 44 (1966) 213.
2. Takashi Nakamura, Nucl. Instr. and Meth., 131 (1975) 521.
3. B. Grosswendt & E. Waibel, Nucl. Instr. and Meth., 131 (1975) 143.
4. L. Moens group, Nucl. Instr. and Meth., 187 (1981) 451.
5. K. Debertin & B. Grosswendt, Nucl. Instr. and Meth., 203 (1982) 343.
6. B. Lal & K.V.K. Iyengar, Nucl. Instr. and Meth, 79 (1970) 19.
7. O. I. Leipunskii, B. V. Novozhilov, V. N. Sakharov, "The Propagation of Gamma Quanta in Matter", Pergamon press, 1965.
8. G. B. Beam, L. Wielopolski, R. P. Gardner & K. Verghese, Nucl. Instr. and Meth. 154 (1978) 501.
9. E. Storm & H. I. Israel, Nucl. Data Tables 7 (6) (1970).
10. Toshimitsu Yamazaki & Jack M. Hollander, Phys. Rev. 140 (1965) B630.
11. G. T. Ewan & A. J. Tavendale, Can. J. Phys. 42 (1964) 2286.
12. J. E. Cline, IEEE Trans. Nucl. Sci. NS-15, No. 3 (1968) 198.

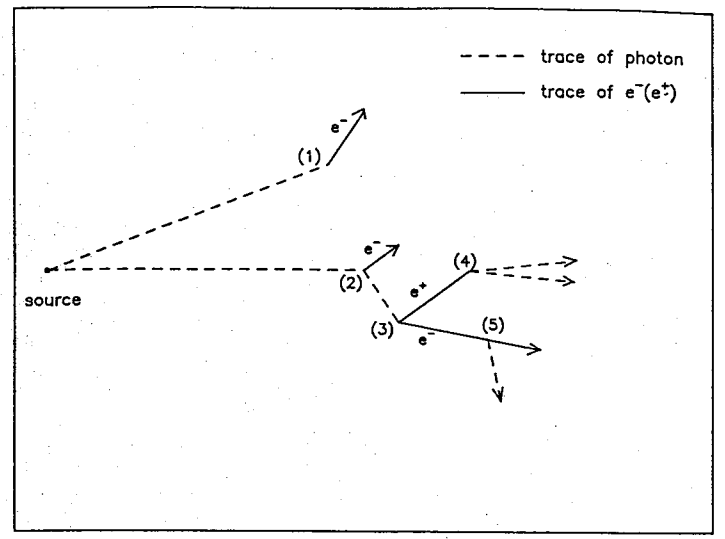

Fig. 1 Interactions of gamma photon with matter. (1) Photoelectric absorption (2) Compton scattering (3) Pair production (4) Positron annihilation (5) Bremsstrahlung emission.

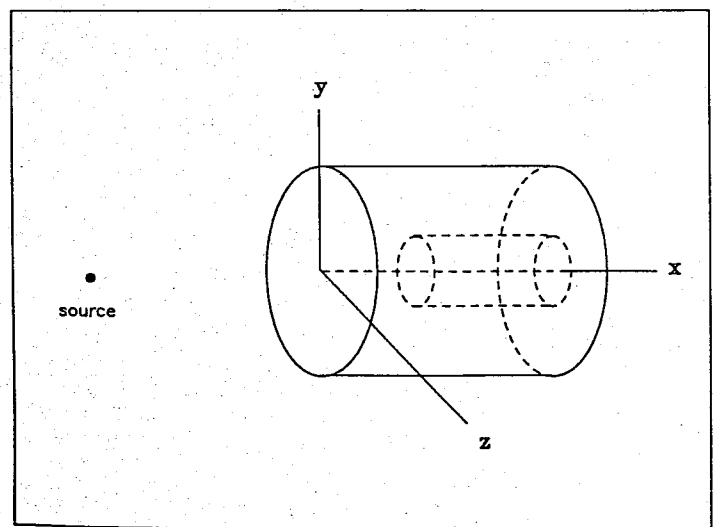

Fig. 2 Geometry of the crystal of closed-end coaxial HpGe detector.

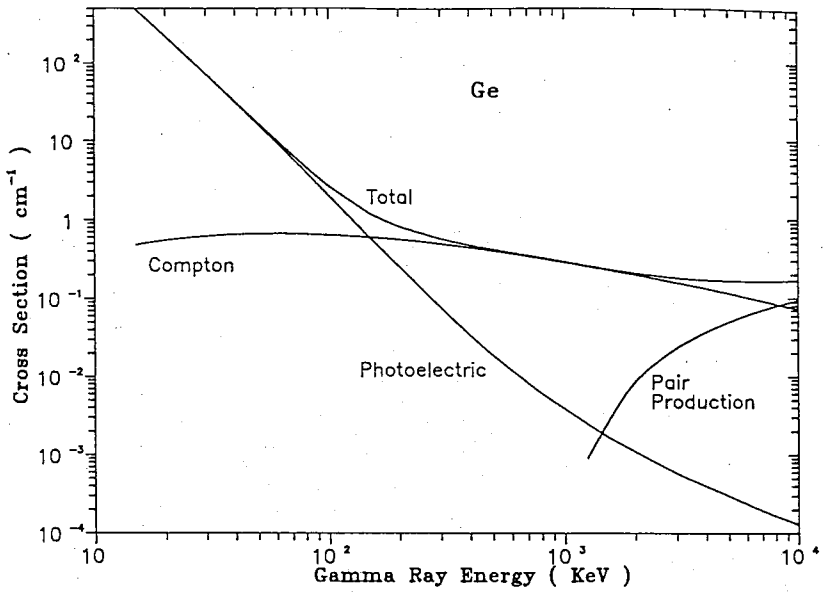

Fig. 3 Absorption coefficients for germanium.

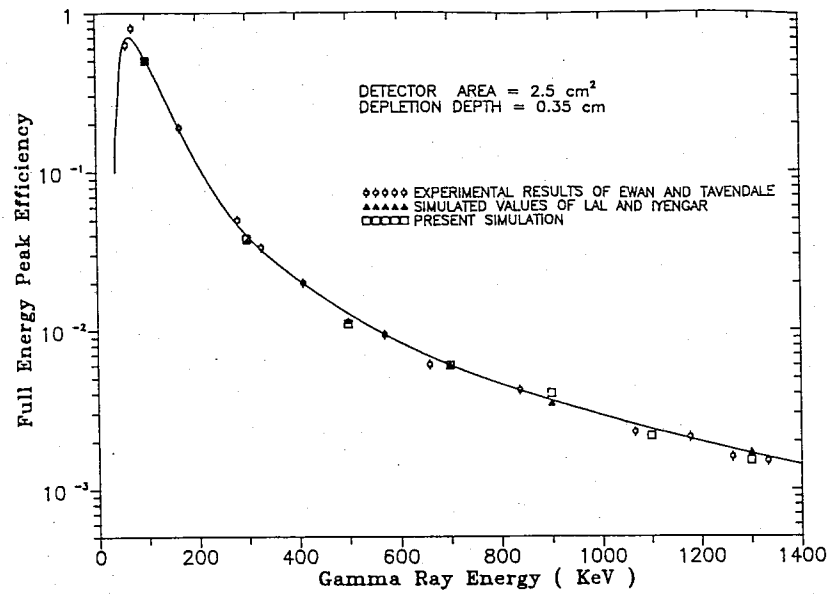

Fig. 4 Comparison of the simulated results of ϵ_{fe} of planar Ge(Li) to the experimental values of Ewan and Tavendale [11] and the simulated results of Lal and Iyenger [6].

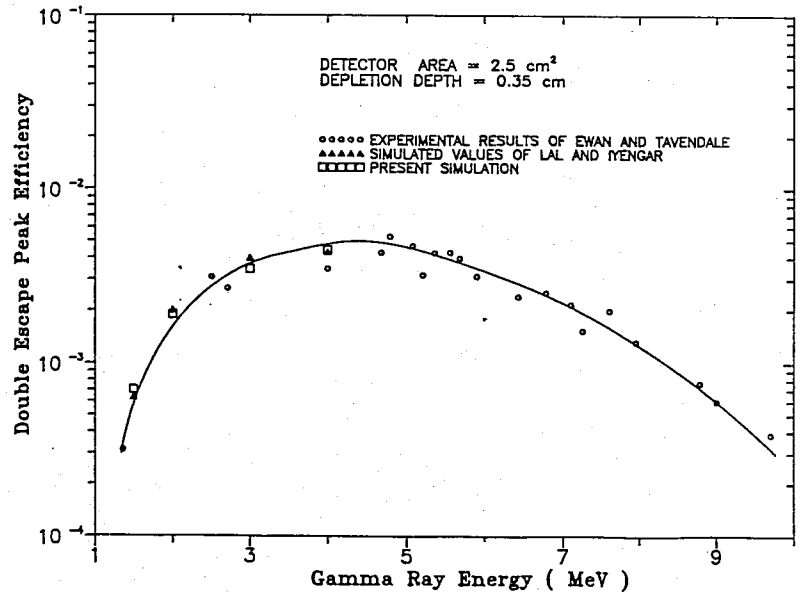

Fig. 5 Comparison of the simulated results of ϵ_{de} of planar Ge(Li) to the experimental values of Ewan and Tavendale [11] and the simulated results of Lal and Iyengar [6].

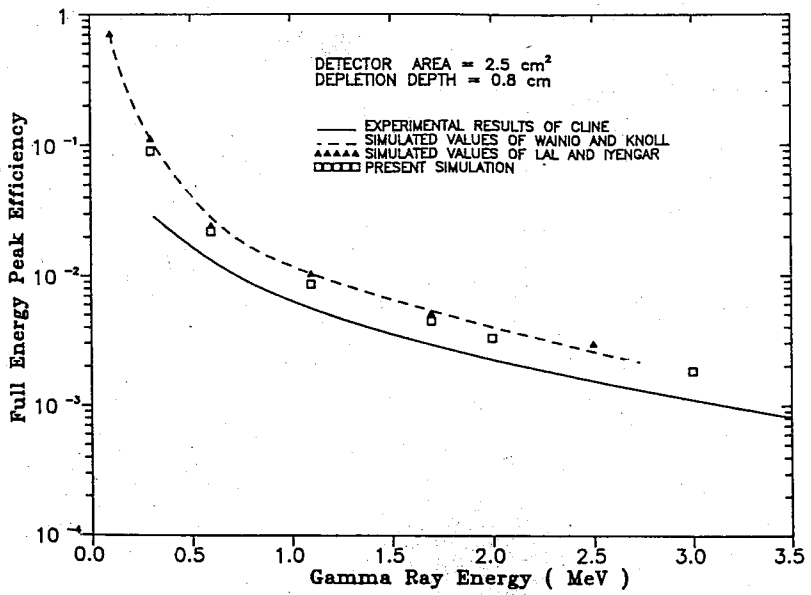

Fig. 6 Comparison of the simulated results of ϵ_{fe} of planar Ge(Li) to the experimental values of Cline [12] and the simulated results of Lal and Iyengar [6] and Wainio and Knoll [1].

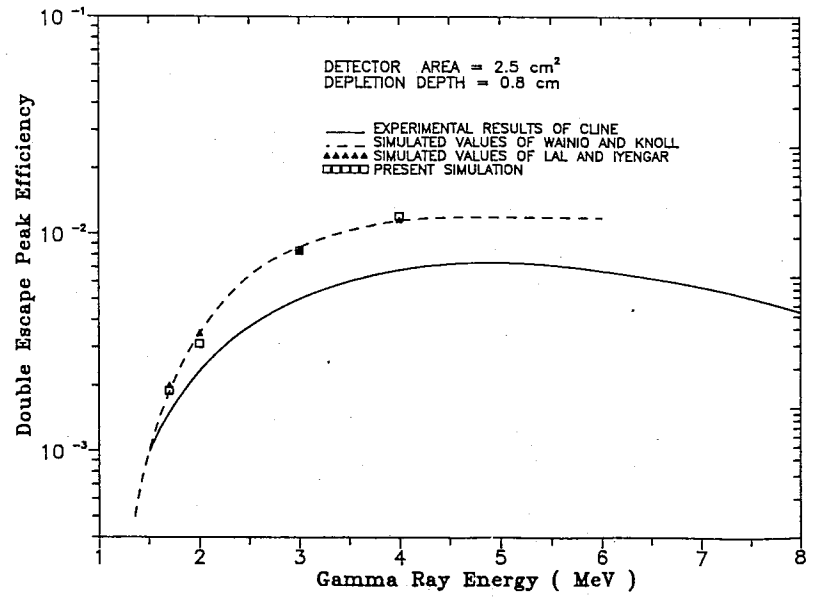

Fig. 7 Comparison of the simulated results of ϵ_{de} of planar Ge(Li) to the experimental values of Cline [12] and the simulated results of Lal and Iyengar [6] and Wainio and Knoll [1].

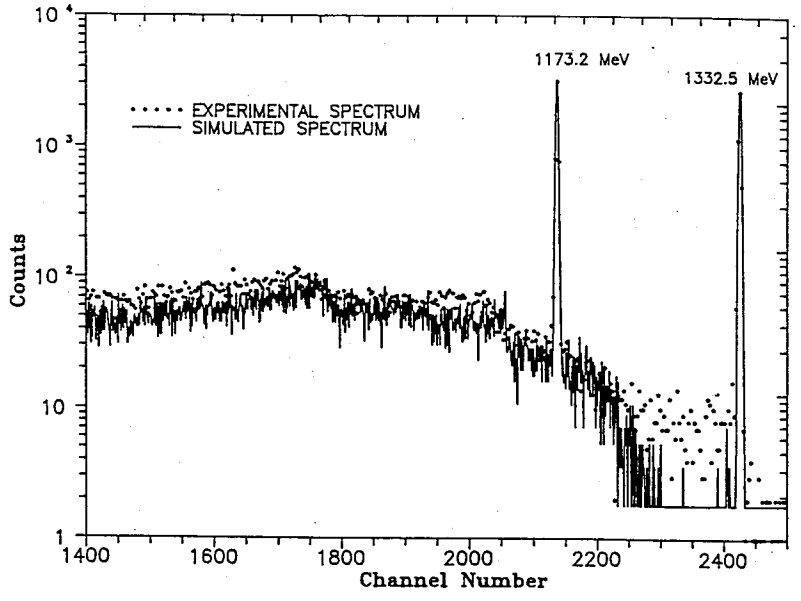

Fig. 8 Comparison of the simulated spectrum of ^{60}Co to the experimental spectrum of coaxial HpGe.

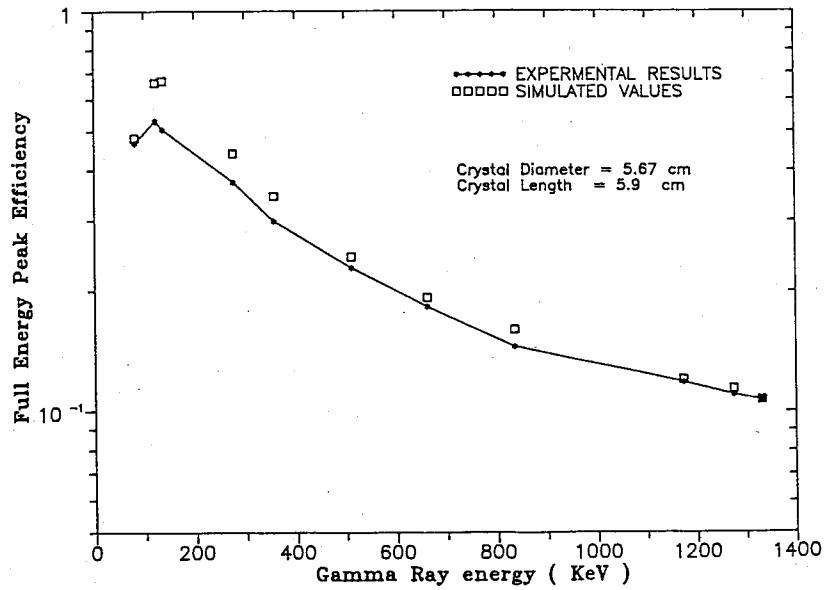

Fig. 9 Comparison of the simulated results of ϵ_{fe} to the experimental values of coaxial HpGe.

ELECTRIC AND MAGNETIC PROPERTIES OF CuFe, CuNi AND CuZn COMPOSITES AFTER THERMAL ANNEALING

Y. D. Yao

Institute of Physics, Academia Sinica
Taipei, Taiwan, 11529, R.O.C.

Abstract

CuFe, CuNi and CuZn composite samples were fabricated by means of the cold powder metallurgy technique. The temperature-dependent electrical resistivity ρ was studied between 4 and 1,100 K. The isothermal irreversible electrical resistivity changes due to thermal annealing was measured between 423 and 1,073 K. The coercive field H_c at room temperature is increased for CuFe and is decreased for CuNi after thermal annealing; the saturation magnetization M_s at room temperature is decreased for CuNi composite and do not changed for CuFe composite after thermal annealing. These results are explained by both the magnetostriction λ of Fe ($\lambda > 0$) and Ni ($\lambda < 0$) and the alloying effect. The results of alloying study during thermal annealing indicate that the solubility between two components is almost negligible for CuFe composites, is limited for CuZn composites and is nonlimited for CuNi composites; these results are consistent with the metallurgical phase diagrams.

Introduction

In recent years there has been much interest in the transport properties such as the electrical and magnetic behaviors of composite materials [1-7]. The different behaviors of the electrical and magnetic properties after thermal treatments are very important probes to understand the special characteristic of these composites. There is not only a need to improve and optimize these properties but also the possibility of devising materials showing novel electrical and magnetic behaviors [1,8]. In this investigation; we give experimental information on the influence of the electrical and magnetic properties of Cu-Fe, Cu-Ni and Cu-Zn composites after the thermal annealing treatment. Our experimental results and their significance are briefly presented below.

Experimental Consideration

The composite samples were fabricated following the same procedure that developed for metal-metal composite materials [2]. Using roughly 100 μm copper and nickel powders, and roughly 40 μm iron and zinc powders, we mixed the Cu and Fe powders together with 40 wt.% Fe, the Cu and Ni powders together with 50 wt.% Ni and the Cu and Zn powders together with 50 wt.% Zn. Copper tubes with roughly 12.7 mm outer diameter and roughly 11.1 mm inner diameter were used as an external jacket to contain these powders. The mixed powders were tapped into the Cu tube, the tube was evacuated, and then the compact was swaged and wire drawn to final size. Swaging techniques were used for the preliminary elongation, and the remaining deformation to a wire with a final outer diameter of roughly 0.25 mm for CuFe and CuNi composites and roughly 0.88 mm for CuZn composites was made by wire drawing.

The electrical resistivity of these composites was determined using the conventional four-probe technique. A D.C. current was maintained constant to about one part in 10^5 and the voltage was measured with an accuracy to a few nanovolts. Temperatures between 4K and 300K were achieved in a Displex closed-cycle refrigeration system (Model CS-308, Air Products). Temperatures between 300K and 1,100K were produced by a Marshall vacuum furnace. The furnace could be either evacuated or filled with helium gas. Magnetic measurements were made with a vibrating sample magnetometer at room temperature with the field along the fiber axis.

Results and Discussion

Fig. 1 (a to c) shows the temperature dependence of the electrical resistivity ρ of the Cu-Fe, Cu-Ni and Cu-Zn composite samples in the temperature range between 4K and 1,100K. The rate of the temperature change was roughly about 1K/Min. One low temperature run (4K—300K) and three high temperature runs have been taken for each sample. The whole measuring procedures are indicated by numerically labelled arrows in the figures. For Cu-Fe composite, the electrical resistivity data between 4K and 1,100K are completely reproducible. This means that the solubility between Cu and Fe is almost negligible in good agreement with the phase diagrams reported before [9]. For Cu-Ni and Cu-Zn composites, the room temperature electrical resistivity is increased after high temperature runs and the slope of the

electrical resistivity increases rapidly at high temperatures. These phenomena suggest that the alloying effect is significant at high temperatures.

Fig. 2 (a to b) shows the isothermal irreversible electrical resistivity data studied at 1,073K for Cu-Fe; at 973K, 773K and 573K for Cu-Ni; and at 623K, 523K and 423K for Cu-Zn. These electrical resistivity data were measured continuously as a function of time during isothermal annealing. From these figures, it is evident that the alloying effect is negligible for Cu-Fe composite; for Cu-Ni composite, the alloying effect does not manifest below 573K, however, the fast diffusion happens between Cu and Ni roughly at 973K for two weeks; according to the phase diagrams of CuNi [9-11], there is no limitation of the solubility between Cu and Ni.

The melting temperature of Zn is roughly 690K, therefore, the isothermal irreversible electrical resistivity studies of Cu-Zn composites below 690K can be used to analyze the alloying effect. In figure 2(b), for comparison, we plot the normalized electrical resistivity ρ_t/ρ_o, (i.e. the ratio of the electrical resistivity at time t to the electrical resistivity at the beginning of each annealing temperature) as a function of time t. The ρ_t/ρ_o vs t curves approach to the same value after roughly 2 days. This suggests that the effect of alloying seems to be completed after roughly 2 days at annealing temperatures between 423K and 623K. According to the phase diagram of CuZn [9], the solubility of Zn in Cu between 623K and 423K is roughly $33 \sim 35\%$.

Figure 3 represents the room temperature saturation magnetization of the Cu-Ni composite as a function of annealing time at 573K and 973K. The value of the saturation magnetization drops slowly for 573K, and drops very fast at the beginning for 973K. These decreases means that some electrons of the copper atoms seek the place of the lowest energy in the system and find it in the 3d shell of the nickel atoms rather than in the copper atoms to which they originally belonged. This behavior lowers the saturation magnetization of the system. However, the room temperature saturation magnetization of the Cu-Fe composite does not varied significantly after annealing. These behaviors are consistent with the solubility of CuNi and CuFe alloys.

Fig. 4 shows the coercive field H_c at room temperature of CuFe and CuNi composite as a function of time annealed at 573K. After annealing, the value of H_c increases for CuFe composite and decreased for CuNi composite. It seems that the values are saturated after 50 minutes. We suggest that it could be related to the positive value of magnetostriction ($\lambda > 0$) for iron and negative ($\lambda < 0$) for nickel. Because the magnetoelastic energy [12] of the domain magnetization depends on the sign and the magnitude of magnetostriction. The thermal annealing should

result strain released in the samples; from our experimental data, it seems to induce magnetic anisotropy in CuFe system and to release magnetic anisotropy in CuNi system.

In conclusion, this is the first time that the electrical and magnetic properties of Cu-Fe, Cu-Ni and Cu-Zn composites after thermal annealing is reported. We have found that the saturation magnetization M_s at room temperature is decreased for CuNi composite and is unaffected for CuFe composite after thermal annealing. However, the coercive field H_c at room temperature is increased for Cu-Fe composite and is decreased for Cu-Ni composite after thermal annealing; these effects could be concerned with the magnetostriction, the magnetic domain shift and the alloying effect. The alloying study indicates that the solubility between two elements is almost negligible for CuFe composites, is limited for CuZn composites and is non-limited for CuNi composites. These results are in good agreement with the metallurgical phase diagrams. At present our data are not sufficient to allow us to study the solid state diffusion quantitatively. Further experimental and theoretical works are needed to accurately analysis the solid state diffusion.

Acknowledgements

The author is grateful to the National Science Council of R.O.C. for the financial support of this work, special thanks are extended to Mr. I. S. Chen, Mr. G. Yur and Mr. G. F. Liao for their laboratory assistances.

References

1. B. Bhushan, S. C. Kashyap and K. L. Chopra, Appl. Phys. Lett., 38, 160 (1981).
2. Y. D. Yao and S. Foner, Appl. Phys. Lett. 43, 697 (1983).
3. T. Slupkowski, Phys. Stat. Sol. 83A, 329 (1984).
4. Y. Termonia and S. Reich, Phys. Lett. 111A, 138 (1985).
5. I. S. Chen and Y. D. Yao, Chin. J. Mat. Sci. 18A, 78 (1986).
6. Y. D. Yao and G. Yur, Chin. J. Mat. Sci. 20, 181 (1988).
7. Y. Ishii and M. Sato, J. Appl. Phys. 59, 880 (1986).
8. D. Abukay, K. V. Rao, S. Arajs and Y. D. Yao, Fib., Sci. Tech. 10, 313 (1977).
9. M. Hansen and K. Anderko, Constitution of Binary Alloys, McGraw-Hill Book Co., New York (1958).
10. R. P. Elliott, Constitution of Binary Alloys, First Supplement, McGraw-Hill Book Co., New York (1965).
11. F. A. Shunk, Constitution of Binary Alloys, Second Supplement, McGraw-Hill Book Co., New York (1969).
12. S. Chikazumi, Physics of Magnetism, (English Edi.: S. H. Charap) John Wiley & Sons, Inc. (1964).

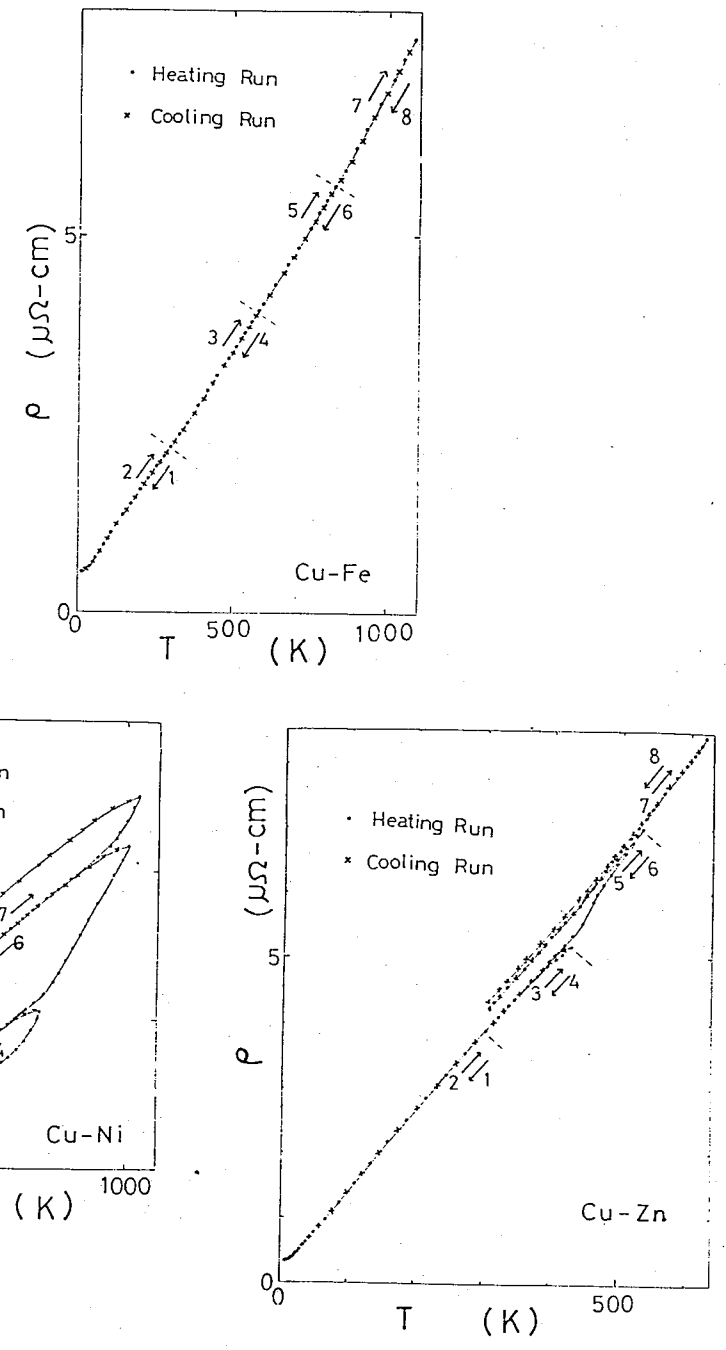

Fig. 1 Electrical resistivity as a function of absolute temperature for (a) Cu-Fe composite, (b) Cu-Ni composite, and (c) Cu-Zn composite.

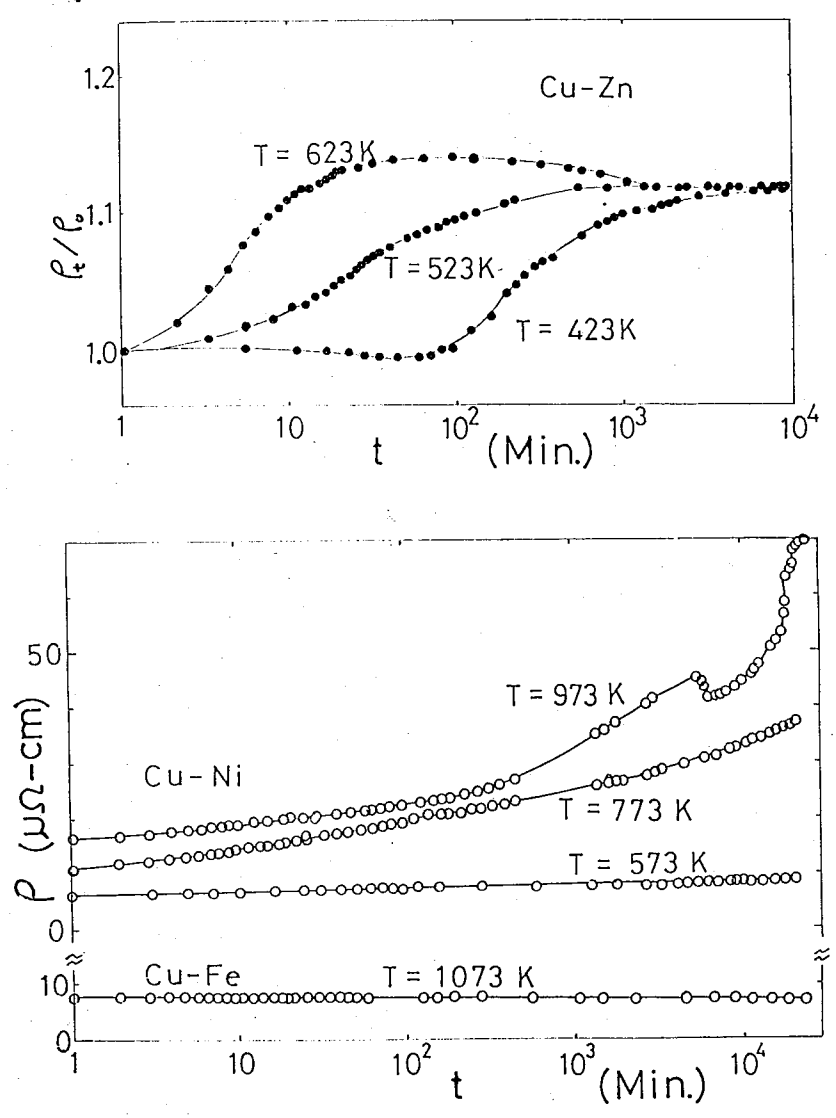

Fig. 2 Electrical resistivity as a function of annealing time for (a) Cu-Fe and Cu-Ni composites, and (b) Cu-Zn composite.

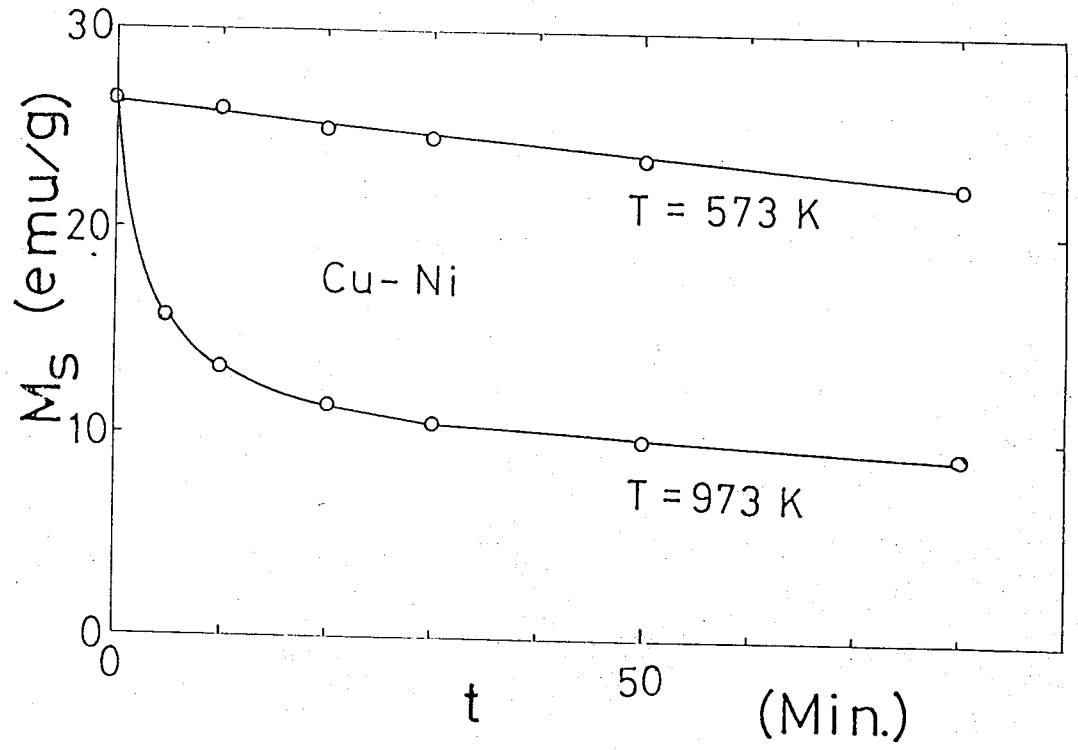

Fig. 3 Room temperature saturation magnetization of Cu-Ni composite as a function of annealing time.

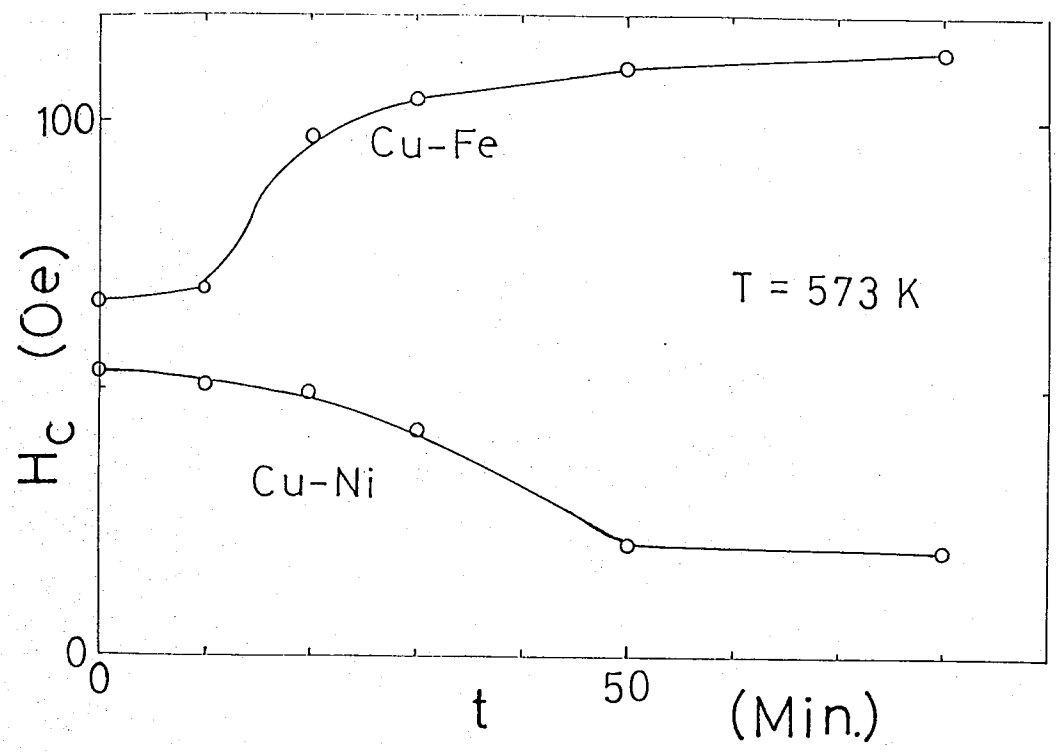

Fig. 4 Room temperature coercive field of Cu-Fe and Cu-Ni composites as a function of annealing time.

NALOXONE AND HALOPERIDOL DECREASE THE FREQUENCY OF LH PULSATILE RELEASE

Wei-Kung Wang[1,2], Tse-Lin Hsu[1], Yi Chiang[1]

1 Biophysics Laboratory, Institute of Physics, Academia Sinica, Taipei, 11529, Taiwan, R.O.C.

2 Institute of Biomedical Engineering, National Yang-Ming Medical College

Abstract

For mathematical simplicity, a negative feedback hypothesis between DA and GnRH was suggested as DA $\overset{+}{\rightleftharpoons}$ GnRH $\overset{+}{\rightarrow}$ LH. The concentrations of GnRH and LH would be in following form: concentration of GnRH = $A\sin(\sqrt{K_1K_2}\,t + \Phi)$ concentration of LH = $Ce^{-Kt} + \frac{A\alpha}{\sqrt{K^2+K_1K_2}}\sin(\sqrt{K_1K_2}\,t + \Phi + \Phi')$ which suggests the naloxone and haloperidol injected into the ovariectomized rats would slow down the frequency of the LH pulsatile release. We did these experiments and found results consistent with this hypothesis.

Introduction

Current evidence on dopamine regulation of LH is confusing and conflicting, both excitatory and inhibitory action have been postulated [1,2,3,4,5,6]. Multiple dopaminergic pathways [6] and several different kind dopamine receptors [4] might also involved. We selected a simplified situation of LH pulsatile release in the overiectomized rat to study.

Without the influence from the ovary, the LH concentration in the blood of the female animal would simply oscillate with regular frequency and amplified amplitude [7,8]. Previously, we have reported that GnRH might inhibit the DA synthesis through the opiate receptors [9]. Excitatory effect of DA in regulation of LH release do exist [1,4,6,10,11,12]. While GnRH is closely correlated with the release of LH [4], we therefore suggested a negative feedback model as: DA $\overset{+}{\rightleftharpoons}$ GnRH $\overset{+}{\rightarrow}$ LH for LH pulsatile release in physiological condition.

Simple mathematical derivations showed that the concentrations of both GnRH and LH should oscillate as sine waves in a simple mathematical sense (in real

physiology, it will be distorted by other factors). Both frequency and amplitude would be changed if the feedback constants between GnRH and DA were changed.

The opiate antagonist naloxone [13], and the dopamine antagonist haloperidol [14] were chosen to test this model. Both of the drugs were effective in slowing down the LH pulsatile release (lower frequency) as expected.

Theory

Assume the simplified negative hypothesis model between DA and GnRH, DA $\overset{+}{\underset{-}{\rightleftharpoons}}$ GnRH $\overset{+}{\rightarrow}$ LH is correct, the concentration relation can be described by the following equations:

$$\frac{dx}{dt} = K_1 Y \qquad (1)$$

$$\frac{dY}{dt} = -K_2 X \qquad (2)$$

X: concentration of GnRH x-C_0

Y: concentration of dopamine y-C_1

Z: concentration of LH z-C_2

$K_1 Y$: GnRH synthesis rate in correspondence to Y amount of dopamine stimulation

$-K_2 X$: dopamine synthesis rate in correspondence to X amount of GnRH inhibition

αX: LH synthesis rate in correspondence to X amount of GnRH stimulation

KZ: LH decay rate in the blood

$$\frac{dZ}{dt} = \alpha X - KZ \qquad (3)$$

C_0 : average concentration of GnRH

C_1 : average concentration of dopamine

C_2 : average concentration of LH

From (1), (2) we have $\frac{d^2 X}{dt^2} = -K_1 K_2 X$ (4′)

Solve the equation (4′): $X = A\sin(\sqrt{K_1 K_2}\, t + \Phi)$ (4)

From (3), (4) $\frac{dZ}{dt} = A \sin(\sqrt{K_1 K_2}\, t + \Phi) - KZ$ (5′)

From (5′)

$$Z = Ce^{-Kt} + \frac{A\alpha}{\sqrt{K^2 + K_1 K_2}} \sin(\sqrt{K_1 K_2}\, t + \Phi + \Phi') \qquad (5)$$

$\Phi' = \tan^{-1}(-\sqrt{K_1 K_2}/K)$. A, Φ, C depend on initial condition of X and Z.

Since the term Ce^{-Kt} will decay quickly, which suggests that the concentration of LH shall oscillate as a sine wave in a simple mathematical sense with the amplitude $A \propto / \sqrt{K^2 + K_1 K_2}$ and frequency $f = \frac{\sqrt{K_1 K_2}}{2\pi}$, this may well be the source of the LH pulsatile release which does show a periodic property similar to sine wave. We can also see that if any of the K_1, K_2, K, or α is changed, it will change the amplitude or the frequency of the GnRH and LH pulsatile release. Table I summarizes these relations.

Using this hypothesis, drug effect could be analyzed as following: Naloxone would block the opiate receptor [13], therefore a larger dose of GnRH would be needed to give similar effect on DA[15]. This was equivalent to the reduction of K_2. From table I, which led the LH concentration to oscillate slower and with a somewhat larger amplitude. Similarly the haloperidol would reduce K_1. The K_1 and K_2 were equivalent in the equation (5). Therefore the LH concentration would change in a similar way. However, if we injected in certain amount of GnRH, that is increased the initial level of x, since none of the constant was changed, we should see a sharp increase of the LH level, nonetheless this effect would be quickly decayed. This can be demonstrated easily by solving the differential equation (3) with X as a delta function of time. Or we may simply fit equation (5) with the initial condition which gives a larger C.

Material and Methods

To measure the change of LH concentration with respect to time, the rat was bled continuously for 4-8 hours. The bleeding procedure has been described by S.V. Drouva and R.V. Gallo [16]. Briefly, a day before the bleeding, a polyethylene catheter was inserted through the right external jugular vein to approach the right atrium of a young female ether anesthetized Sprague-Dawley rat which had been ovariectomized for six weeks. The catheter was passed under the skin and fixed on the back neck with a light spring sewed outside as protection. A bi-direction pump was connected with the catheter which permitted continuously access to the venous circulation without the animal's being restrained. Twenty minutes before bleeding,

2.0 mg/kg body weight naloxone or 1.3 mg/kg body weight haloperidol was injected into the rat through the catheter with 200 $\mu\ell$, 200 units heparin containing physiology saline as carrier. Two 5 $\mu\ell$ blood samples were taken by way of the same catheter every 5 minutes. The blood samples were centrifuged with 100 $\mu\ell$ phosphorous buffer with 1% normal rabbit serum at 1000 rpm for 10 minutes, 80 $\mu\ell$ supernatant was taken and frozen at $-70°C$ until the RIA process started. RIA procedure was modified from the method of Niswender et al [17]. We reduced the volume of incubation medium to increase the sensitivity. Buffer was prepared with 10 mM sodium phosphate, 0.15 M NaCl and 0.02% NaN_3 at pH 7.5. 25 $\mu\ell$ NIADDK anti-r-LH-S-8 of final dilution 1:280000 in buffer with 0.05M EDTA was incubated with the sample in cold room for 2 days, then 50 $\mu\ell$ ^{125}I-LH about 3500 cpm was added and incubated for another two days. Finally the LH-antibody complex was precipitated with 50 $\mu\ell$ second antibody and 180 $\mu\ell$ 10% PEG. 0.1ng/tube, 0.06ng/tube, and 0.03ng/tube of NIADDK-rLH-RP-2 were used as standard which was 61 times more potent as NIADDK-rLH-RP-1. Data would be discarded if the correlation factor was less than 0.999.

The periodicities of the LH pulses were analyzed by a permutation rank test described by R. H. Odell, Jr. [18]. We took the fourier transform of the autocorrelation function of the linear trend removed LH concentration time series. The existence of significant peaks in power spectral ordinate was then determined by comparing 100 times of the original power spectrum with the power spectrum obtained by randomly perturbing the LH concentration time series.

The significance level was chosen arbitrarily to be 0.05, that is we chose the 95th percentile to be the critical limit for judging a power spectral estimate to be significant.

This method was proved very useful in solving the periodicity problem in short noisy time series [18,19]. Flow chart was given as Fig. 1.

Results

Both naloxone and haloperidol would slow down the LH pulsatile release which were shown on Fig. 2 and Table II. The average frequency on pre-drug control was 28.8 ± 8.3 min./pulse (No. = 9), however with the naloxone or haloperidol added the frequency changed to be 69.9 ± 35.7 min./pulse (No. = 8) and 82.4 ± 40.4 min./pulse (No. = 5) respectively. There was no significant difference of the amplitude between control and drug set.

Discussion

Two pharmacologically independent drugs, naloxone and haloperidol showed the similar slowing down effect on the frequency of the LH pulsatile release. The indistinguishable amplitude in our data may due to the square root nature of the amplitude (Eq. 5) or our data analysis method [18]. However, Bhattacharya, A.N. et. al. [10] had reported that single injection of chlorpromazine or haloperidol in ovariectomized rhesus monkey would inhibit LH release, then after certain time the LH pulsatile secretory pattern would suddenly resume and with much slower frequency and larger amplitude. Our hypothesis seems to be the first to explain this peculiar phenomena. When a large dose of drug was suddenly given to the animal, it would completely block the DA receptors hence block the GnRH release. However, when the time passed by, part of the drug would be cleared out, the GnRH releasing axons would be free from the complete blocking, then the DA started to stimulate GnRH release. (It could also be seen that the larger the dose used, the longer the inhibition time existed in Bhattacharya's report [10]).

An axoaxonally interaction [3] was suspected to be responsible for this negative feedback relation of LH pulsatile release. In order to get a clear picture, the drug effect on DA presynaptic receptors must also be considered. For example, apomorphine stimulated DA postsynaptic receptors [12], however it also strongly blocked DA synthesis on DA presynaptic receptors [20], hence its total effect on DA signal transmission was not clear. For haloperidol, it blocked DA postsynaptic receptors [14], but it would not influence the DA auto-inhibition on DA presynaptic receptors [21]. It clearly decreased DA signal transmission.

The LH oscillation of the old ovariectomized animal has been found with lower frequency and amplitude [15]. Since the pitutitary response to GnRH was decreased [22,23], and the response and output of dopaminergic neurons were also decreased in old animal [24], according to our hypothesis, K_1, K_2, and the α should all be reduced which in turn would reduce both the amplitude and frequency of the LH oscillation. We get a few data indicated that the old rat injected with naloxone or haloperidol would further lengthent he period of the LH pulsatile release. Naloxone would lengthen the period from 75 mins/pulse of control to 115 mins/pulse, haloperidol would lengthen the period from 90 mins/pulse of control to 130 mins/pulse.

What we presented here is just a trial of using mathematics to help solving physiological problems. Actually this feedback mechanism of DA and GnRH may not be a direct one. It may go through some other intermediates. However to explain

the effect of naloxone and haloperidol on the LH pulsatile release, we tried to give a feasible quantitative approach. The interpretation is compatible with most of the available data. It will be strengthened, modified or even disproven when more evidence is emerged.

References

1. Dickerman S, Kledzik G, Gelato M, Chen HJ and Meites J. (1974). Effects of haloperidol on serum and pituitary prolactin, LH and FSH and hypothalamic PIF and LRF. Neuroendocrin. 15; 10-20.
2. Lofstrom A, Agnati LF and Fuxe K. (1977). Evidence for an inhibitory dopaminergic and stimulatory noradrenergic hypothalamic influence of PMS-induced ovulation in the immature rat. Neuroedocrin. 24; 270-288.
3. McNeill TH and Sladek Jr. JK. (1978). Fluorescence-immunocytochemistry: simultaneous localization of catecholamines and gonadotropine-releasing hormone. Science 200; 72-74.
4. Sarkar DK and Fink G. (1981). Gonadotropin-releasing hormone surge: possible modulation through postsynaptic — adreno receptors and two pharmacologically distinct dopamine receptors. Endocrinol. 108; 862-867.
5. Schneider HPG and McCann SM. (1970). Mono- and indolamines and control of LH secretion. Endocrinol. 86; 1127-1133.
6. Weiner RI and Ganong WF. (1978). Role of brain monoamines and histamine in regulation of anterior pituitary secretion. Physiol. Rev. 58; 905-976.
7. Gallo RV. (1981). Pulsatile LH release during the ovulatory LH surge on proestrous in the rat. Biol. Reprod. 24; 100-104.
8. Gay VL, Sheth NA. (1972). Evidence for a periodic release of LH in castrated male and female rats. Endocrinol. 90; 158-162.
9. Wang WK, Jeng LC, Chiang Y and Chien NK. (1982). Inhibition of dopamine biosynthesis by gonadotropin-releasing hormone in rat. Nature. 296; 354.
10. Bhattacharya AN, Dierschke DJ, Yamaji T and Knobil E. (1972). The pharmacologic blockade of the circhoral mode of LH secretion in the ovariectomized Rhesus monkey. Endocrinol. 90; 778-786.
11. Linnoila M and Cooper RL. (1976). Reinstatement of vaginal cycles in aged female rats. J. of Pharm. Exp. Therap. 199; 477-482.
12. Schneider HPG and McCann SM. (1969). Possible role of dopamine as transmitter to promote discharge of LH-releasing factor. Endocrinol. 85; 121-132.

13. Snyder SH and Goodman RR. (1980). Multiple neurotransmitter receptors. J. of Neurochem. 35; 5-15.
14. Miller RJ, Horn AS and Iversen LL. (1974). The action of neuroleptic drugs on dopamine stimulated adenosine cyclic 3′, 5′monophosphate production in rat neostriatum and limbic forebrain. Molec. Pharm. 10; 759-766.
15. Ester KS, Simpkins JW and Chen CL. (1980). Alteration in pulsatile release of LH in aging female rats. Proc. Socl. Exp. Biol. Med. 163; 384-387.
16. Drouva SV and Gallo RV. (1976). Catecholamine involvement in episodic luteinizing hormone release in adult ovariectomized rats. Endorinol. 99; 651-658.
17. Niswender GD, Midgley Jr. AR, Monroe SE and Reichert LE. (1968). Radioimmunoassay for rat luteinizing hormone with anti-ovine LH serum and ovine LH-^{131}I*(33129). J. Proc. Soc. Exp. Biol. Med. 128; 807-811.
18. Odell Jr. RH. (1975). A permutation test for periodicities in short noisy time series. Annals of Biomed. Engineering. 3; 160-180.
19. Yates PE. (1981). Analysis of endocrine signals: The engineering and physics of biochemical communication system. Biol. of Reprod. 24; 73-94.
20. Wang WK, Hai TY and Chiang Y. (1980). Different inhibitory effects of dopa, dopamine and apomorphine on dopamine biosynthesis. Bull. Inst. Zool. Academia Sinica. 19(1); 33-37.
21. Wang WK, Hsu TL and Chiang Y. (1984). Effect of bromocriptine and haloperidol on the dopamine auto-regulation. Annual Report of the Inst. Phys. Acad. Sinica. 14; 81-87.
22. Cooper RL, Roberts B, Rogers DC, Seay SG and Conn PM. (1984). Endocrine Status Versus Chronologic age as predictors of altered luteinizing hormone secretion in the "Aging rat"., Endocrinol. 114; 391-396.
23. Watkins BE, Meites J and Riegle GD. (1975). Age related changes in pituitary responsiveness to LRH in the female rat. Endocrinol. 97; 543-548.
24. Finch CE. (1979). Neuroendocrine mechanism and aging. Federation Proc. 38; 178-183.
25. Gabriel SM, Simpkins JW and Kalra SP. (1983). Modulation of endogenous opioid influence on luteinizing hormone secretion by progesterone and estrogen. Endocrinol. 113; 1806-1811.

Table I. Relations between the LH pulsatile release and the constants in the equation

$$\text{Eq.: } Z = Ce^{-Kt} + \frac{A\alpha}{\sqrt{K^2 + K_1 K_2}} \sin(\sqrt{K_1 K_2}\, t + \Phi + \Phi') \text{ *}$$

Eq. constant	Frequency	Amplitude	Explanation
K_1 or K_2 ↑	↑	↓	
K_1 or K_2 ↓	↓	↑	**inject HD, or Nal.
α ↓ (or K ↑)		↓	desensitization due to continuously GnRH infusion[6].
None of K_1, K_2, K, A, or α is changd, only C increased	Z will suddenly ↑ increase then decay exponentially with time		inject single dose of GnRH

* We may analyze any periodical (pulsatile) function by Fourier Transform, therefore sine function is always a good first approximation.

** Too much HD will completely block the DA stimulation effect on GnRH, therefore will decrease the LH concentration [10]. Too much naloxone will completely block the GnRH inhibition effect on DA, therefore DA will stimulate GnRH synthesis without negative feedback control, LH will increase then [24].

Table II. Drug effect on LH pulsatile release

	Drug	Period	
	control	28.8 ± 8.3 mins/pulse	(9)
**	naloxone	69.9 ± 35.7 mins/pulse	(8)
***	haloperidol	82.4 ± 40.0 mins/pulse	(5)

* data were presented as mean ± S.D. (number of experiments)

** and *** significant different $p < (0.01)$ from control set

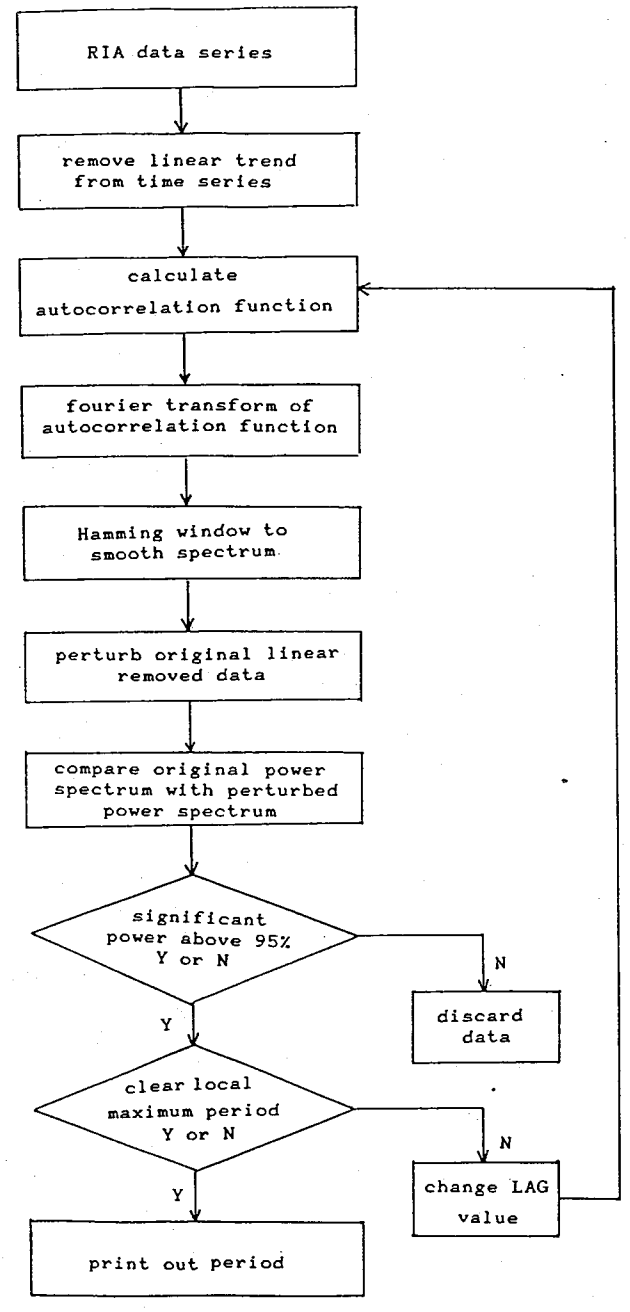

Fig. I. Flow chart of data analysis

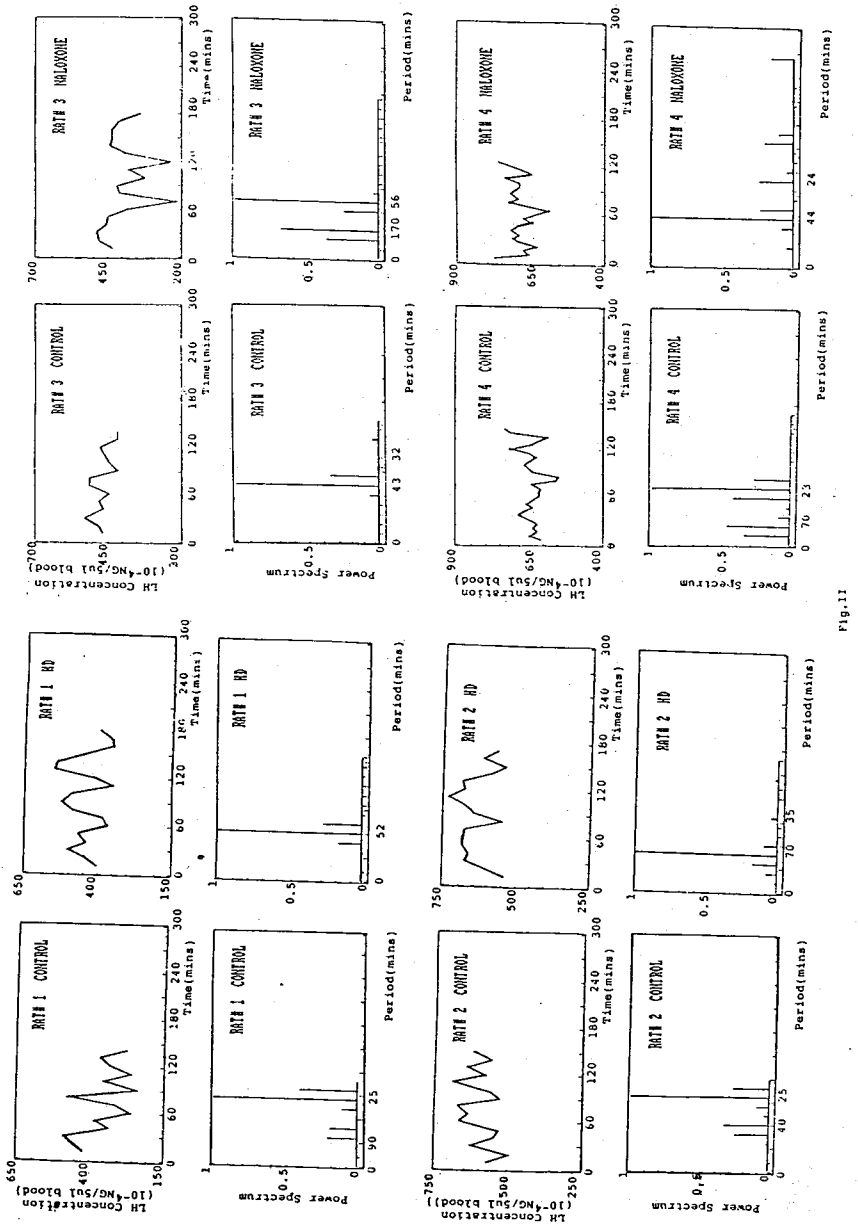

Fig.11

Fig. II. Drug effect on LH pulsatile release. Drugs were injected into the rat 20 minutes before bleeding, 200 $\mu\ell$, 200 units heparin containing physiology saline was used as carrier, 2.0 mg/kg naloxone and 1.3 mg/kg haloperidol were used separately. NIADDK-rLH-RP-2 was used as RIA reference preparation. Computer analyzed, normalized power spectrum was given under each experiment.

EFFECT OF FLUID STRATIFICATION ON THE VORTEX SHEDDING FLOW FROM A CYLINDER

Robert R. Hwang and S. H. Lin

Institute of Naval Architecture, Taiwan Univ., and Institute of Physics, Academia Sinica, Taipei, Taiwan, R.O.C.

Abstract

Finite-difference techniques based on boundary-fitted coordinates have been developed to study the flow of a stably stratified viscous fluid past a circular cylinder. A time dependent approach is used and the implicit solution utilizes the vorticity-stream formulation. All field equations are approximated using central differences and solved simultaneously at each time step by SOR iteration. Results show that the stratification tends to retard the vortex shedding from two sides of the cylinder and to narrow down the wake behind the cylinder. With increasing stratification, the drag on the surface first decreases and then increases. These solutions also disply that the periodic configuration of the oscillatory character of the wake flow decreases with the increase of the stratification.

Introduction

The uniform flow of homogeneous fluids past a circular cylinder is a classic problem in fluid mechanics. At low Reynolds numbers (Re < 40), a steady symmetrical flow exists. As the Reynolds number increasing to certain values, the flow in the wake of the obstacle becomes unsteady and periodic, and transforms into a Karman vortex street. In a result, the forces that are imposed by the fluid upon the cylinder become oscillatory in nature. Studies on the problems of vortex street development and shedding behind the cylinder for a unform flow of homogeneous fluid have been reported by many researchers [1,2,5,6]. The effect of the stratification of ambient on the configuration of flow pattern such as the formulation of wake, the shedding mechanism of vortex, etc., on the other hand, has not been widely investigated.

Most studies [3,4,6,7,10] of the density-stratified fluid flow over an obstacle were dealt with the ambient in a strong density stratification. In such stratified fluid

flow, one of the striking phenomena obtained is the strong upstream influence (the upstream wake) of an obstacle when the grativy effect is compared to, or more than the inertial effect. The other characteristics are the lee waves formation downstream behind the obstacle. The study of Pao [7] concluded that the upstream influence and the reverse wake of lee waves were decreased in the decreasing of the ambient density stratification. What is the effect of the weak stratification on the oscillatory wake development and the vortex shedding behind the cylinder is till not investigated.

This study then concerns the laminar flow past a circular cylinder with uniform upstream velocity and weak density gradient. Effects of gravity, viscosity and obstacle shape simultaneously on uniform flow over a circular cylinder are investigated. Separation and vortex shedding which depend on viscous effects and obstacle shape in the interaction with the mean density stratification are considered in the flow problem. In solving the flow problem, a time dependent approach in utilizing the vorticity-stream function formulation is used. With the boundary-fitted coordinates, all field equations are discretilized into finite difference approximation and solved simultaneously at each time step on the transformed domain. Numerical computations for flow of Re = 100 are carried out with the variations of density gradients.

Formulation of flow problems

We consider an incompressible viscous flow of linearly stratified fluid past a circular cylinder of diameter D with constant uniform speed U. Fig. 1 shows the geometry and coordinates of the flow problem. Far upstream, in the frame of reference of the cylinder, the following conditions are assumed to exist:

$$\begin{aligned} &\tilde{\rho} = \rho_0 (1 - \beta \tilde{z}) \\ &\tilde{u} \to U \\ &\tilde{w} \to 0 \end{aligned} \tag{1}$$

in which ρ_0 is the density of fluid very far upstream at the level of the cylinder and

$$\beta = \lim_{\tilde{x} \to -\infty} | d\rho / d\tilde{z} | / \rho_0$$

is the stratification parameter. U is the constant velocity in the undisturbed farther distance.

With the assumptions that the flow is incompressible and laminar, the fluid has uniform transport properties, and that β is so small that the Boussinesq approximation is valid, the governing equations in vorticity-stream function formulation and the diffusion equation in density are

$$\frac{\partial \tilde{\zeta}}{\partial \tilde{t}} + u \frac{\partial \tilde{\zeta}}{\partial \tilde{x}} + w \frac{\partial \tilde{\zeta}}{\partial \tilde{z}} = -\frac{1}{\rho_0} \frac{\partial \tilde{\rho}}{\partial \tilde{x}} g + \nu \tilde{\nabla}^2 \tilde{\zeta} \tag{2}$$

$$\tilde{\nabla}^2 \tilde{\psi} = -\tilde{\zeta} \tag{3}$$

$$\frac{\partial \tilde{\rho}}{\partial \tilde{t}} + \tilde{u} \frac{\partial \tilde{\rho}}{\partial \tilde{x}} + \tilde{w} \frac{\partial \tilde{\rho}}{\partial \tilde{z}} = D_m \tilde{\nabla}^2 \tilde{\rho} \tag{4}$$

$$\text{and } \tilde{u} = \partial \tilde{\psi} / \partial \tilde{z} \quad , \quad \tilde{w} = -\partial \tilde{\psi} / \partial \tilde{x} \tag{5}$$

where $\tilde{u}$ and $\tilde{w}$ are the velocity components in $(\tilde{x}, \tilde{z})$ directions, $\tilde{\rho}$ is the density, $\tilde{t}$ is the time, $\tilde{\nabla}^2 = \partial^2/\partial \tilde{x}^2 + \partial^2/\partial \tilde{z}^2$, and ν and D_m are the kinematic viscosity and the molecular diffusivity of fluid respectively. $\tilde{\zeta}$ is the vorticity defined by

$$\tilde{\zeta} = \partial \tilde{w} / \partial \tilde{x} - \partial \tilde{u} / \partial \tilde{z} \tag{6}$$

For convenience, Eqs. (2) through (5) can be normalized to give a set of non-dimensional equations by defining a length D, the diameter of the cylinder and a velocity U, the velocity very far upstream from the cylinder as characteristic parameters. This dimensionless quantities are specified as follows:

$$x = \tilde{x}/D, \; z = \tilde{z}/D, \; u = \tilde{u}/U, \; w = \tilde{w}/U$$

$$t = \tilde{t}/\frac{D}{U} \; , \quad \psi = \tilde{\psi}/UD, \; \zeta = \tilde{\zeta}/\frac{U}{D} \; , \quad \rho = \frac{\rho - \rho_0}{\Delta \tilde{\rho}} \tag{7}$$

$$\text{Re} = UD/\nu, \; S_c = \nu/D_m \text{ and}$$

$$F = U/\sqrt{(\Delta\tilde{\rho}/\rho_0)gD}$$

where $\Delta\tilde{\rho}$ is the density difference between the levels of the upper and the lower surfaces of the cylinder infinitely far upstream. Re, Sc and F are Reynolds number, Schmidt number and the densimetric Froude number respectively. The dimensionless governing equations now become

$$\frac{\partial\zeta}{\partial t} + \frac{\partial\psi}{\partial z}\frac{\partial\zeta}{\partial x} - \frac{\partial\psi}{\partial x}\frac{\partial\zeta}{\partial z} = \frac{1}{Re}\nabla^2\zeta - \frac{1}{F^2}\frac{\partial\rho}{\partial x} \tag{8}$$

$$\nabla^2\psi = -\zeta \tag{9}$$

$$\frac{\partial\rho}{\partial t} + \frac{\partial\psi}{\partial z}\frac{\partial\rho}{\partial x} - \frac{\partial\psi}{\partial x}\frac{\partial\rho}{\partial z} = \frac{1}{Re\,Sc}\nabla^2\rho \tag{10}$$

$$\text{and } u = \partial\psi/\partial z,\ w = -\partial\psi/\partial x \tag{11}$$

The governing Eqs. (8) through (11) subject to the appropriate initial and boundary conditions are to be solved in studying the uniform flow with weakly density stratified fluid past a cylinder. The initial and boundary conditions on a far from the cylinder are summarized as

$$\begin{aligned}
&(1)\ \ \psi = \psi_p\ ,\ \zeta = 0\ ,\ \ \rho = -\psi_p \text{ for } t = 0 \text{ and } \psi_p = -(z + z/\sqrt{x^2 + z^2}) \\
&(2)\ \ \psi = 0\ \ ,\ \zeta = \zeta_b\ ,\ \ \rho = 0 \text{ on cylinder} \\
&(3)\ \ \psi = \psi_p\ ,\ \zeta = 0\ ,\ \ \rho = -\psi_p \text{ far from cylinder}
\end{aligned} \tag{12}$$

The transformation

To simplify the numerical solution of the problem, the flow physical region as shown in Fig. 2, cut off suitably upstream, is transformed to a computational region

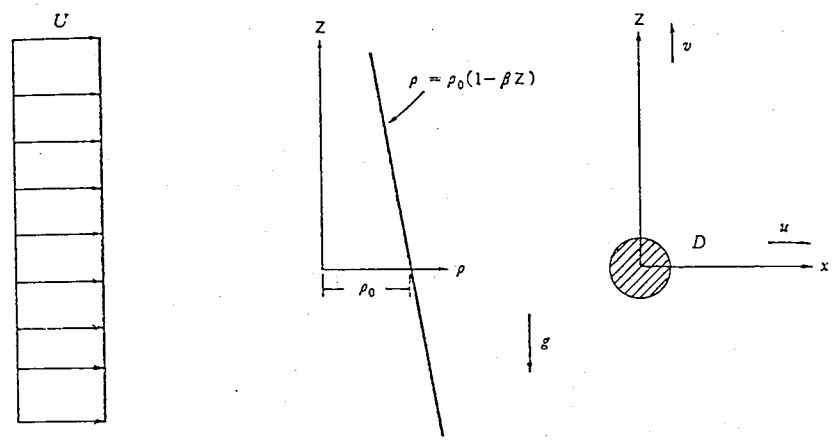

Fig. 1. The geometry of the problem.

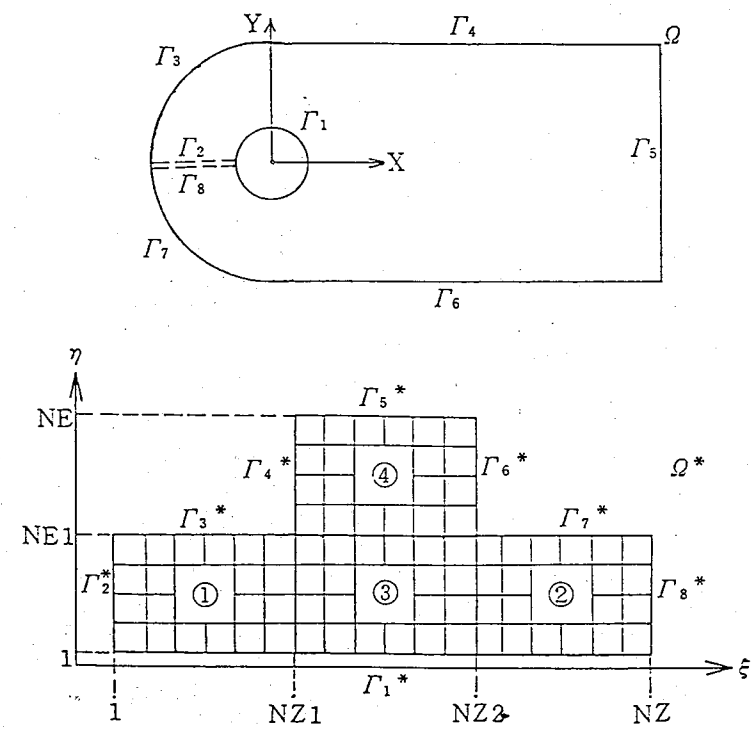

Fig. 2. Transformation of coordinate system.

which is composed of rectangles. The cylinder is mapped onto the line Γ_1^*, the far downstream onto Γ_5^*, the upper and lower far boundaries onto Γ_4^* and Γ_6^* respectively, and the upstream boundary splitting onto Γ_3^* and Γ_7^*. The boundaries Γ_2^* and Γ_8^* represent cut within the fluid.

As to transformations computed by Thompsonet et al [8,9], the curvilinear coordinates (ξ, η) are generated by solving an elliptic system of the form

$$\xi_{xx} + \xi_{yy} = P(\xi, \eta, t) \tag{13}$$

$$\eta_{xx} + \eta_{yy} = Q(\xi, \eta, t) \tag{14}$$

with appropriate boundary conditions. The source functions P and Q are specified in such that it allows coordinate lines to be attracted to specified lines and/or points in the domain or on the boundaries in making the numerical scheme to be efficience.

For computational purposes, the generating system of equations (13) and (14) is transformed to the computational plane by interachanging dependent and independent variables to yield

$$\alpha x_{\xi\xi} - 2\beta x_{\xi\eta} + \gamma x_{\eta\eta} = -J^2 (P x_\xi + Q x_\eta) \tag{15}$$

$$\alpha y_{\xi\xi} - 2\beta y_{\xi\eta} + \gamma y_{\eta\eta} = -J^2 (P y_\xi + Q y_\eta) \tag{16}$$

where

$$\alpha = x_\eta^2 + y_\eta^2 \,, \quad \beta = x_\xi x_\eta + y_\xi y_\eta$$

$$\gamma = x_\xi^2 + y_\xi^2 \,, \quad J = x_\xi y_\eta - x_\eta y_\xi \tag{17}$$

The transformation can then be determined by solving Eqs. (15) and (16). The application of the methodology to generate a grid system for the flow domain is illustrated. Fig. 3 displays the results of the solution to Eqs. (15) and (16) in the physical plane.

Since we desire to perform all computations in the transformed plane, where the mesh system consists of simple rectangulars, the governing equations and boundary conditions must be transformed in such that ξ and η are the independent variables. Using the fully conservative form of the differential operators given by

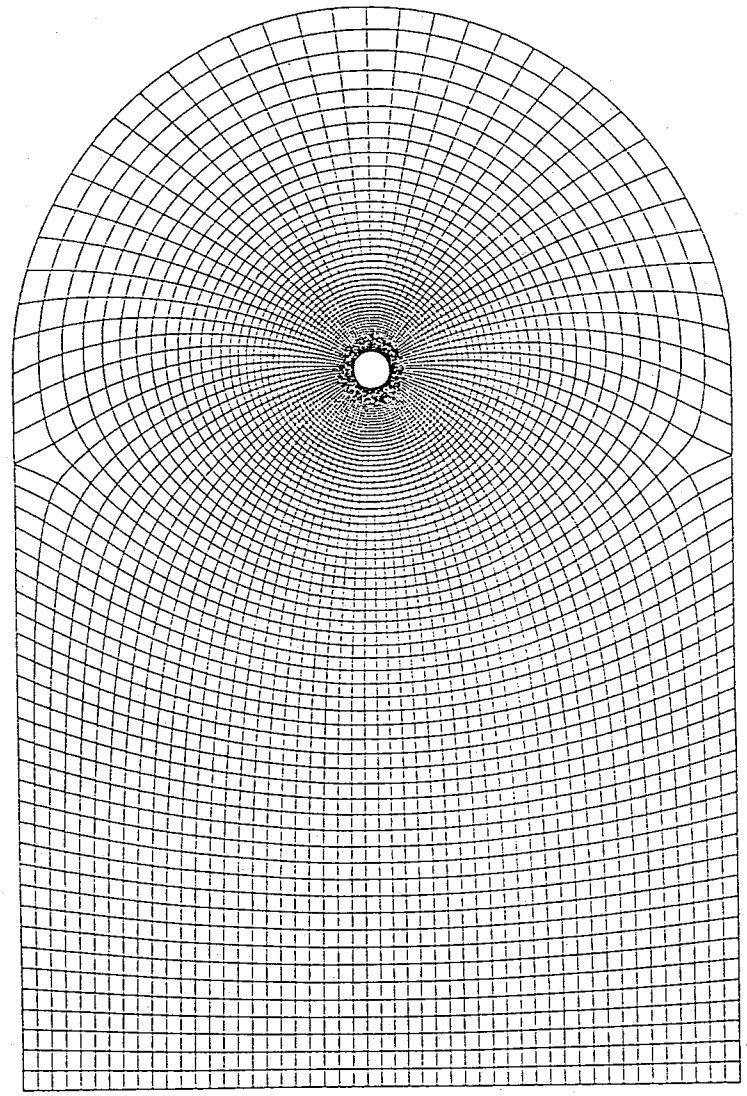

Fig. 3. Coordinates in physical plane.

$$f_x = \frac{1}{J}[(fy_\eta)_\xi - (fy_\xi)_\eta]$$
$$f_y = \frac{1}{J}[-(fx_\eta)_\xi + (fx_\xi)_\eta] \tag{18}$$

where f denotes some arbitrary function and J is the Jacobian defined in Eq. (17), the governing equations (8) through (11) become

$$\zeta_t + (\psi_\eta\zeta_\xi - \psi_\xi\zeta_\eta)J = \frac{1}{Re}\left[\frac{1}{J^2}(\alpha\zeta_{\xi\xi} - 2\beta\zeta_{\xi\eta} + \gamma\zeta_{\eta\eta}) + (Q\zeta_\eta + P\zeta_\xi)\right] \tag{19}$$

$$(\alpha\psi_{\xi\xi} - 2\beta\psi_{\xi\eta} + \gamma\psi_{\eta\eta})/J^2 + Q\psi_\eta + P\psi_\xi = -\zeta \tag{20}$$

$$\rho_t + (\psi_\eta\rho_\xi - \psi_\xi\rho_\eta)/J = \frac{1}{Re\,Sc}[(\alpha\rho_{\xi\xi} - 2\beta\rho_{\xi\eta} + \gamma\rho_{\eta\eta})/J^2 + (P\rho_\xi + Q\rho_\eta)] \tag{21}$$

$$u = (x_\xi\psi_\eta - x_\eta\psi_\xi)/J,\ v = (y_\xi\psi_\eta - y_\eta\psi_\xi)/J \tag{22}$$

The boundary conditions under the transformation can be specified in the computational plane as follows

(1) On the boundary
$\psi(\xi, 1, t) = 0, \zeta(\xi, 1, t) = -\gamma\psi_{\eta\eta}/J^2,\ \rho(\xi, 1, t) = 0$.

(2) On boundaries Γ_3^*, Γ_4^*, Γ_6^*, and Γ_7^*,
$\psi(\xi, \eta, t) = \psi_p, \zeta(\xi, \eta, t) = 0,\ \rho(\xi, \eta, t) = -\psi_p$. (23)

(3) On the boundary,
$\psi_\eta = 0,\ \zeta_\eta = 0,\ \rho_\eta = 0$.

Computational procedures

Numerical computations contain of both the transformation and flow problem solution. The first step in the computational procedure is to compute the grid transformation. Replacing by central difference formula, difference equations of (15) and (16) are solved by successive overrelaxation. Once convergence of the SOR point iteration is achieved, defining the x, y locations along lines of constant ξ and η, the spatial derivative x_η, y_η, x_ξ and y_ξ, and the transformation coefficients α, β, γ, and J at each grid point are computed. These derivatives, scaled to the appropriate size, are then available as input to constitute a complete description of the mesh geometry.

Given the description of the mesh system, the governing Eqs. (19), (20), (21) and (22) with boundary conditions were solved numerically with the fully implicit, forward-time, central-space formulation. The alternative direction implicit method of splitting the time step to obtain a multi-dimensional system equation was applied to solve Eqs. (19) and (21), while point SOR iteration was employed to converge the elliptic space variation of Eq. (20). The basic steps of calculating algorithm involved in advancing the configuration through the cycle from time t to time $t + \Delta t$ are as follows:

(1) At the beginning of the cycle, all required quantities are available either as initial data or as results from the previous cycle.
(2) Applying the ADI method, new values of ξ and ρ are obtained in advancing a time step by solving Eqs. (19) and (21) numerically subject to the appropriate boundary conditions.
(3) With the new value for the vorticity field, a new value for ψ is found from solving Eq. (20) by the SOR iteration. The magnitude of the relative convergent criteria is on the order of 0.01.
(4) From Eq. (22), u and w are found for the new components of velocity. Also obtain the vorticity on the obstacle surface.
(5) For selected cycles, a summary information is computed and this, together with various configurations, is recorded for studying the time development of the flow field.

Results and discussion

The establishments of flows for the uniform flows of weak stably stratified

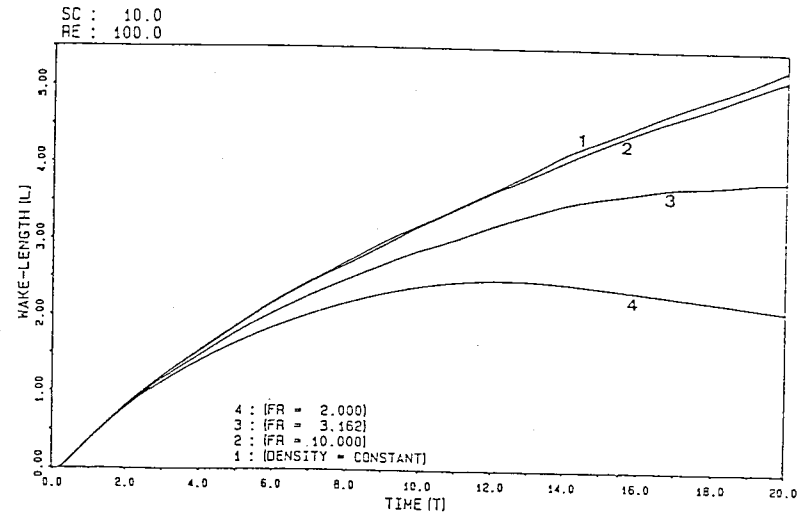

Fig. 4. Evolution of wake-length varied with F.

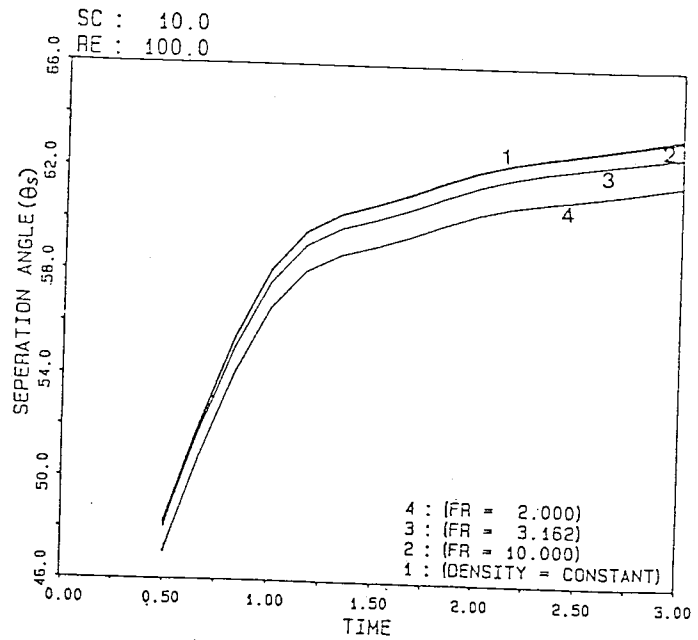

Fig. 5. Evolution of separation angle varied with F.

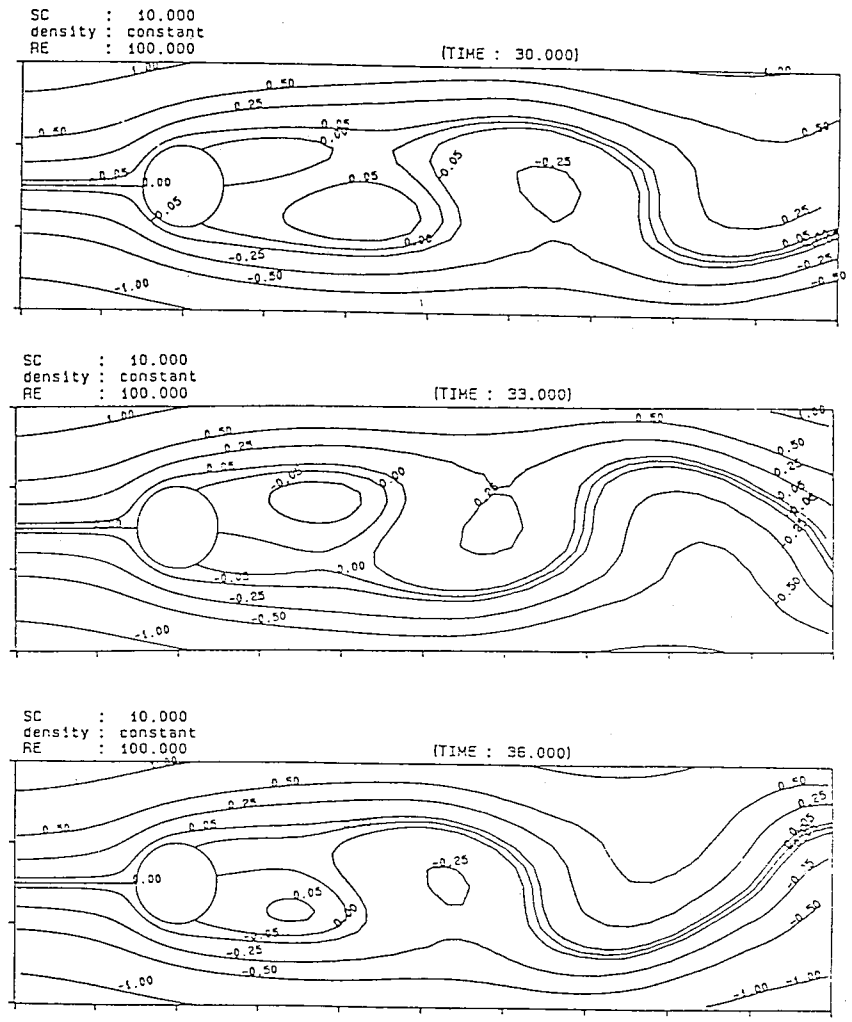

Fig. 6. Streamlines during vortex shedding for F = ∞.

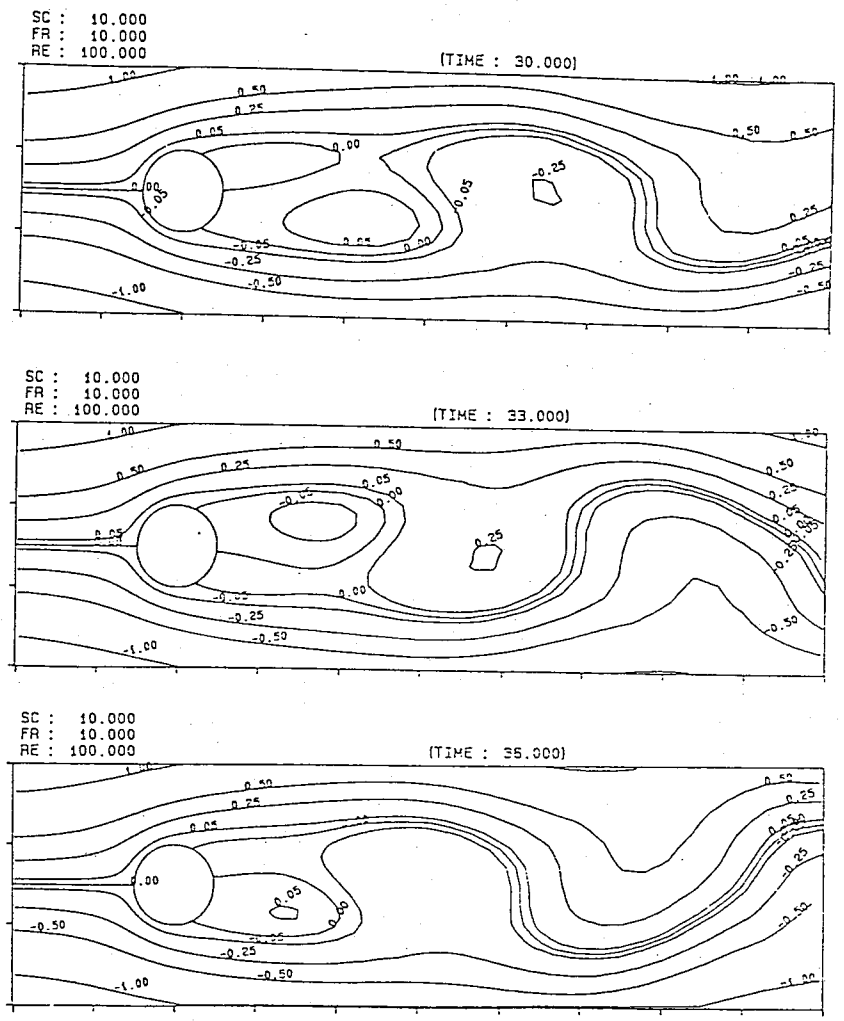

Fig. 7. Streamlines during vortex shedding for F = 10.

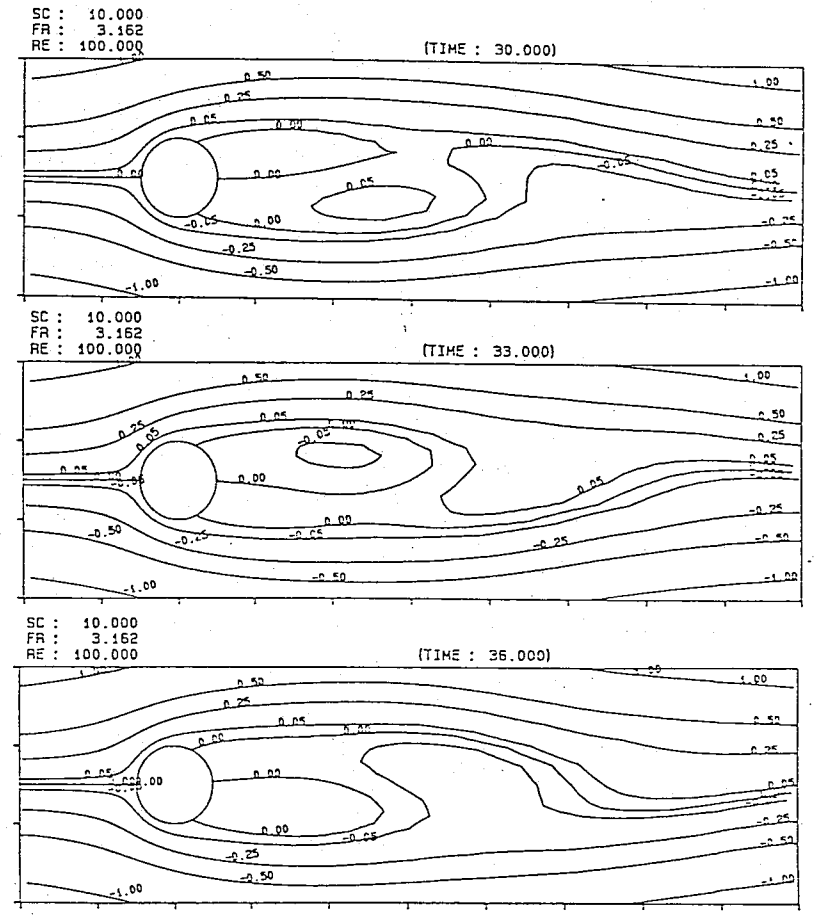

Fig. 8. Streamlines during vortex shedding for F = 3.16.

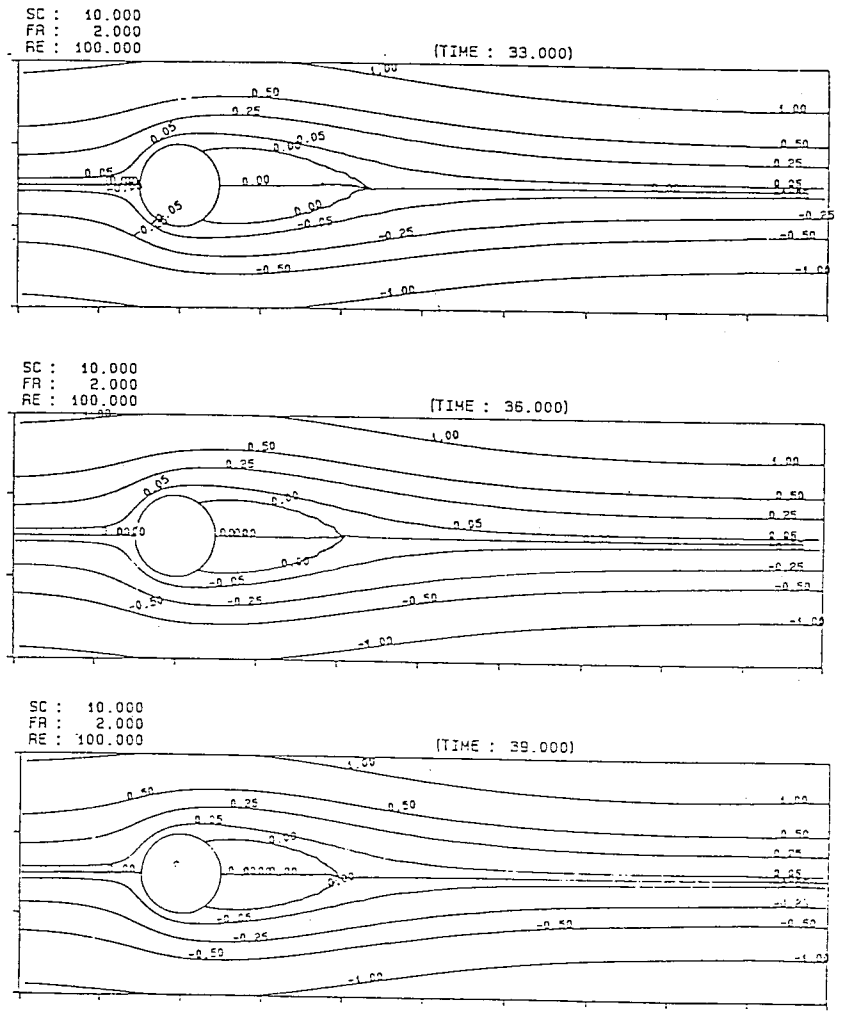

Fig. 9. Streamlines evolution for F = 2.0.

fluid past a circular cylinder were investigated numerically in variations of the ambient stratification for flow of Re = 100. In the operation of the numerical scheme, small times steps ($\Delta t = 0.002$) were utilized in the initial phases to resolve the fluid motion under the effects of impulsive start. Time steps were then subsequently increased to values of the order of 0.01 without significant increase in the number of iterations required to converge each step. The spatial grid resolution in the computational domain as shown in Fig. 2, was set as $\Delta\xi = \Delta\eta = 1$, and NZ = 90 NE = 80, $NZ_1 = 20$, $NZ_2 = 70$ and $NE_1 = 50$.

Effects of density stratification on the wake development behind the cylinder are investigated and obtained in the numerical computations. Some significant results are presented in the following. Figs. 4 and 5 showed the time evolution of the wake length and separation angle at the early times of flow development. It indicates that the density stratification will inhibit the flow development of the wake. With the time increase, the wake of the cylinder becomes unsteady and periodic. Figs. 6, 7 and 8 show the streamlines during vortex shedding at Re = 100 for $F = \infty$ (homogeneous fluid), 10 and 3.16 respectively. The shedding frequency of the vortex street varies with the increase of the density gradient. With the Strouhal number of S = shedding frequency xD/U, it means that flow of small F results in small S of the vortex shedding. Increasing the stratified gradient more, say F = 2, as showing in Fig. 9 the wake behind the cylinder maintains stationary and no alternate vortex shedding occurs.

The force acting on the cylinder in the flow is also influenced by the variation of the density stratification. In terms of nondimensional local surface pressure and tangential shear forces, the drag, the lift, and the torque coefficients are given by

$$C_D = -\int_0^{2\pi} p\cos\theta\, d\theta - \frac{1}{Re}\int_0^{2\pi} \zeta \sin\theta\, d\theta$$

$$C_L = -\int_0^{2\pi} p\sin\theta\, d\theta + \frac{1}{Re}\int^{\pi} \zeta \cos\theta\, d\theta\,. \qquad (24)$$

and

$$C_T = \frac{1}{Re}\int_0^{2\pi} \zeta\, d\theta.$$

Fig. 10 shows the drag, the lift and the torque coefficient histories for different F of flow Re = 100. It shows that the oscillatory character of the drag, the lift and the

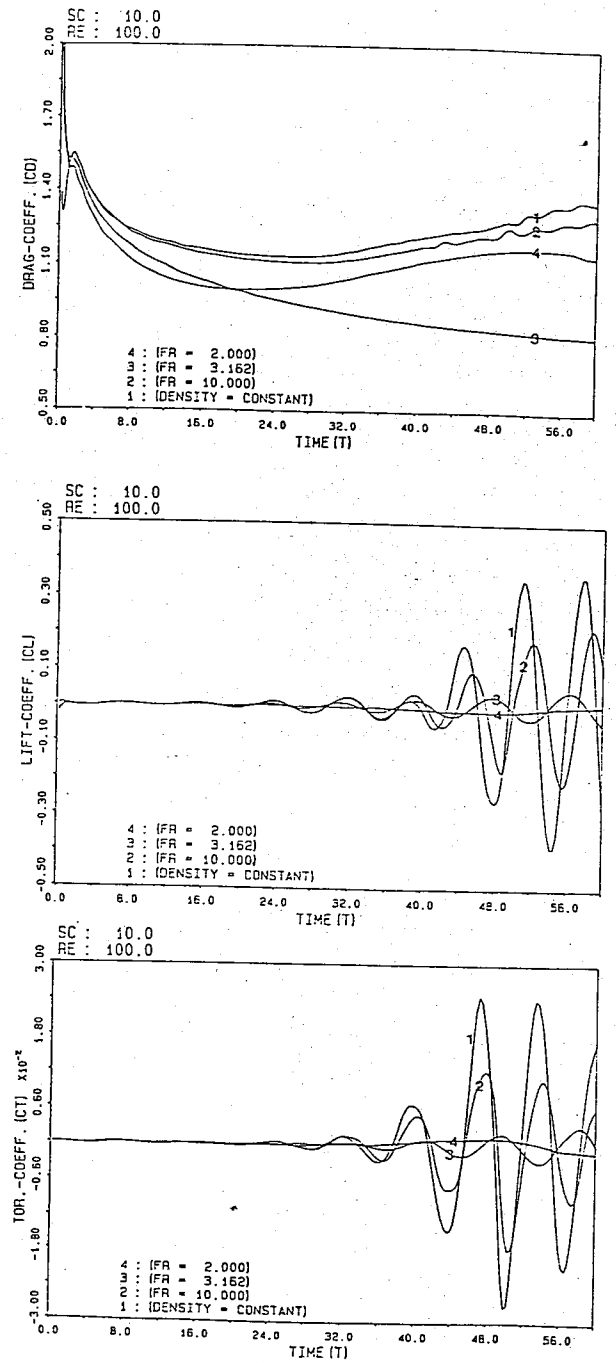

Fig. 10. Evolution of drag, lift and torque coefficients with different F for Re = 100.

torque experienced by the cylinder is reduced in the increases of the density stratification. For the case of F = 2, the vortex shedding is prohibited and the wake behind the cylinder becomes stationary. Some results for the effect of density stratification on the shedding frequency, the averaged drag and the amplitude of lift oscillatory are summaried in Table 1.

Table I. Effect of density stratification on mean drag, lift and Strouhal number

F	C_D	C_L	S
∞	1.29	0.76	0.164
10	1.24	0.44	0.154
3.16	1.0	0.10	0.118

Conclusions

With the use of boundary-fitted coordinates the study of laminar viscous flow with density stratification past a circular cylinder was performed. In series of numerical computations for several density stratifications, some tentative conclusions can be made:

(1) The density stratification tends to retard the vortex shedding from the two sides of the cylinder and to narrow down the wake development behind the cylinder.

(2) With the increase of the density stratification, the periodic configuration of the oscillatory character of the wake flow is decreased.

(3) The mean drag and the lift amplitude are decreased with the increase of the stratification.

(4) In the flow of heavier stratification, the wake behind the cylinder is stationary.

References

1. Deffenbaugh, F. D. and F. J. Marshall, "Time Development of the Flow About an Impulsively Started Cylinder," AIAA J., Vol. 14, No. 7, 908-913 (1976).
2. Gresho, P. M., R. L. Lee, and R. L. Sani, "On the Time-dependent Solution of

the Incompressible Navier-Stokes Equations," Recent Advances in Numerical Methods in Fluids, ed. by C. Taylor, Pineridge Press, Swansea, U. K., 27-80 (1980).
3. Haussling, H. J., "Viscous Flows of Stably Stratified Fluids over Barriers," J. the Atmosphere Sc., Vol. 34, 582-602 (1977).
4. Hwang, R. R., and S. W.. Jang, "Viscous Flows of Stably Stratified Fluids over Semi-Circular Obstacles," Proc. the National Science Council, Vol. 6, No. 1, 1-8 (1982).
5. Hwang, R. R., T. P. Chiang and M. T. Chiao, "Time-Dependent Incompressible Viscous Flow past a Circular Cylinder," J. the Chinese Institute of Engineers, Vol. 9, No. 6, 617-631 (1986).
6. Jordan, S. K., and J. E. Fromm, "Oscillatory Drag, Lift and Torque on a Circular Cylinder in a Uniform Flow," Phys. Fluids, Vol. 15, No. 3, 371-376 (1972).
7. Pao, Y. H., "Laminar Flow of a Stably Stratified Fluid past a Flat Plate," J. Fluid Mech., Vol. 34, part 4, 795-808 (1968).
8. Thompson, J. F., F. C. Thames, and C. W. Mastin, "Solutions of the Navier-Stokes Equations in Various Flow Regimes on Fields containing any Number of Arbitary Bodies Using Boundary-Fitted Coordinate systems," Lecture Notes in Phys, vol. 59, 421-450 (1976).
9. Thompson, J. F., F. C. Thames and C. W. Mastin, "TOMCAT," J. Comput. Physics, Vol. 24, 274-302 (1977).
10. Wei, S. N., T. W. Kao, and H. P. Pao, "Experimental Study of Upstream Influence in the Two-dimensional Flow of a Stratified Fluid Over an Obstacle," Geophysical Fluid Dynamics, Vol. 6, 315-336 (1975).

Nomenclature

C_D	drag coefficient
C_L	lift coefficient
C_T	torque coefficient
D	diameter of circular cylinder
D_m	the molecular diffusivity
F	the densimetric froude number
g	acceleration of gravity
p	pressure

R_e	Reynolds number
S	Strouhal number
S_c	Schmidt number
(x,z)	Cartesian coordinates
(u,w)	velocity components of (x,z) direction
t	time
ρ	density
β	stratification parameter
ψ	stream function
ζ	vorticity
ν	kinematic viscosity
(ξ, η)	transform coordinates

NUMERICAL SOLUTION OF FORCE CONNECTION FOR FLOW OVER AN IMPULSIVELY STARTED HEATED CYLINDER USING VELOCITY-PRESSURE COUPLING

Lai-Chen Chien
Institute of Physics, Academia Sinica, Nankang, Taipei 11529

and

Bi-Jung Lee
Department of Mechanical Engineering, Tamkang University
Tamshui, Taiwan 251

Abstract

The numerical simulation with primitive variables is incorporated to study the force-convection for an impulsively started heated circular cylinder. The in compressible momentum equation and energy equation with constant properties are considered to simulate the problem considered. In order to avoid the singularity at the very beginning of the start, the inner-outter expansion analytic solution is used as initial conditions of the flow and temperature field. The alternate direction implicit method is applied to solve the momentum and energy equations. The Poisson equation of pressure is worked out by successive over relaxation method. The computation results have a satisfactory aggrem ent with the existing solutions.

Introduction

The characteristics of flow over an impulsively started circular cylinder is of basic and important problem in fluid mechanics. Both the experiments or theoretical studies of this problem are interested by scientists. The force convection for flow over an impulsively started heated cylinder is applied widely in the engineering, such as hot wire, heat exchanger. This paper utilizes the primitive variables method to simulate the temperature, flow field of an impulsively started heated cylinder.

On the analytic solution, Blasius (1940) used the power series of time to simulate the situation of impulsively started cylinder. Bar-lev and Yang (1975), Chien (1977) investigated the flow field of this problem by using the inner-outter

expansion. Jofroudi and Yang (1983) transformed the Navier-Stokes equation to ordinary differential equation and obtained the steady solution by numerical method.

On the numerical solution, Son and Honnatty (1969) solved the unsteady problem by the unsteady Navier-Stokes equations formulation and found the second vortices at Reynolds number 500. Ja Phuoc Loc (1980) fomulated this problem by stream function-vorticity coupling and used Fourth-order compact numerical algorithm to high Reynolds number. Patel (1987) got the Von-Karmam vortex street at low Reynolds number by adding the Fourier Series on the steady solution. Kim and Chang (1988) coupled the laminar momentum equation and boundary energy equation to formulate this problem and got the solution by non-iteration numerical method. This finite difference method of non-iteration saved a lot of computation time. Kawamura (1984) got the vortex street at high Reynolds number by adding the roughness on the surface of cylinder and using the numerical primitive variables method. Chang and Finlayson (1987) used the finite element numerical method to reserch this situation, they had a good aggrement with the experimentical results.

In the next sections, the mathematical problem solved numerically are considered. Because of considering the initial-boundary condition problems, the more exact analytic initial condition and the boundary condition will be considered at this paper. And the subsequent section, the computational results are discussed and compared with the existing numerical solutions and experimentical dates.

Problem Formulation

1. The governing equations:

This problem to be solved is given by the two dimensional Navier-Stokes equations written in primitive variables. The flow is assumed as incompressible flow and the viscosity is constant. For the energy equation of this problem, the viscous dissipation, radiation and pressure gradient, mass concentration to the temperature are all reglected. For such laminar flow, the governing equations are:
continuity equation

$$\nabla \cdot \vec{V} = 0 \tag{1}$$

Navier-Stokes equation

$$\frac{\partial \vec{V}}{\partial t} + (\vec{V} \cdot \nabla)\vec{V} = -\frac{1}{\rho}\nabla P + \nu \nabla^2 \vec{V} \tag{2}$$

energy equation

$$\frac{\partial T}{\partial t} + \vec{V}(\nabla T) = \frac{K}{\rho C_p U_0 r_0} \nabla^2 T \tag{3}$$

Poisson equation of pressure

$$\nabla^2 P = -\nabla \cdot (\vec{V} \cdot \nabla)\vec{V} + \mu \nabla^2 D - \frac{\partial D}{\partial t} \tag{4}$$

where dilation

$$D = \nabla \cdot \vec{V} \tag{5}$$

2. Nondimensionalized and coordinate transformation

We consider to nondimensionalize the governning equations. In order to save the computation time, governning equations are mapping from the physical plane to the computational plane by using the function $Z = \ell nr$, Figure 1. The governning equations (1-4) are transfomed from polar coordinate system to computational plane (Z, θ) as following:
continuity equation:

$$e^{-z}\left(V_r + \frac{\partial V_r}{\partial z} + \frac{\partial V_\theta}{\partial \theta}\right) = 0 \tag{6}$$

Navier-Stokes equations:

$$\frac{\partial V_r}{\partial t} + e^{-z}\left(V_r \frac{\partial V_r}{\partial z} + V_\theta \frac{\partial V_r}{\partial \theta} - V_\theta^2\right)$$

$$= -e^{-z}\frac{\partial P}{\partial z} + \frac{1}{R_e}\cdot e^{-2z}\left(\frac{\partial^2 V_r}{\partial z^2} + \frac{\partial^2 V_r}{\partial \theta^2} - V_r - 2\frac{\partial V_\theta}{\partial \theta}\right) \tag{7}$$

$$\frac{\partial V_\theta}{\partial t} + e^{-z}\left(V_r \frac{\partial V_\theta}{\partial z} + V_\theta \frac{\partial V_\theta}{\partial \theta} + V_\theta V_r\right)$$

$$= -e^{-z}\frac{\partial P}{\partial \theta} + \frac{1}{R_e}\cdot e^{-2z}\left(\frac{\partial^2 V_\theta}{\partial z^2} + \frac{\partial^2 V_\theta}{\partial \theta^2} - V_\theta + 2\frac{\partial V_r}{\partial \theta}\right) \tag{8}$$

energy equation:

$$\frac{\partial T}{\partial t} + e^{-z}\left(V_r \frac{\partial T}{\partial z} + V_\theta \frac{\partial T}{\partial \theta}\right) = \frac{e^{-2z}}{R_e \cdot P_r}\left(\frac{\partial^2 T}{\partial z^2} + \frac{\partial^2 T}{\partial \theta^2}\right) \tag{9}$$

Poisson equation of Pressure

$$S_p = \frac{1}{R_e}\cdot e^{-3z}\left(\frac{\partial^2 D}{\partial z^2} + \frac{\partial^2 D}{\partial \theta^2} - \frac{\partial V_r}{\partial z} - 2\frac{\partial^2 V_\theta}{\partial z \partial \theta} - \frac{\partial^2 V_r}{\partial z^2}\right.$$

$$\left. - \frac{\partial^2 V_r}{\partial \theta^2} + V_r + \frac{\partial V_\theta}{\partial \theta} + 2\frac{\partial^2 V_r}{\partial \theta^2}\right) - e^{-2z}\left[2\frac{\partial V_r}{\partial \theta}\frac{\partial V_\theta}{\partial z}\right.$$

$$\left. + \left(\frac{\partial V_\theta}{\partial \theta}\right)^2 + \left(\frac{\partial V_r}{\partial z}\right)^2 + V_r\left(\frac{\partial^2 V_\theta}{\partial z \partial \theta} + \frac{\partial V_\theta}{\partial \theta} + \frac{\partial^2 V_r}{\partial z^2}\right)\right.$$

$$\left. + V_\theta\left(\frac{\partial^2 V_\theta}{\partial \theta^2} + \frac{\partial V_r}{\partial \theta} + \frac{\partial^2 V_r}{\partial z \partial \theta} - 2\frac{\partial V_\theta}{\partial z}\right)\right] \tag{10}$$

$$e^{-2z}\left(\frac{\partial^2 P}{\partial z^2} + \frac{\partial^2 P}{\partial \theta^2}\right) = S_p - \frac{\partial D}{\partial t} \tag{11}$$

3. Initial conditions

The problem is an unsteady problem. The more exact initial condition is necessary for the subsequent solutions. In this paper, we referred the analytic solution of Chien (1977) as flow initial condition and the analytic solution of Chien and Kung (1982) as temperature initial condition. The stream function analytic solution of Chien (1977):

$$\phi(r, \theta, t) = r - \frac{1}{r} - \frac{4}{\sqrt{\pi}}\cdot\frac{\sqrt{t}}{\sqrt{R_e}}\left(\frac{1}{r} + \sqrt{\pi}\,\eta\ \mathrm{erfc}\,\eta - e^{-\eta^2}\right)$$

$$- \frac{t}{R_e}\left(\frac{1}{r} - (6\eta^2 + 1)\ \mathrm{erfc}\,\eta + \frac{6}{\sqrt{\pi}}e^{-\eta^2}\right) - 2\left(\frac{t}{R_e}\right)^{3/2}$$

$$\cdot\left[\left(\frac{16}{3}\eta^3 + \eta\right)\mathrm{erfc}\,\eta - \frac{1}{\sqrt{\pi}}\left(\frac{16}{3}\eta^2 - \frac{1}{6}\right)e^{-\eta^2}\right.$$

$$\left. - \frac{1}{6\sqrt{\pi}}\right]\sin\theta + 8\frac{t\sqrt{t}}{\sqrt{R_e}}\left[\int_0^\eta f(\xi)\,d\xi - \frac{1}{\sqrt{\pi}}\left(1 + \frac{4}{9\pi}\right.\right.$$

$$\left.\left. - \frac{4\sqrt{2}}{3}\right)(r^{-2} + 2r - 3) + 2\frac{\sqrt{t}}{\sqrt{R_e}}\int_0^\eta g_3(\xi)d\xi\right]\sin\theta\cos\theta$$

$$+ 16\frac{t^2\sqrt{t}}{\sqrt{R_e}}\left[\int_0^\eta F_3(\xi)\,d\xi\sin\theta\cos^2\theta - \int_0^\eta f_3(\xi)\,d\xi\sin^3\theta\right] \tag{12}$$

where $\xi = \frac{(r-1)}{2\sqrt{\alpha_1 t}}$ is stretched variable and $\alpha_1 = (\epsilon\,Re)^{-1}$, strouhol number. Function

$f(\xi)$, $g_3(\xi)$, $F_3(\xi)$, $f_3(\xi)$ are error functions. And the temperature analytic solution of Chien and Kung (1982).

$$T = \operatorname{erfc}\lambda + (t/R_e)^{1/2} f_2(\xi) + t\, q_2(\xi)\cos\theta + (T/R_e) f_4(\xi) + (t^3/R_e)^{1/2} q_4(\xi)\cos\theta + t^2 h_4(\xi), \tag{13}$$

where $\lambda = \sqrt{\rho r}\,\xi$, $q_2(\xi)$, $f_4(\xi)$, $q_4(\xi)$ and $h_4(\xi)$ are error functions. Because of resistance of the assumption about the analytic solution, it only can be used at $t < 1$ and $Re >> 1$. We choose the solution at $t = 0.02$ as initial solution.

4. Boundary conditions

4.1 On the surface of circular cylinder:

Considering the inner boundary condition on the surface of circular cylinder is no slip condition and the cylinder is heated. The velocities on the cylindrical surface are zero and the temperature is set 1 after nondimensionalized:

$$V_r = V_\theta = 0\ , \quad T = 1$$

The pressure, on the surface of circular cylinder, can be gotten by solving the momentum equation with the no slip condition as:

$$-e^{-z}\frac{\partial P}{\partial Z} + \frac{1}{R_e} e^{-2Z}\left(\frac{\partial^2 U_r}{\partial r^2}\right) = 0 \tag{14}$$

Referring the Anderson (1983), the continuity equation is satisfied on the surface of cylinder then we can get the pressure on the surface from following finite difference form:

$$P_{1j} = P_{2,j} - \frac{1}{R_e}\left(\frac{V_{r2,j} - V_{r0,j}}{\Delta Z}\right) \tag{15}$$

$$V_{r0,j} = \frac{1}{2}(6\ V_{r2,j} - V_{r3,j}) \tag{16}$$

4.2 On the infinite far field:

Considering the outter boundary condition at the far flow field is non-influence field as the potential flow and low temperature set 0 after nondimensionalized:

$$V_\theta = -(1 + \frac{1}{r^2})\sin\theta \tag{17}$$

$$V_r = (1 - \frac{1}{r^2})\cos\theta \tag{18}$$

$$T = 0$$

And using the exploration, the pressure on the outter boundary can be gotten by the momentum equation directly. method:

Numerical Method

1. This paper solve the momentum equation and energy equation by A.D.I. (Alternative Direction Implicit) method:

(I) the first half time step at z-direction

$$\frac{V^n_{r_{ij}} - V^n_{r_{ij}}}{\Delta t/2} + e^{-z}\left(V^n_{r_{ij}}\frac{V^*_{r_{i+1,j}} - V^*_{r_{i-1,j}}}{2\cdot\Delta z} + V^n_{\theta_{ij}}\frac{V^n_{r_{i,j+1}} - V^n_{r_{i,j-1}}}{2\cdot\Delta\theta} - V^{n^2}_{\theta_{ij}}\right)$$

$$= e^{-z}\frac{P^n_{i+1,j} - P^n_{i-1,j}}{2\cdot\Delta z} + \frac{1}{R_e}\cdot e^{-2z}\left(\frac{V^*_{r_{i+1,j}} - 2V^*_{r_{ij}} + V^*_{r_{i-1,j}}}{\Delta z^2}\right.$$

$$\left. + \frac{V^n_{r_{i,j+1}} - 2V^n_{r_{ij}} + V^n_{r_{i,j-1}}}{\Delta\theta^2} - V^n_{r_{ij}} - 2\frac{V^n_{\theta_{i,j+1}} - V^n_{\theta_{i,j-1}}}{2\cdot\Delta\theta}\right) \tag{19}$$

$$\frac{V^*_{\theta\,ij} - V^n_{\theta\,ij}}{\Delta t/2} + e^{-z}\left(V^n_{r\,ij} \frac{V^*_{\theta\,i+1,j} - V^*_{\theta\,i-1,j}}{2\cdot\Delta z} + V^n_{\theta\,ij} \frac{V^n_{\theta\,i,j+1} - V^n_{\theta\,i,j-1}}{2\cdot\Delta\theta} \right.$$

$$\left. + V^n_{\theta\,ij}\cdot V^n_{r\,ij} \right)$$

$$= -e^{-z} \frac{P^n_{i,j+1} - P^n_{i,j-1}}{2\cdot\Delta\theta} + \frac{1}{R_e}\cdot e^{-2z}\left(\frac{V^*_{\theta\,i+1,j} - 2V^*_{\theta\,ij} + V^*_{\theta\,j-1,j}}{\Delta z^2} \right.$$

$$\left. + \frac{V^n_{\theta\,i,j+1} - 2V^n_{\theta\,ij} + V^n_{\theta\,i,j-1}}{\Delta\theta^2} - V^n_{\theta\,ij} + 2\,\frac{V^n_{r\,i,j+1} - V^n_{r\,i,j-1}}{2\cdot\Delta\theta} \right) \tag{20}$$

$$\frac{T^*_{ij} - T^n_{ij}}{\Delta t/2} + e^{-z}\left(V^n_{r\,ij}\frac{T^*_{i+1,j} - T^*_{i-1,j}}{2\Delta z} + V^n_{\theta\,ij}\frac{T^n_{i,j+1} - T^n_{i,j-1}}{2\cdot\Delta\theta}\right)$$

$$= \frac{e^{-2z}}{R_e\cdot P_r}\left(\frac{T^*_{i+1,j} - 2T^*_{ij} + T^*_{i-1,j}}{\Delta z^2} + \frac{T^n_{i,j+1} - T^n_{ij} + T^n_{i,j-1}}{\Delta\theta^2}\right) \tag{21}$$

(II) the second half time step at the θ direction

$$\frac{V^{n+1}_{ij} - V^*_{r_{ij}}}{\Delta t/2} + e^{-z}\left(V^*_{r\,ij}\frac{V^*_{r_{i+1,j}} - V^*_{r_{i-1,j}}}{2\cdot\Delta z} + V^*_{\theta\,ij}\frac{V^{n+1}_{r_{i,j+1}} - V^{n+1}_{r_{i,j-1}}}{2\cdot\Delta\theta} - V^{*2}_{\theta_{ij}}\right)$$

$$= -e^{-z}\frac{P^n_{i+1,j} - P^n_{i-1,j}}{2\quad\Delta z} + \frac{1}{R_e}\cdot e^{-2z}\left(\frac{V^*_{r_{i+1,j}} - 2V^*_{r_{ij}} + V^*_{r_{i-1,j}}}{\Delta z^2}\right.$$

$$\left. + \frac{V^{n+1}_{r_{i,j+1}} - 2V^{n+1}_{r_{ij}} + V^{n+1}_{r_{i,j-1}}}{\Delta\theta^2} - V^*_{r_{ij}} - 2\,\frac{V^*_{\theta\,i,j+1} - V^*_{\theta\,i,j-1}}{2\cdot\Delta\theta}\right) \tag{22}$$

$$\frac{V^{n+1}_{\theta\,ij} - V^*_{\theta\,ij}}{\Delta t/2} + e^{-z}\left(V^*_{r\,ij}\frac{V^*_{\theta\,i+1,j} - V^*_{\theta\,i-1,j}}{2\cdot\Delta z} + V^*_{\theta\,ij}\frac{V^{n+1}_{\theta\,i,j+1} - V^{n+1}_{\theta\,i,j-1}}{2\cdot\Delta\theta}\right.$$

$$\left. + V^*_{\theta\,ij}V^*_{r\,ij}\right)$$

$$= -e^{-z}\frac{P^n_{i,j+1} - P^n_{i,j-1}}{2\cdot\Delta\theta} + \frac{1}{R_e}\cdot e^{-2z}\left(\frac{V^*_{\theta\,i+1,j} - 2V^*_{\theta\,ij} + V^*_{\theta\,i-1,j}}{\Delta z^2}\right.$$

$$\left. + \frac{V^{n+1}_{\theta\,i,j+1} - 2V^{n+1}_{\theta\,ij} + V^{n+1}_{\theta\,i,j-1}}{\Delta\theta^2} - V^*_{\theta\,ij} + 2\,\frac{V^*_{r_{i,j+1}} - V^*_{r_{i,j-1}}}{2\cdot\Delta\theta}\right) \tag{23}$$

$$\frac{T^{n+1}_{ij} - T^*_{ij}}{\Delta t/2} + e^{-z}\left(V^*_{r\,ij}\frac{T^*_{i+1,j} - T^*_{i-1,j}}{2\cdot\Delta z} + V^*_{\theta\,ij}\frac{T^{n+1}_{i,j+1} - T^{n+1}_{i,j-1}}{2\cdot\Delta\theta}\right)$$

$$= \frac{e^{-2z}}{R_e\cdot P_r}\left(\frac{T^*_{i+1,j} - 2T^*_{ij} + T^*_{i-1,j}}{\Delta z^2} + \frac{T^{n+1}_{i,j+1} - 2T^{n+1}_{ij} + T^{n+1}_{i,j-1}}{\Delta\theta^2}\right). \tag{24}$$

2. Using the S.O.R. (Successive over Relaxation), we solve the poisson equation of pressure

$$P^{k+1}_{ij} = (1-\Omega)\,P^k_{ij} + \frac{\Omega}{2(1+\beta^2)}\left\{(P^k_{i+1,j} + P^k_{i-1,j})\right.$$

$$\left. + \beta^2\,(P^k_{i,j+1} + P^{k+1}_{i,j-1}) - \Delta z^2\cdot(\widetilde{SP}_{ij} + D^{*n}_{ij}/\Delta t)\right\} \tag{25}$$

where $\beta = \Delta z/\Delta\theta$

Referring to the study of Roach (1972, p 194) in order to, force the D^{n+1} to zero for the stability of convergence, we take the finite difference form of SP_{ij} is approaching:

$$\tilde{SP}_{ij} = \frac{1}{R_e} \cdot e^{-z_{ij}} \cdot \left(\frac{\tilde{D}_{i+1,j} - 2\cdot\tilde{D}_{ij} + \tilde{D}_{i-1,j}}{\Delta z^2} + \frac{\tilde{D}_{i,j+1} - 2\cdot\tilde{D}_{ij} + \tilde{D}_{i,j-1}}{\Delta\theta^2} \right.$$

$$- \frac{V_{r_{i+1,j}} - V_{r_{i-1,j}}}{2\cdot\Delta z} - 2\cdot\frac{V_{\theta_{i+1,j+1}} - V_{i+1,j-1} - V_{i-1,j+1} + V_{i-1,j-1}}{4\cdot\Delta z\cdot\Delta\theta}$$

$$- \frac{V_{r_{i+1,j}} - 2V_{r_{ij}} + V_{r_{i-1,j}}}{\Delta z^2} - \frac{V_{r_{i,j+1}} - 2V_{r_{ij}} + V_{r_{i,j-1}}}{\Delta\theta^2} + V_{r_{ij}}$$

$$+ \frac{V_{\theta_{i,j+1}} - V_{\theta_{i,j-1}}}{2\cdot\Delta\theta} + 2\cdot\frac{V_{r_{i,j+1}} - 2V_{r_{ij}} + V_{r_{i,j-1}}}{\Delta\theta^2}$$

$$- \left[2\cdot\frac{V_{r_{i,j+1}} - V_{r_{i,j-1}}}{2\cdot\Delta\theta} \cdot \frac{V_{\theta_{i+1,j}} - V_{\theta_{i-1,j}}}{2\cdot\Delta z} + \left(\frac{V_{\theta_{i,j+1}} - V_{\theta_{i,j-1}}}{2\cdot\Delta\theta} \right)^2 \right.$$

$$\left. + \left(\frac{V_{\theta_{i+1,j}} - V_{\theta_{i-1,j}}}{2\cdot\Delta z} \right)^2 + V_{r_{ij}} \cdot \left(\frac{V_{\theta_{i+1,j+1}} - V_{\theta_{i-1,j+1}} - V_{\theta_{i+1,j-1}} + V_{\theta_{i-1,j-1}}}{4\cdot\Delta z\cdot\Delta\theta} \right.\right.$$

$$\left.\left. + \frac{V_{\theta_{i,j+1}} - V_{\theta_{i,j-1}}}{2\cdot\Delta\theta} + \frac{V_{r_{i+1,j}} - 2V_{r_{ij}} + V_{r_{i-1,j}}}{\Delta z^2} \right) + V_{\theta_{ij}} \right.$$

$$\left. \cdot \left(\frac{V_{\theta_{i,j+1}} - 2V_{\theta_{ij}} + V_{\theta_{i,j-1}}}{\Delta\theta^2} + \frac{V_{r_{i,j+1}} - V_{r_{i,j-1}}}{2\cdot\Delta\theta} \right) \right.$$

$$\left. + \frac{V_{r_{i+1,j+1}} - V_{r_{i-1,j+1}} - V_{r_{i+1,j-1}} + V_{r_{i-1,j-1}}}{4\cdot\Delta z\cdot\Delta\theta} \right]$$

$$- 2\cdot\frac{V_{\theta_{i+1,j}} - V_{\theta_{i-1,j}}}{2\cdot\Delta z} \Big) \Big] \tag{26}$$

where

$$\tilde{D}_{ij} = \frac{V_{r_{i+1}} - V_{r_{i-1}}}{2\cdot\Delta z} + \frac{V_{\theta_{i,j+1}} - V_{\theta_{ij-1}}}{2\cdot\Delta q} \tag{27}$$

3. The drag of cylinder gomes from the friction force and the pressure on the surface. Calculate the drag coefficient by integrating this equation

$$C_D = C_{DS} + C_{DP}$$

$$= \int_0^{2\pi} \left[\frac{1}{R_e} (\omega)_{r_0} \cdot \sin\theta + (P^*)_{r_0} \cos\theta \right] d\theta \tag{28}$$

where C_{DS} is friction force coefficient and C_{DP}, pressure coefficient.

4. The heat transfer of the cylinder
Because of the no slip flow on the surface of cylinder, the heat transfer of the surface of cylinder only occurs by conduction. Define the Nusselt number $Nu = h\,D_0/K$ and the h coefficient of conduction $h = -K\frac{\partial T}{\partial r}\Big|_{r0}$, transfered to the computational plane. The Nusselt number

$$Nu = -2\frac{\partial T}{\partial Z}\Big|_{r_0} \cdot e^{-z_0} \tag{29}$$

5. The steps for numerical method.
(1) Get the initial conditions of pressure from the poisson equation of pressure with initial flow field.
(2) Solve the momentum equations and chergy equation by A.D.I.
(3) Use the S.O.R. to solve the Poisson equation of pressure with new flow field.

(4) Repeat (2), (3) until computation is finished.

Result and Discussion

In order to simulate the steep variation of the boundary layer, use the function $z = \ell n\ r$ coordinate transformation system to have the computational grids concentrate to the surface of cylinder as Loc and Boundard (1985). This paper use the analytic solution as the initial condition to avoid the singular point of the time zero. And it can simulate the initial configuration more exactly and also save the computational time to converge. From the initial flow field and momentum equation, we can get the initial condition of pressure. Fig 1 is the computational plane, the grids concertrate to the surface of cylinder.

1. Results of Reynolds number 100

In this problem, several important numerical results can be compared to the existing solution to ensure the accuracy of the program. First is the initial separation time. When the moderate time t = 0.54, we find that the velocity V_θ reverse at the rear of cylinder. The wake zone appears and moves to $\theta = \pi/2$. From table 1, the initial separation time have an aggrement with Collin and Dennies (1973) t = 0.513, Chien and Wang (1985) t = 0.50.

From Fig. 2 to Fig. 6, the wake zone grows larger according to the increment of the nondimensional time and the separation angle moves up to $\theta = 123°$ at t = 2.34. The variation of the separation angle to t is shown in Fig. 7.

Comparing with the experimental data of Honji and Teneda (1969), the length of the wake grows longer according to the increment of moderate time t as shown in Fig. 8. The variation of drag coefficient of cylinder is shown in Fig. 9. At the beginning, it results a big drag force because of the heavy change of the flow configuration. As the moderate time t increasing, the drag coefficient drops down quickly to $C_D = 1.32$ at t = 2.13. From Fig. 9, we find that C_D has a small increase at t = 2.13 then drops down smoothly to $C_D = 1.22$ at t = 15. Comparing with Payne's (1958) steady solation $C_D = 1.15$, it has an approaching situation.

To the conduction problem of cylinder, we fix the Prandtle number to 0.73 and the properties of flow to be constant. So the whole heat trasfer will be controlled by the Reynolds number. From Fig. 2 to Fig. 6, because of the impulse of the flow to the cylinder, the heat transfer on the front of cylinder is hardly transfered to the flow. But on the rear of the cylinder, the heat transfer grows graduately according to the increasement of moderate time. In the wake zone, the reversing

flow resists the heat to transfer, as the front flow of cylinder. So the heat is hardly transfered to the flow on the front of cylinder and wake zone. In this force convection problem, the heat transfer will be influenced by the flow configuration in deed. Fig. 10 shows the variation of the mean Nasselt number of the cylinder, as t increasing it approachs to Chang (1987) and Finlayson's steady solution.

2. Results of Reynolds number 500

From table 1, the initial separation time at t = 0.38 which has an aggrement with collin & Dennis (1973) 0.394 and Chien (1977) 0.375. Because of the impulse of the flow becoming stronger, the initial separation time comes earlier than Renolds number 100. Also the separation angle moves up to $\theta = 102°$ more quickly as Fg. 16 shows. From Fig. 11 to Fig. 15 the flow patterns, the wake grows larger according to the increasement of the moderate time t but the length of wake is shorter than the case of Reynolds number 100. Actually, the second bubbles appears at $\theta = 140°$ when t = 2.9 as the flow pattern shows. Also from Fig. 16, the v vorticity distributon on the cylindrial surface has a reversing situation in the wake zone near $\theta = 140°$. It confirms that the second bubbles oxist in the wake. The variation of drag coefficient shown in Fig. 17, we ccan find C_D drops down quickly and has a small increment at t = 1.46. This small increment of drag coefficient is simillar to Ta Phuoc Loc (1980).

As Reyndolds number getting larger, the impulse of the flow is getting stronger. The configuration of the temperature will be influenced by this stronger impulse of flow field. From Fig. 11 to Fig. 15, such as Reynolds number 100, the front of cylinder hardly has a good heat transfer and the rear of cylinder the heat transfers graduately according to moderate time. But the reversing flow will resist the heat transfer in the wake zone too. Because the impulse is more larger, the whole configuration of temperature convergs more small than the case of Reynolds number 100. The variation of the Nusselt number of the cylinder-rical surface according to the moderate time shown in Fig. 18. The Nusselt number is getting lower according to the increase of the angle from front of cylinder until meets the wake. Because the eversing of flow appears, the Nusselt number also reverse to get higher as increase of the angle. So the flow pattern influences the heat transfer in deed. Fig. 19 shows the variation of mean Nusselt number. As the moderate time increases, the mean Nusselt number approaches to steady.

Conclusion

This paper uses the numerical simulation with primitive variables to simulate the impulsively started heated cylinder. The A.D.I. method is used to solve the momentum and energy equation, also the S.O.R. method for the Poisson equation of Pressure. The results have a satisfactory aggrement with the existing solutions. The numerical primitive variables method can overcome the shortcoming of three-dimentional problem of the stream function-vorticity coupling system. It can be developed to the three dimensional problems.

References

1. BLASIUS, H.–– Small Perturbation Solution of Boundary Layer, NACA TM 1256, Washington, D.C., 1940.
2. YANG, H. T. and BAR LEV, M. –– Potential Flow Model for an Impulsively started Cylinder, J. Applied Mech., vol. 98, pp. 213-216, 1976.
3. CHIEN, L.C. –– Impuslively Started Viscous Flow over a Circular Cylinder, Ph. D. Dissertation, Dept. Aerospace. Eng. Univ. South. Calif., 1977.
4. JAFROUDI, H. and YANG, H. T. –– Computation of Steady Laminar Flow over a Circular Cylinder with Third-Order Boundary Conditions. J. Comput. Phys. vol. 49, pp. 181-197, 1983.
5. SON, J. S. and HANRATTY, T. J. –– Numerical Solution of Flow around a Cylinder at Reynolds Number of 40, 200 and 500, J. Fluid Mech., Vol. 35, Part 2, pp. 369-386, 1969.
6. TA PHUOC LOC –– Numerical Analysis of Unsteady Secondary Vortices Generated by an Impulsively Started Circular Cylinder. J. Fluid Mech., vol. 100, pp. 111-128, 1980.
7. PATEL, V.A. –– Symmetry of the Flow around a Circular Cylinder. J. of Computational Physics vol. pp. 65-99, (1987).
8. Chang, W. M. and Finlayson, B.A. –– Heat Transfer Inflow Past Cylinders at Re<150-Prt 1, Calculations for Constant Fluid Properties. Numerical Heat Transfer, vol. 12, pp. 179-195, 1987.
9. KIM. J. and CHANG, K. –– Unsteady Boundary Layer and Its Seperation over A Heat Circular Cylinder. International J. For Numerical in Fluids. vol. 8, pp. 165-179, 1988.
10. KAWAMURA, T. and KUWAHARA, K. –– Computational of High Reynolds

11. Roache, P. J. (1976). Computaticnal Fluid Dynamics, Hermosa Publishers, Albuquerque, New Mexico.

    Number for around Circular Cylinder with Surface Roughness, AIAA-84-0340, 1984.
12. HONJI, H. and TANEDA, S. –– Unsteady Flow past a Circular Cylinder. J. Phys. Soc. Japan, vol. 27, pp. 1668-1677, 1969.
13. PAYNE, R. B. –– Calculation for Unsteady Viscous Flow Past a Circular Cylinder, J. Fluid Mech., Vol. 4, pp. 81-86, 1958.
14. Collins, W. H. and Dennis, S.C.R. –– Flow past an Impulsively Started Circular Cylinder. J. Fluid Mech., Vol. 60, pp. 105-127, 1973.

C_D : drag coefficient
C_P : pressure coefficient
D : dilation ($D = \frac{\partial u}{\partial x} + \frac{\partial v}{\partial y}$)
D_o : diameter of the cylinder
h : convection heat transfer coefficient
K : thermal conductivity
N_u : $h D_o/K$, Nusselt number
N_{um} : Mean Nusselt number
P : State pressure
P_r : $\rho C_P \nu/K$, Prandtl number
R_e : $D_o U_o/\nu$, Reynolds number
r : the r-axis of cylindrical coordinates
r_o : radius of the cylinder
T : temperature
t : the time
V_i : the velocity at the radial direction
V_θ : the velocity at the fangentical direction
Z :
θ : the θ-axis of cylindrical coordinates
u : viscosity
v : dynamic viscosity
ρ : the density of fluid
ψ : stream function
ω : vorticity
β : $\Delta Z/\Delta\theta$

INITIAL SEPARATION TIME

	RE=100	RE=500
COLLIN & DINNES (A)	0.513	0.396
COLLIN & DINNES (B)	0.589	0.394
CHIEN	0.469	0.375
CHIEN & WANG	0.50	0.376
PRESENT	0.54	0.38

Table 1. Initial separation time.

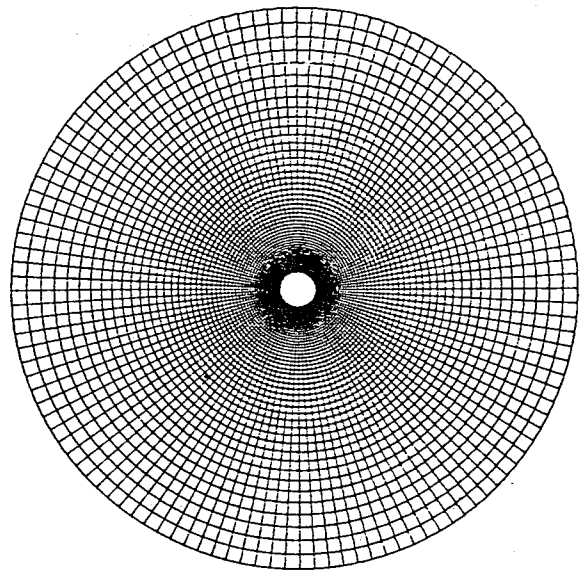

Figure 1. Grid system.

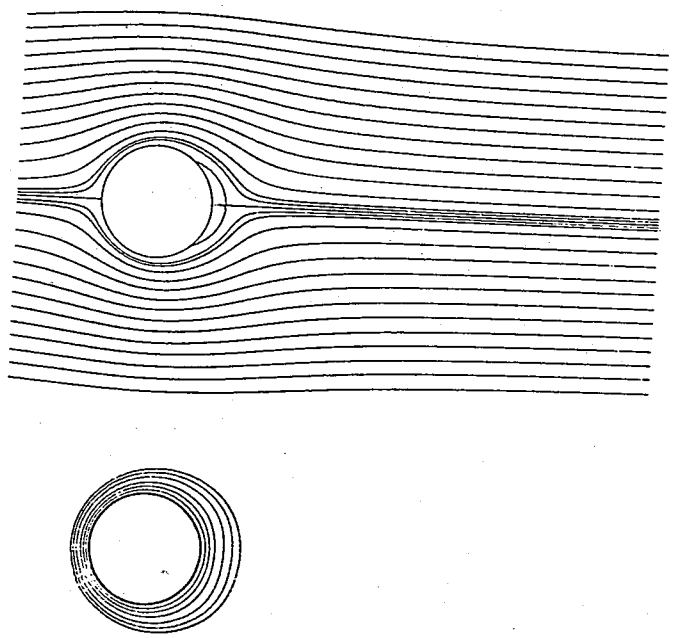

Figure 2. Flow pattern and iso-therm for Re = 100 at $t^* = 1.0$.

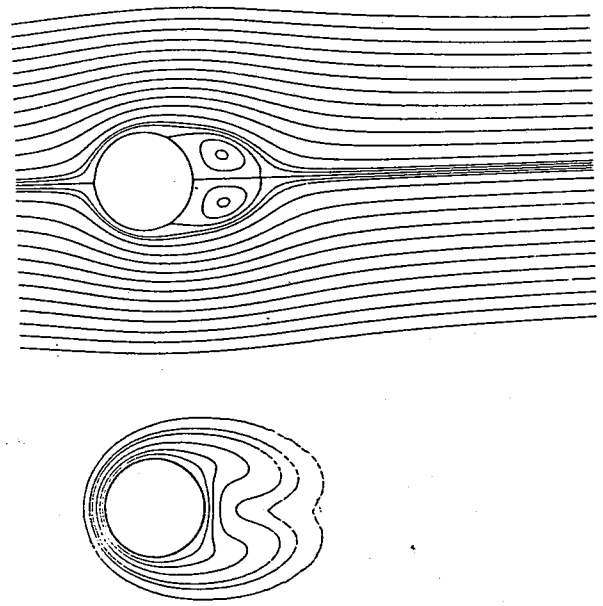

Figure 3. Flow pattern and iso-therm for Re = 100 at t = 3.0

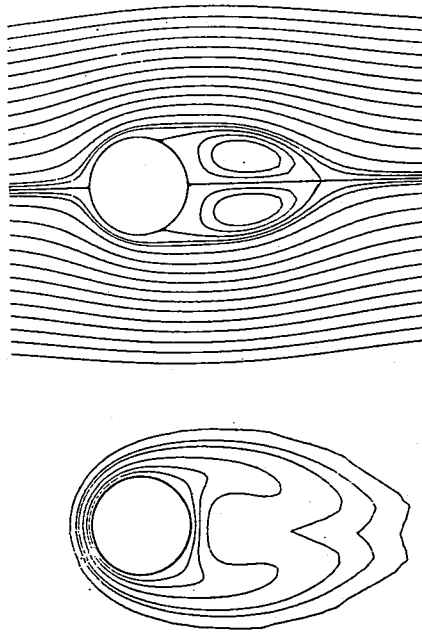

Figure 4. Flow pattern and iso-therm for Re = 100 at t = 6.0

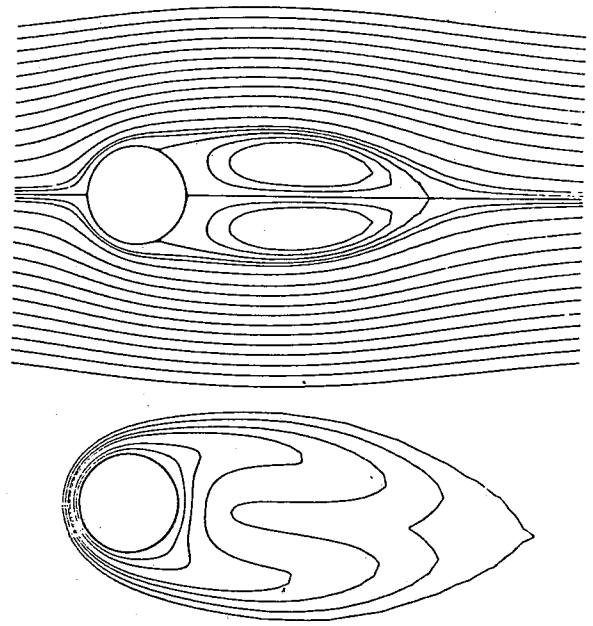

Figure 5. Flow pattern and iso-therm for Re = 100 at t = 15.0

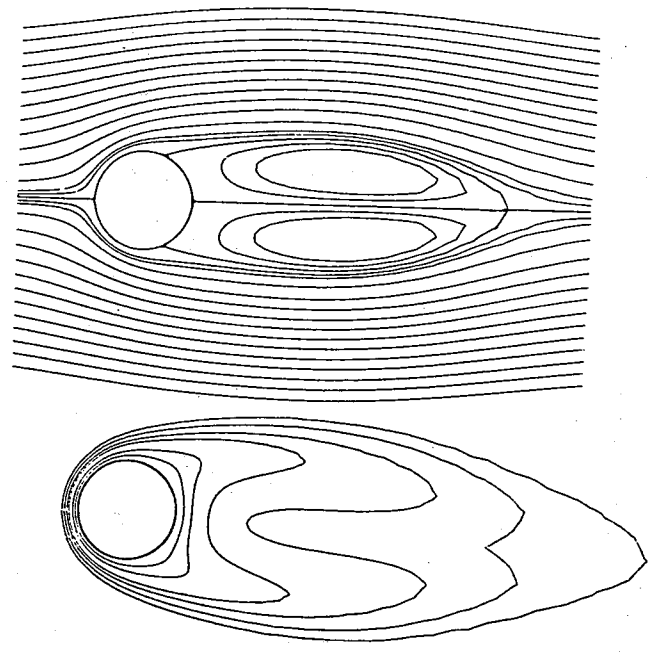

Figure 6. Flow pattern and iso-therm for Re = 100 at t = 20.0

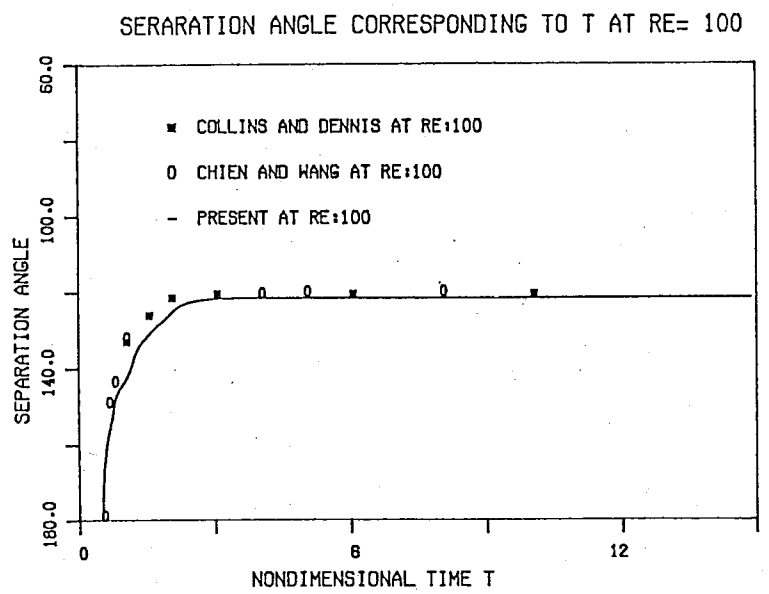

Figure 7. Separation angle corresponding to time for Re = 100

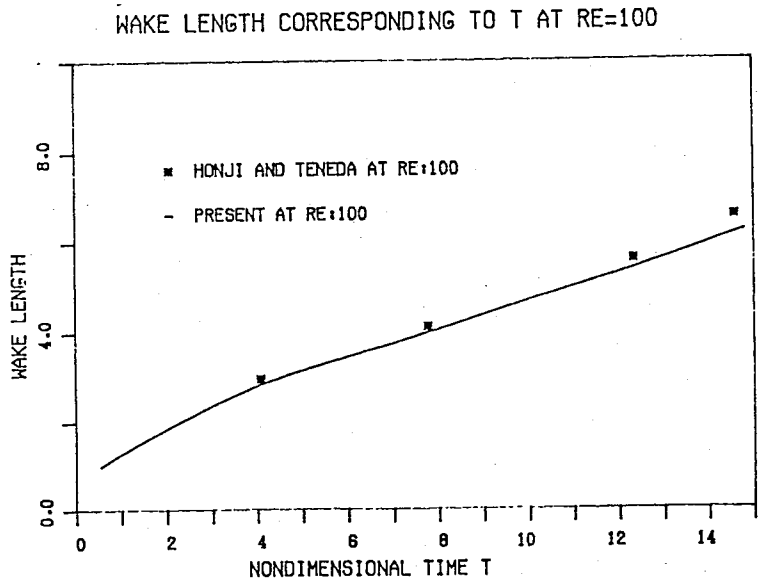

Figure 8. Wake length corresponding to time for Re = 100.

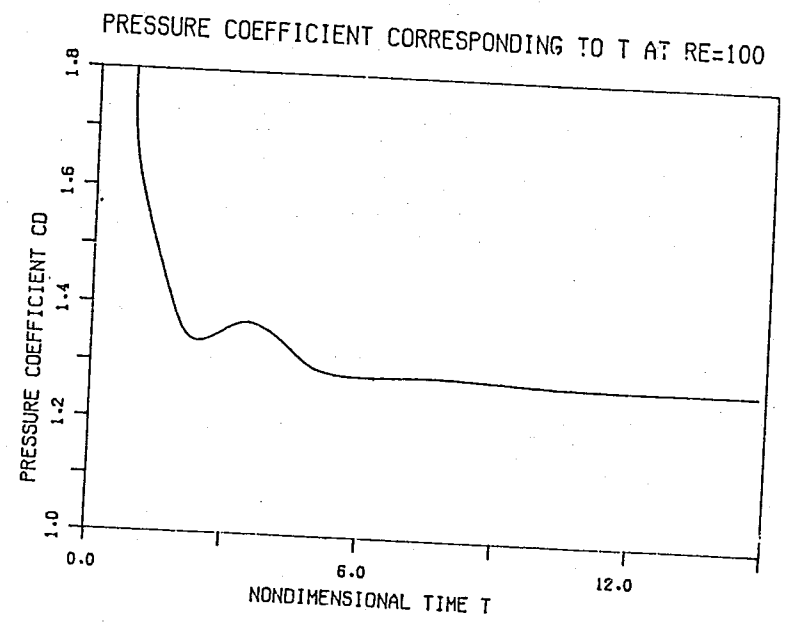

Figure 9. Pressure coefficient corresponding to time for Re = 100.

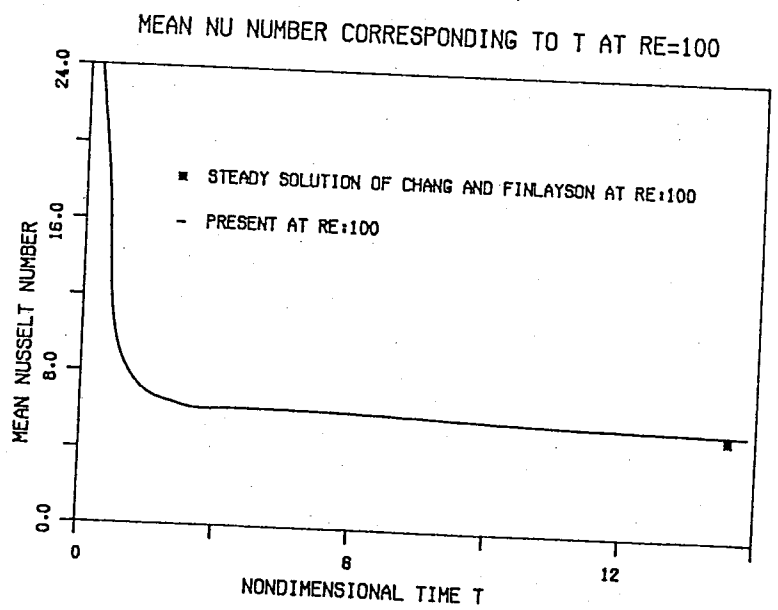

Figure 10. Mean Nusselt number along the cylinder surface corresponding to time for Re = 100.

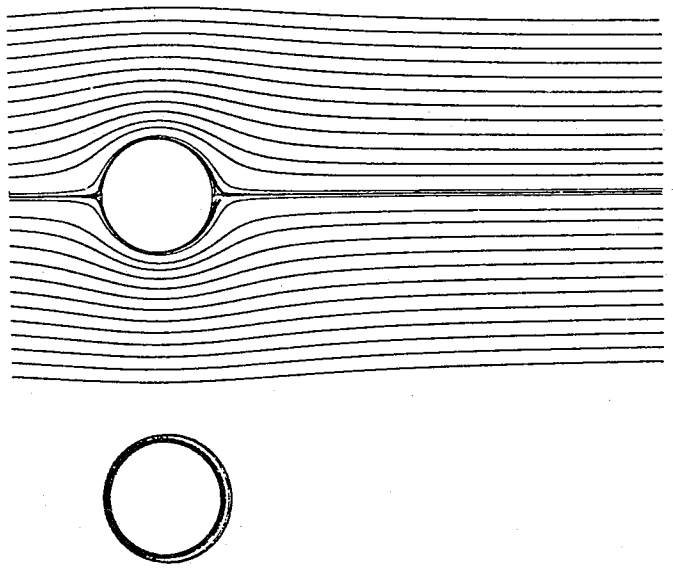

Figure 11. Flow pattern and iso-therm for Re = 500 at t = 1.0

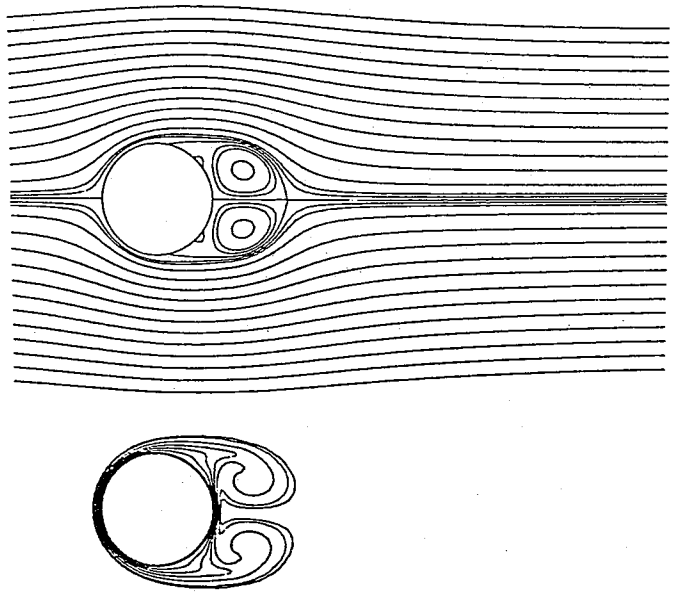

Figure 12. Flow pattern and iso-therm for Re = 500 at t = 3.0

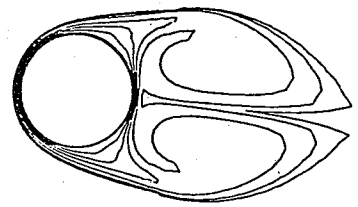

Figure 13. Flow pattern and iso-therm for Re = 500 at t = 10.0

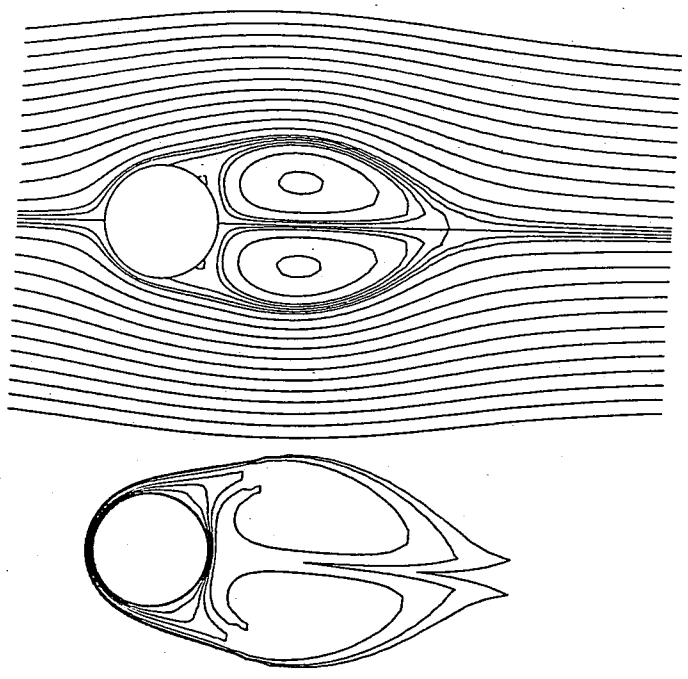

Figure 14. Flow pattern and iso-therm for Re = 500 at t = 15.0

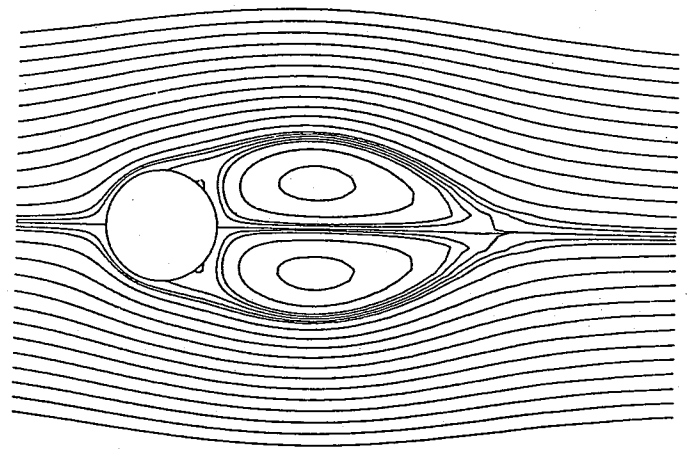

Figure 15. Flow pattern and iso-therm for Re = 500 at t = 20.0

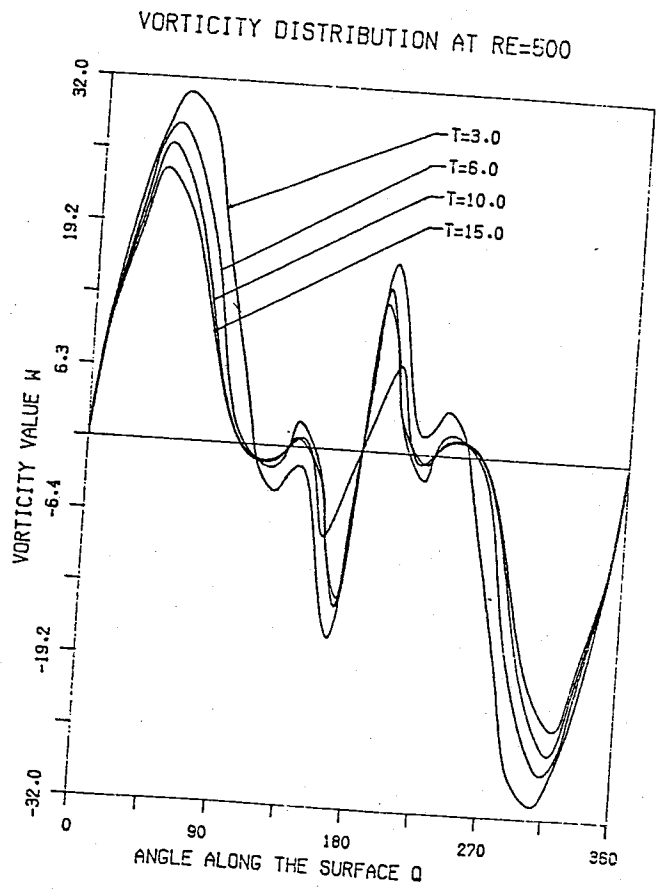

Figure 16. Vorticity distribution corresponding to time along the cylinder surface for Re = 500.

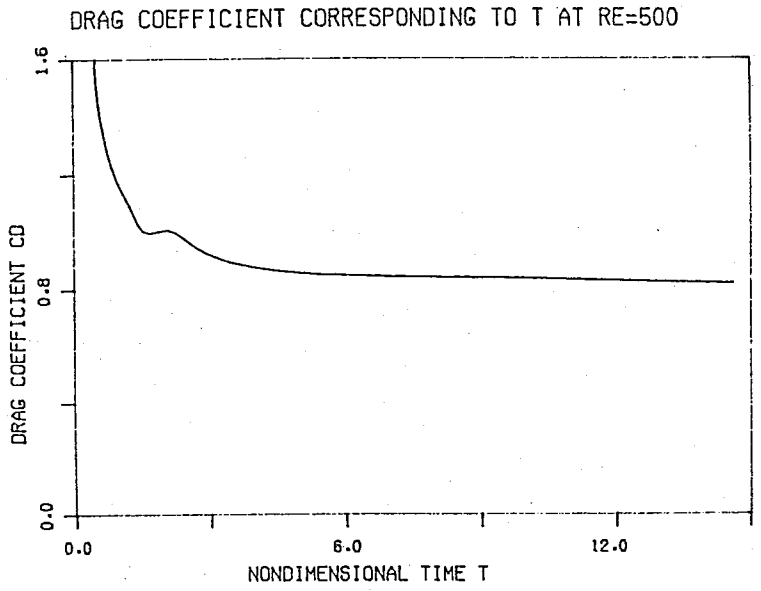

Figure 17. Drag coefficient corresponding to time for Re = 500.

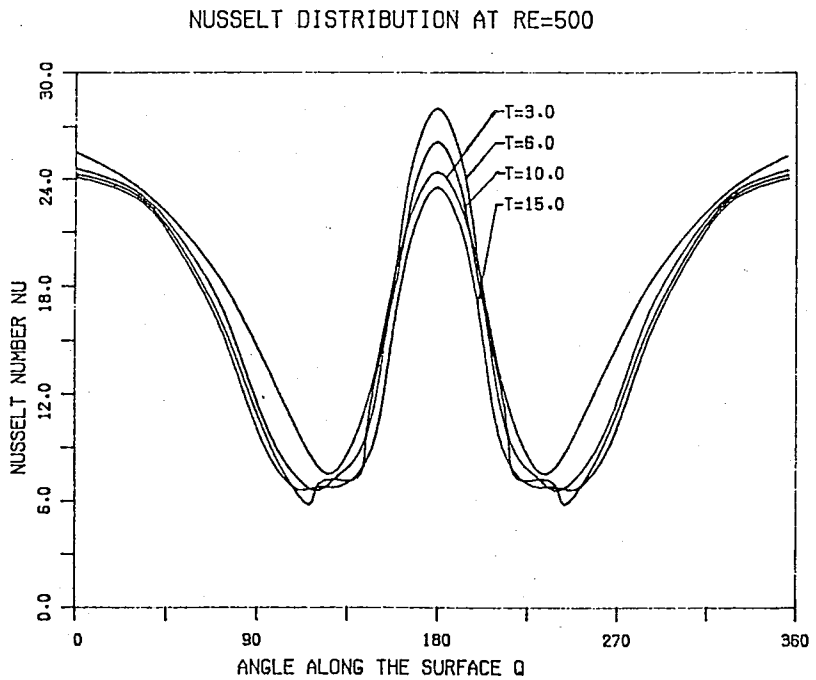

Figure 18. Nusselt number distribution corresponding to time along the cylinder surface for Re = 500.

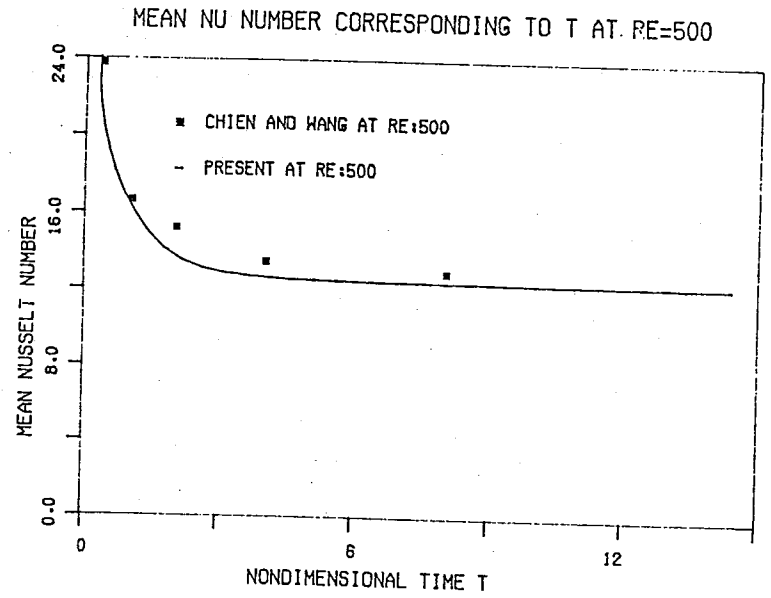

Figure 19. Mean Nusselt number corresponding to time along the cylinder surface for Re = 500.

CONSISTENCY CONSTRAINTS ON RENORMALIZED SUPERGRAVITY NO SCALE MODELS AT LOW ENERGY

Sai Ping Li and H. Havelet*

Service de Physicque Theorique† de Saclay,
91191 Gif-sur-Yvette Cedex, France

Abstract

We have used an analytic solution of the renormalization group equations to reexamine issues on no-scale supergravity models, namely, the hierarchy problem and the existence of a consistent stable absolute minimum of the scalar potential at a mass scale of the order of M_W. Special attention is given to the cases where there is mixing between the two Higgs doublets. Including first order corrections, we have obtained almost a unique solution in the SU(1,1)/U(1) and the SU(n,1)/U(n) no scale models. Neither of these models provide a natural solution of the hierarchy problem.

* Inst of Phys. Academia Sinica Nankang Taipei 11529
† Laboratorie de l'Institut de Recherche Fondamentale du Commissariat a l'Energie Atomique

Accepted for publication in: "Nucl. Phys. B"

OPTICAL POLARONS IN LAYERED SEMICONDUCTOR STRUCTURES

S. P. Li and S. C. Wang

Institute of Physics, Academia Sinica Nankang,
Taipei, Taiwan 11529

Abstract

Optical polarons in layered semiconductor structures are studied with the inclusion of many body effects. The energy shift, the effective mass and the life-time of an optical polaron are calculated as functions of electron density and interlayer separation. The resuts indicate behavior qualitatively different from that of pure two-dimensional optical polarons.

Accepted for priblication in Phys. Rev. B.

REMARK ON THE LOCALIZATION OF A POLARON IN THE ADIABATIC LIMIT

S. P. Li

Institute of Physics, Academia Sinica
Nankang, Taipei, Taiwan 11529 R.O.C.

Abstract

The dependence of the localization and the effective mass of a polaron on a parameter δ $(= D - 2\lambda - 2)$ in a deformable continum is reconsidered by employing an argument using the scaling hypothesis of Emin and Holstein.

Published in Phy. Lett. A135 (1989) 52.

SOLVING A PHENOMENOLOGICAL TWO-BODY DIRAC EQUATION

C. Y. Cheung and S. P. Li

Institute of Physics, Academia Sinica,
Taipei, Taiwan 11529, Republic of China

Abstract

We present a general scheme of solving a relativistic two-body equation with phenomenological potentials. We show that, for a class of local potentials, the problem can be reduced to that of solving a pair of coupled Schrodinger-type equations. A general discussion of the mixing of partial wave channels and the question of Klein paradox is also presented.

Submitted to Phy. Lett. B.

ANALYSIS OF $K \to 3\pi$ DECAYS IN CHIRAL PERTURBATION THEORY

Hai-Yang Cheng, C. Y. Cheung, and Wai Bong Yeung

Institute of Physics, Academia Sinica
Nankang, Taipei, Taiwan 11529
Republic of China

Abstract

Using the recently proposed higher-order chiral Lagrangians determined from the integration of nontopological chiral anomalies, we calculate corrections to the current-algebra analysis of $K \to 3\pi$ decay amplitudes expanded in powers of the Dalitz variables. Effects of quartic-derivative weak chiral Lagrangians are determined through the use of short-distance effective weak Hamiltonian and the factorization method. We find that (1) the constant and linear terms in the amplitude for $\Delta I = 1/2$ $K \to 3\pi$ are in excellent agreement with experiment; the previous discrepancy of (20-35)% between current algebra and data is thus accounted for by the higher-order effective Lagrangians, (2) the penguin interaction does not play an essential role in the $\Delta I = 1/2$ rule, for otherwise it will lead to a large disagreement for the constant and linear terms, (3) one of the two quadratic terms in the $\Delta I = 1/2$ process, which arise from the quartic chiral Lagrangians, is in accord with data within experimental errors, while the other is off by four standard deviations, (4) the linear term in the $\Delta I = 3/2$ transitions is in good agreement with experiment and contributions from quadratic terms are sizable.

To appear in Z. Phys. C (1989)

TOWARD THE UNDERSTANDING OF $K \to 3\pi$ DECAYS IN CHIRAL PERTURBATION THEORY

Hai-Yang Cheng, C. Y. Cheung, and Wai Bong Yeung
Institute of Physics, Academia Sinica, Taipei, Taiwan 11529, Republic of China

Abstract

Corrections to current-algebra analysis of $K \to 3\pi$ decay amplitudes are calculated using the dimension-four effective chiral Lagrangians, which are uniquely determined from the integration of nontopogical chiral anomalies. We find that the constant and linear terms in the $\Delta I = 1/2$ amplitude are in good agreement with experiment; the previous discrepancy of 20-35% between current algebra and experiment is thus accounted for by including the higher order chiral Lagrangians. Predictions for quadratic terms are also given for both $\Delta I = 1/2$ and $3/2$ transitions.

Published in Mod. Phys. Lett A4, 869 (1989).

ARE THERE REALLY NO EXPERIMENTAL LIMITS ON A LIGHT HIGGS BOSON FROM KAON DECAY?

Hai-Yang Cheng and Hoi-Lai Yu

Institute of Physics, Academia Sinica, Taipei, Taiwan 11529, Republic of China

Abstract

We re-examine the theoretical estimates of the decay $K \to \pi H$ and the experimental constraints on the existence of a light Higgs boson from this process. We find that: (i) a destructive interference between the spectator and non-spectator contributions is confirmed, (ii) pole diagrams though suppressed do contribute to $K \to \pi H$, (iii) the unknown parameter B in the chiral Lagrangian of Chivukula and Manohar is in fact zero, (iv) even if B were non-zero and even if the real part of the $K \to \pi H$ amplitude were canceled accidentally, the CP-violating contribution alone suffices to rule out a Higgs boson lighter than $2m_\pi$, and (v) Higgs bosons in the mass range $2m_\pi < m_H < 350$ MeV are excluded as long as the top quark is heavier than 60 GeV. Decay modes $K_L \to \pi^+\pi^- H$ and $K^+ \to \ell^+\nu H$ are briefly discussed.

Submitted to Phy. Lett. B

COMMENTS ON QCD SUM-RULE CALCULATIONS OF EXCLUSIVE TWO-BODY DECAYS OF CHARMED MESONS

Ling-Lie Chau

Department of Physics, University of California
Davis, California 95616

and

Hai-Yang Cheng

Institute of Physics, Academia Sinica
Nankang, Taipei, Taiwan

Abstract

Exclusive two-body decay amplitudes of charmed mesons evaluated by Blok and Shifman (BS) using QCD sum rules are analyzed using the model-independent quark-diagram scheme, which helps to pin point the generic structure of the BS calculations, and their difficulties when compared with the experimental data. We also point out what experimental improvements on the data and which new data are most helpful in sharpening these comparisons. Some comments on possible ways of further improving the theoretical calculations are given.

To appear in Mod. Phys. Lett. A (1989).

ADDENDUM: ANALYSIS OF TWO-BODY DECAYS OF CHARMED MESONS USING THE QUARK-DIAGRAM SCHEME (FURTHER DEVELOPMENTS: D → VV DECAYS AND HAIRPIN DIAGRAMS)

Ling-Lie Chau

Department of Physics, University of California
Davis, California 95616

and

Hai-Yang Cheng

Institute of Physics, Academia Sinica
Nankang, Taipei, Taiwan

Abstract

Anticipating the soon upcoming D → VV data, we further develop our previous work, "Analysis of Two-Body Decays of Charmed Mesons Using the Quark-Diagram Scheme", Phys. Rev. D36, 137 (1987). We incorporate in this addendum quark-diagram amplitudes of charmed meson decay into two vector mesons, and also the hairpin graphs.

To appear in Phys. Rev. D. (1989)

ON THE REALIZATION INDEPENDENCE OF CHIRAL SYMMETRY

Hai-Yang Cheng, C. Y. Cheung, and Wai Bong Yeung

Institute of Physics, Academia Sinica, Taipei, Taiwan 11529,
Republic of China

Abstract

In the U(3) × U(3) chiral perturbation theory, on-shell physical amplitudes are independent of any nonlinear realization of chiral symmetry. However, if one is restricted to the chiral symmetry SU(3) × SU(3), then the nonlinear realization scheme must be of the exponential form. The isospin violating decay $\eta \to 3\pi$ is employed as an example to elaborate on this phenomenon. We also consider a case in which the physical amplitude is independent of the realization scheme chosen, while the soft-pion theorem is.

To appear in Prog. of Th. Phys.

KAONS, HYPERPHOTONS, AND THE FIFTH FORCE

S. H. Aronson,[a] Hai-Yang Cheng,[a,b] Ephraim Fischbach,[c]
Daniel Sudarsky,[c] Carrick Talmadge,[c] and Josip Trampetic[a,d]

(a) Brookhaven National Laboratory, Upton, New York 11973
(b) Institute of Physics, Academia Sinica, Nankang, Taipei, Taiwan, ROC
(c) Physics Department, Purdue University, West Lafayette, Indiana 47907
(d) Physics Department, University of Oregon, Eugene, Oregon 97331

to appear in
in Proceedings of the 1988 Meeting of the Division
of Particles and Fields
August 1988, Storrs, Connecticut, USA
edited by K. Haller
(World Scientific, to be published)

ON THE NON–RESONANT THREE-BODY DECAYS OF CHARMED MESONS

Ling-Lie Chau

Physics Department, University of California, Davis, CA 95616

and

Hai-Yang Cheng

Institute of Physics, Academia Sinica, Taipei, Taiwan 11529

Abstract

Non-resonant 3-body decays of charmed mesons are first studied in the approach of effective SU(4) × SU(4) chiral Lagrangians. It is pointed out that the predictions of the branching ratios in chiral perturbation theory are in general too small when compared with experiment. However, the experimental results are comprehensible in the general framework of the quark-diagram scheme. The existence of a sizable W-annihilation amplitude, which is evidenced by the observation of $D_s^+ \to (\pi^+\pi^+\pi^-)_{NR}$, is the key towards an understanding of the 3-body non-resonant decays of D^+ and D_s^+. The measurement of $D^0 \to K^0K^+K^-$ and $D^0 \to K^0\pi^+\pi^-$ indicates that color suppression is not effective in the 3-body decay. Based on the quark-diagram analysis, predictions for some other non-resonant modes are given.

Submitted to Phys. Rev. D

DETECTING HYPERPHOTONS IN KAON DECAYS

Josip Trampetic[a,d], S. H. Aronson,[a] Hai-Yang Cheng,[a,b] Ephraim Fischbach,[c] and Carrick Talmadge,[c]

(a) Brookhaven National Laboratory, Upton, New York 11973
(b) Institute of Physics, Academia Sinica, Nankang, Taipei, Taiwan, ROC
(c) Physics Department, Purdue University, West Lafayette, Indiana 47907
(d) Physics Department, University of Oregon, Eugene, Oregon 97331

Abstract

Recent work aimed at searching for a possible "fifth force" has led to the question of whether the quantum of this putative force, the hyperphoton (γ_Y), can be detected experimentally. Following an argument by Weingerb, it was noted in Ref. 1 that γ_Y could show up in the decays $K^0 \to \pi\pi\gamma_Y$ at an experimentally interesting level, provided that γ_Y were a vector particle which coupled to the non-conserved hypercharge current (or more generally to any current which coupled differently to d and s quarks). This observation was followed by a number of papers which considered the decay modes $K^\pm \to \pi^\pm \gamma_Y$ and $K^0_{L,S} \to \pi^0\gamma_Y$.

Submitted to Phys. Rev. Lett.

$K \to \pi\pi\gamma$ AND CHIRAL PERTURBATION THEORY

Hai-Yang Cheng, S.-C. Lee, and Hoi-Lai Yu

Institute of Physics, Academia Sinica, Nankang,
Taipei, Taiwan, Republic of China

Abstract

Weak radiative decays $K_{L,S} \to \pi^+\pi^-\gamma$ and $K^+ \to \pi^+\pi^0\gamma$ are reexamined. The electromagnetic form factors and long-distance contributions to the direct photon emission are evaluated using the higher order effective chiral Lagrangian. We find that (1) the naive soft-pion theorem cannot be applied to the magnetic-type transition amplitude, (2) the short-distance contribution to $K_L \to \pi^+\pi^-\gamma$ is comparable to or even bigger than the long-distance one, (3) the $\Delta I = 1/2$ enhancement persists in the decay $K^+ \to \pi^+\pi^0\gamma$, (4) to the order of $1/\Lambda_\chi^2$ (Λ_χ being the chiral-symmetry breaking scale) the direct photon emission amplitude does not receive a contribution from penguin operators, and (5) the $1/N_c$ expansion improves the discrepancy between theory and experiment.

Z. Phys. C – Particles and Fields 41, 223-231 (1988)

STATUS OF THE $\Delta I = 1/2$ RULE IN KAON DECAY

Hai-Yang Cheng

Physics Department, Indiana University,
Bloomington, Indiana 47405, USA

and

Institute of Physics, Academia Sinica, Nankang,
*Taipei, Taiwan 11529, Republic of China**

Abstract

The $\Delta I = 1/2$ rule in $K \to \pi\pi$ decays and its status are discussed and reviewed. First, we present the phenomenological deductions which have a firm basis, including the penguin diagram, vacuum insertion, current algebra and chiral perturbation theory. Then we proceed to discuss new conjectures and speculations e.g. 1/N expansion, W-exchange, low-energy penguin diagrams, the s-d self-energy tadpole, QCD-duality, instanton effects, etc. and to assess their roles in understanding the $\Delta I = 1/2$ enigma.

* present address

International Journal of Modern Physics A. Vol. 4, No. 3 (1989) 495-582

WEAK AND STRONG CP VIOLATION

Hai-Yang Cheng

Institute of Physics, Academia Sinica
Nankang, Taipei, Taiwan 11529
Republic of China

Table of Contents

Lecture presented at the Spring School on "Medium- and High-Energy Nuclear Physics," Taipei, Taiwan, May 16-21, 1988. To be published by World Scientific (1988).

ISOSPIN BREAKING EFFECTS ON THE $\Delta I = 3/2$ $K \to \pi\pi$ AMPLITUDES

Hai-Yang Cheng

Institute of Physics, Academia Sinica, Nankang,
Taipei, Taiwan, Republic of China

Abstract

Without including isospin breaking effects, the experimental data of $K \to 2\pi$ yield $A_0/A_2 = (22.2 \pm 0.1)$ and $\delta_0 - \delta_2 = (56.5 \pm 3.0)^\circ$. The latter is substantially larger than the isospin phase shift difference determined from strong-interaction $\pi\pi$ scatterings; this seems to imply the importance of isospin violation. However, we show that effects of the π–η–η' mixing and the electromagnetic penguin contributions do not modify $\delta_0 - \delta_2$, but they account for about 17% of the observed $K^+ \to \pi^+\pi^0$ amplitude.

Published in Phys. Lett 201B (1988), 155.

IMPLICATIONS OF A NONVANISHING ϵ'/ϵ

Hai-Yang Cheng

Institute of Physics, Academia Sinica,
Taipei, Taiwan 11529, Republic of China

Abstract

Implications of the recent CERN NA31 result on the CP-violation parameter ϵ'/ϵ are discussed. The experimental positivity of ϵ'/ϵ implies that, within the context of the Kobayashi-Maskawa model, the parameter B_K is positive and that the real and imaginary parts of the penguin coefficient are of opposite signs. Due to the improved estimate of the $\eta - \eta'$ mixing and of the matrix element $<\eta_0|\mathcal{L}_-^{\Delta S=1}|K^0>$ the sign of ϵ'/ϵ in the Weinberg three-Higgs model of CP violation is predicted to be the same as that of the chiral suppression on CP-odd $K \to 2\pi$ amplitudes (owing to the presence of tadpole contributions), contrary to previous calculations. Genuine superweak gauge models in which ϵ' is essentially zero (e.g. the superweak color-sextet scalar model) are ruled out by the NA31 experiment: CP violation cannot be solely mediated by superweak interactions. A nonzero ϵ'/ϵ generally implies the presence of $W_L - W_R$ mixing effects in the left-right symmetric model with two generations of fermions.

Submitted to Phys. Lett. B.

ON THE WILSON COEFFICIENT OF THE PENGUIN OPERATOR

*Hai-Yang Cheng**

Physics Department, Indiana University,
Bloomington, Indiana 47405

Abstract

Recently an additional contribution to the real part of the Wilson coefficient function c_5 of the dominant penguin operator O_5 in $K \to 2\pi$ decay was found by Bardeen, Buras, and Gerard. We show that in the effective-Hamiltonian approach used by Gilman and Wise with the "heavy" charm-quark approximation, the additional contribution to c_5 originates from the penguin diagrams with u-quark loops which are left after the charm quark is integrated out. For $\mu \sim 1$ GeV (μ being the renormalization scale), the inclusion of the u-quark loop diagram amounts to adding a contribution $5/3\ \alpha_s(\mu)/12\pi$ to the standard estimate of c_5. Penguin diagrams at the low-momentum scale are briefly discussed.

Published in Phys. Rev. 37D (1988) 1908.

THE STRONG CP PROBLEM REVISITED

*Hai-Yang Cheng**

Physics Department, Indiana University, Bloomington
Indiana 47405, U.S.A.

Abstract

The strong CP-violating θ parameter, the problem of strong CP violation and their status are reviewed. Among all possibilities, two natural solutions to the strong CP puzzle are thoroughly discussed and emphasized: the axion-type mechanism for hard CP violation and the non-Peccei-Quinn scheme for spontaneous CP nonconservation. Basic properties of the axion are derived from the modified Peccei-Quinn symmetry. Astrophysical and cosmological constraints are described for two different types of invisible axions. In nonaxion solutions, CP is spontaneously broken at the grand-unification scale and the CP phase is transmitted down to the low energy sector by quantum effects or by fermion mixing effects. As a by-product, the cosmological baryon asymmetry, which is caused by the same source of CP violation ultimately responsible for the kaon ϵ parameter, is generated adequately at the one-loop level.

Phys. Rep. 158, No. 1 (1988) 1 – 89.

LOW-ENERGY INTERACTIONS OF SCALAR AND PSEUDOSCALAR HIGGS BOSONS WITH BARYONS

Hai-Yang Cheng

Institute of Physics, Academia Sinica,
Taipei, Taiwan, Republic of China

Abstract

It is pointed out the a fit to the baryon-octet mass spectrum to the first order of SU(3) breaking indicates unambiguously a substantial sea-quark content in the baryon at rest. Owing to the presence of sizeable strange quark-antiquark pairs in the nucleon as implied by the pion-nucleon sigma term, the effective low-energy scalar Higgs-nucleon coupling $g_{\Phi NN} \approx 2.2 \times 10^{-3}$ is dominated by strange quarks rather than by heavy quarks. The couplings $g_{\Phi\Sigma\Sigma}$ and $g_{\phi\Xi\Xi}$ are estimated to be 3.2×10^{-3} and 3.7×10^{-3}, respectively. Supplemented by the $1/N_c$ expansion (N_c being the number of colors) and by the recent EMC measurement on the proton polarized structure functions, the coupling of the pseudoscalar Higgs boson to nucleons is fixed. A discussion of axion and Majoron couplings is given.

To appear in Phys. Lett. B219, xxx (1989).

QUARK AND SPIN CONTENTS OF THE PROTON: IMPLICATIONS ON THE HIGGS-NUCLEON COUPLINGS*

Hai-Yang Cheng

*Institute of Physics, Academia Sinica, Taipei, Taiwan 11529,
Republic of China*

Abstract

The QCD quark content of the proton is probed via the mass spectrum of the baryon octet and the pion-nucleon sigma term. Even at low energies, a sizeable sea comprised of uu, dd and ss current-quark pairs is in the proton. This is further reinforced by the data on elastic νp and $\bar{\nu} p$ scatterings and on the proton polarized structure function: unless gluons carry enormously large net helicities about ten times as large as the proton spin, the sea is considerably polarized at all values of Q^2. As a consequence of the presence of a sea, the effective low-energy Higgs-nucleon coupling is dominated by strange quarks rather than by heavy quarks. Supplemented by the $1/N_c$ expansion, nucleon matrix elements of pseudoscalar quark bilinears are fixed. The content of QCD quarks in the pion is addressed.

Invited talk presented at Chinese-German Symposium on Medium-Energy Physics, Taipei, Taiwan, November 14-15, 1988 (to be published by World Scientific).

To be published by World Scientific (1988)

ISOSPIN VIOLATION IN NUCLEON-NUCLEON SCATTERING*

C. Y. Cheung

*Institute of Physics
Academia Sinica, Taipei, Taiwan 11529, Republic of China*

Abstract

A short review of recent progress in the theoretical analysis of isospin symmetry breaking in nucleon-nucleon scattering is given. Directions of future works are also discussed.

* Invited talked presented at the International Conference on Medium- end High- Energy Nuclear Physics; May 16-21, 1988, Taipei, Taiwan, Republic of China.

RELATIVISTIC CALCULATIONS OF THE (γ,p) REACTION*

C. Y. Cheung

Institute of Physics
Academia Sinica, Taipei, Taiwan 11529, Republic of China

Abstract

The (γ,p) reaction is proposed as a way of detecting the enhanced nuclear convection current which is suggested by relativistic models of the atomic nucleus. Differential cross sections have been calculated for the $^{16}O(\gamma,p)^{15}N$ reaction at intermediate energies. Both the direct knock-out and pion-exchange current mechanisms have been included using relativistic form of the nucleon current and four-component nucleon wave functions.

* Invited talked presented at the Chinese-German Symposium on Medium-Energy Nuclear Physics; November 14-16, 1988, Taipei, Taiwan, Republic of China

BOSON PAIR-BREAKING STATES IN NUCLEI

Hsi-Tseng Chen†‡ R. W. Richardson§, L. L. Kiang‖, Y. Tzeng¶, P. K. Teng¶, G. C. Kiang¶, C. W. Wang¶, S. F. Tsai†, E. K. Lin¶ and A. Arima+

† *Department of Physics, National Taiwan University, Taipei, Taiwan*
‡ *Physics Department, Chung-Yuan Christian University, Chung Li, Taiwan*
§ *Physics Department, New York University, New York, NY, USA*
‖ *Department of Physics, National Tsing-Hua University, Taipei, Taiwan*
¶ *Institute of Physics, Academia Sinica, Taipei, Taiwan*
+ *Department of Physics, University of Tokyo, Tokyo, Japan*

Abstract

The exact dispersion equations for the eigenstates of a system of bosons in a spherical or deformed potential well and interacting through a pairing interaction are used to reproduce the physics of the interacting boson model in three dynamical symmetry limits. These equations are generalised to treat the seniority-zero and -two states by switching on a surface-delta interaction between bosons. The model reproduces the quasi-band structure in transition nuclei.

Published in J. Phys. G: Nucl. Phys. 14 (1988) L205-L209.

THE REACTION (π^+, π^+d) ON ^{6}Li AND ^{12}C

J. R. Hurd, J. S. Boswell, R. C. Minehart, Y. Tzeng, H. J. Ziock
and
K. O. H. Ziock

Physics Department, University of Virginia,
Charlottesville, Virginia 22901, USA

L. C. Liu

Los Alamos National Laboratory, Los Alamos, NM 87545, USA

E. R. Siciliano

Department of Physics and Astronomy, University, of Georgia,
Athens, Georgia 30602, USA

Abstract

We have measured the angular and momentum distributions of the scatter-pions from the reactions ^{6}Li$(\pi^+, \pi^+d)^4$He and ^{12}C$(\pi^+, \pi^+d)^{10}$B in a coincidence experiment. We compare our results with two models based on the impulse approximation: a "one-step model" in which it is assumed that a pair of nucleons with a close spatial correlation is ejected simultaneously, and a "two-step model" in which it is assumed that the incident pion interacts with a single nucleon which then picks up a second nucleon of appropriate charge to form a deuteron. In the case of ^{6}Li both models give almost identical results and describe the shapes of the measured angular and momentum distributions well. In the case of ^{12}C the two-step model agrees more nearly with the experimental results.

Published in Nucl. Phys. A475 (1987) 743-760.

SUMMATION OF PARTICLE-PARTICLE RING DIAGRAMS USING GREEN FUNCTION DETERMINANTS

Yiharn Tzeng

Institute of Physics, Academia Sinica, Nankang,
Taiwan, Republic of China

T. T. S. Kuo

Physics Department, State University of New York at Stony Book,
Stony Brook, NY 11794, USA

Abstract

Using the Green function determinant's algebraic characteristics, we derive a simplified formula for summing up particle-particle and hole-hole ring diagrams to all orders exactly. The ground-state energy shift of a nuclear system can be obtained simply from the summation of all the differences between the eigen-state energies and the single-particle energies of hole-hole states. We illustrate the application of our formula by calculating the ground-state energy shift for ^{16}O using four versions of Skyrme effective nucleon-nucleon interactions. The contribution from all such higher order ring diagrams is found to be remarkably small compared with that from the corresponding first-order diagram.

Published in Nucl. Phys. A485 (1988) 85-92.

EXPERIMENTAL STUDIES ON THE EXCITED STATES OF ^{82}Kr POPULATED BY THE β-DECAY OF 35h ^{82}Br

L. L. Kiang

Department of Phy sics National Tsing-Hua University
Hsinchu 30043, Taiwan, Republic of China

and

G. C. Kiang, P. K. Teng, E. K. Lin, T. H. Yuan, C. W. Wang, J. L. Lo and B. Chen

Institute of Physics, Academia Sinica
Nankang Taipei 11529, Republic of China

Abstract

The excited states of ^{82}Kr populated by the β-decay of ^{82}Br ($T_{1/2}$ = 35h) have been investigated by using a HPGe-NaI (Tl) Compton suppression spectrometer and a HPGe-NaI (Tl) coincidenec circuit. A total of thirty γ-rays have been observed; their relative intensities and energies have been measured.

The $\gamma - \gamma$ directional correlation functions of 554-619 keV, 554-1318 keV, 698-776 keV, 1044-776 keV, 1318-776 keV, 827-1044 keV, cascades have been measured. The mixing ratios of multipolarities of various γ-transitions in ^{82}Kr nucleus have been deduced.

Based on both of the IBA model and its extended version with boson surface delta interaction (BSDI), the energy levels and the relative B(E2) values of the various γ-transitions in ^{82}Kr have been calculated and discussed.

發表在：核子科學，第二十六卷第一期　中華民國七十八年二月

AN EXPERIMENTAL INVESTIGATION OF $H^+ + e \rightarrow H^0$ WITH A 350 KEV PROTON BEAM ON A THIN CARBON TARGET*

C. M. Fou†, E. K. Lin, P. K. Teng, and C. W. Wang

Institute of Physics, Academia Sinica, Nankang, Taipei 11529 R.O.C.

Abstract

The reaction $H^+ + e \rightarrow H^0$ in ion-atom collision was investigated from θ = 45° to 75°. An enhancement of about 10% of the H^0 yield was observed between 60° and 65°. Preliminarye explanations for the experimental result and discussion attributing the enhancement to the classical double scattering mechanism are presented.

* Work supported in part by the National Science Council, R.O.C.
† Permanent address: Department of Physics and Astronomy, University of Delaware, Newark, Delaware 19716, U.S.A..

To be published in Journal of Physics B.

PHOTOEMISSION STUDIES OF Ag-ADDED Y-Ba-Cu-O SUPERCONDUCTORS

Y. C. Chou[a], *N. T. Liang*[a,b], *C. S. Kuo*[b]

and

T. T. Chen[a]

(a) Department of PHysics, National Tsing Hua University, Hsinchu, Taiwan
(b) Institute of Physics, Academia Sinica, Nankang, Taipei

Abstract

X-ray photoelectron spectroscopy (XPS) results of Ag-added $Y_1Ba_2Cu_3O_{7-\delta}$ superconductors are reported. The resistivity measurements show that addition of Ag decreases T_c and broadens the transition region. The O 1s core level XPS spectrum is doubly peaked; the peak at smaller binding energy (528.6 eV) is believed to be closely related to the superconductivity of $Y_1Ba_2Cu_3O_{7-\delta}$.

Published in Chin. J. of Phy. Vol. 26, No. 5 (1988)

中　央　研　究　院

物 理 研 究 所 集 刊

第　十　八　卷

發行人：林　　爾　　康
編輯者：中央研究院物理研究所集刊編輯委員會
出版者：中央研究院物理研究所　臺北市南港區
印刷者：昀　橋　印　刷　有　限　公　司
電　話：三　六　二　六　六　八　五

中華民國七十八年五月出版